THE UNIVERSITY OF MANITOBA

BEAM INTENSITY PROFILE MONITOR FOR A PARITY VIOLATION EXPERIMENT AT 230 MeV.

by

ALEXANDER M. SEKULOVICH

A THESIS

SUBMITTED TO THE

FACULTY OF GRADUATE STUDIES AND RESEARCH

IN PARTIAL FULFILLMENT OF THE REQUIREMENTS

FOR THE DEGREE OF MASTER OF SCIENCE

IN

NUCLEAR PHYSICS

DEPARTMENT OF PHYSICS

WINNIPEG, MANITOBA

FALL 1990

ISBN 0-315-71949-4

BEAM INTENSITY PROFILE MONITOR FOR A PARITY VIOLATION EXPERIMENT AT 230 MeV

BY

ALEXANDER M. SEKULOVICH

A thesis submitted to the Faculty of Graduate Studies of the University of Manitoba in partial fulfillment of the requirements of the degree of

MASTER OF SCIENCE

THE UNIVERSITY OF MANITOBA

RELEASE FORM

NAME OF AUTHOR: Alexander M. Sekulovich

TITLE OF THESIS: Beam Intensity Profile Monitor for a Parity Violation Experiment at 230 MeV.

DEGREE: MASTER OF SCIENCE

YEAR DEGREE GRANTED: 1990

(Signed)

Permanent Address:
TRIUMF
4004 Wesbrook Mall
Vancouver, B.C.
CANADA, V6T 2A3

DATED: ...11/26/90.....

Dedication

To my father.

Abstract

A dual function intensity profile monitor has been designed for a measurement of parity violation in $\vec{p}-p$ scattering at 230 MeV using longitudinally polarized protons. The device contains a set of split foil secondary electron emission (SEM) monitors to determine the median of the beam current distribution (in x and y). The split foils, coupled through servoamplifiers and operational amplifiers to upstream aircore steering magnets, have demonstrated the ability to hold the beam position stable to within $\pm$ 5 μm. This monitor also contains a set of foil-strip planes giving information on the intensity distribution projected onto the two orthogonal axes, x and y. Data were acquired using 0.008 mm thick, 0.90 mm wide aluminum foil strips at 1.00 mm centers. The foil strip planes were able to determine the beam centroid of a 20 mm full width $\frac{1}{e}$ beam spot to within $\pm$ 3 μm after one hour of data taking with a 100 nA beam.

Acknowledgements

I am particularly grateful to my supervisor Dr. W.T.H. van Oers for the guidance and support extended to me throughout my years as a graduate student. I also thank him for the unique opportunity to experience experimental research at a world class facility with an impressive group of collaborators. Special thanks to Dr. Shelley A. Page, Dr. William D. Ramsay, Dr. James Birchall, Dr. Norman E. Davison and Dr. Charles A. Davis for their guidance and taking time to answer any and all of my questions. I am also thankful to Dr. John R. Campbell, Dr. Alain R. Berdoz and Dr. Elie Korkmaz for their help with particular aspects of my project. There are a number of people affiliated with TRIUMF who helped me but they are far too numerous to mention.

I would also like to thank fellow graduate student Keith Furutani for his friendship and moral support as well as probes technician Martin R. Knoll for his contributions to my project and allowing me to contribute to his.

I am deeply indebted to my mother Juanita, brother Andrew and sister Michelle, but most of all, my father George for having faith in me, even when I didn't.

Contents

List of Figures

List of Tables

1 Introduction.

Results from the investigation of matter have led to the identification of four elementary forces in the universe: electromagnetic, strong and weak nuclear forces and gravity. The task of unifying these four forces into one common force has proven difficult. Glashow, Weinberg and Salam have been able to unite the electromagnetic with the weak nuclear force with great success[1]. Combining this electroweak force with quantum chromodynamics (QCD) has led to the development of what is known as the standard model. The final step would be to include gravity into such a theory, possibly with supersymmetry or grand unified theories, but as of yet no single theory has been accepted.

As the theorists have developed such theories, it is the purpose of the experimentalist to verify their hypotheses and provide experimental data from which to develop such theories. High energy physics experiments are able to test predictions of new and exotic particles by colliding beams of particles of sufficient energy to produce the particles directly. One such example is the Higgs boson which must exist in order for current theory to explain the mass of the electroweak intermediate vector bosons $W^{\pm}$ and Z^0. Intermediate energy physics experiments generally test the interactions of particles by directing intense beams on fixed targets, relying on improved statistics to observe very small effects to a high degree of accuracy. An example here would be the study of parity violation, a result of the weak interaction in the nucleon-nucleon scattering system which is dominated by the strong interaction.

To investigate the measurement of parity violation in elastic $\vec{p}-p$ scat-

[1]Glashow, Weinberg and Salam received the Nobel Prize for their work in 1979.

tering, the desired effect is only observable at the 10^{-7} level. An experiment must be conceived, engineered and developed with the utmost consideration given to understanding and reducing the systematic errors of the apparatus. Not only does this include a substantial number of diagnostic studies, but also a long and exhaustive investigation of beam properties to show that control over these properties can be obtained to the limit required by the experiment. It is this strict demand that has led to the design and development of a dedicated beam intensity profile monitor for a parity violation experiment at 230 MeV.

1.1 The Proposed Experiment.

In parity-conserving elastic $\vec{p} - p$ scattering, where the incident proton beam is polarized and the target is unpolarized, the scattering asymmetry is due only to the transverse polarization components of the beam perpendicular to the scattering plane. If one proceeds to orient the polarization in the longitudinal direction, parity conservation would imply a null result for the longitudinal analyzing power A_Z, defined as

$$A_Z = \frac{1}{\mid P_z \mid} \frac{\sigma^+ - \sigma^-}{\sigma^+ + \sigma^-}, \tag{1}$$

where σ^+ and σ^- are the helicity dependent cross sections with respect to the beam polarization. A nonzero result for A_Z implies parity nonconservation.

There are two methods used in experiments for the determination of A_Z. The first method is to use a scattering detector to determine the amount of beam scattered from the target. At low energies, where only the lowest partial wave transition amplitude contributes, the scattering is essentially isotropic. If the scattering detector covers a reasonable solid angle, an estimate of the total cross section for each helicity state allows a calculation of A_Z by extrapolation. The second method is to measure the beam current intensity before and after the scattering target. By correlation of the decrease in beam intensity with the helicity state of the beam, a cross section for each of the beam helicity states can also be obtained. When operating above several hundred MeV where A_Z can no longer be considered isotropic, it is more advantageous to determine the scattering asymmetry in this type of attenuation experiment.

To determine parity violation in the N-N scattering system, the effects of the Coulomb and strong forces must be eliminated to the 10^{-7} level since a strongly interacting probe is being used to extract a weak interaction effect. In more complex nuclei, there are nuclear structure effects which complicate the understanding of the strong interaction. It is therefore advantageous to consider an experiment involving proton-proton scattering. Once the strong interaction mechanism has been understood and eliminated, the resultant analyzing power can be expressed as a hadronic weak interaction effect. Fig. 1 shows the three dominant Feynman diagrams for the parity violating N-N interaction in the meson exchange model. The right vertex is the parity conserving (PC) strong interaction vertex involving a meson exchange from the nucleon. The left vertex is the parity non-conserving (PNC) weak interaction vertex and involves boson exchanges between the quarks.

In the meson exchange model normally used, three mesons can be exchanged in the interaction, a pion ($\pi^{\pm}$) or a vector meson (ρ and ω). Taking into account the associated isospin changes, there are a total of six weak meson-nucleon coupling constants which must be determined. The values of these weak coupling constants have been predicted by Desplanques,

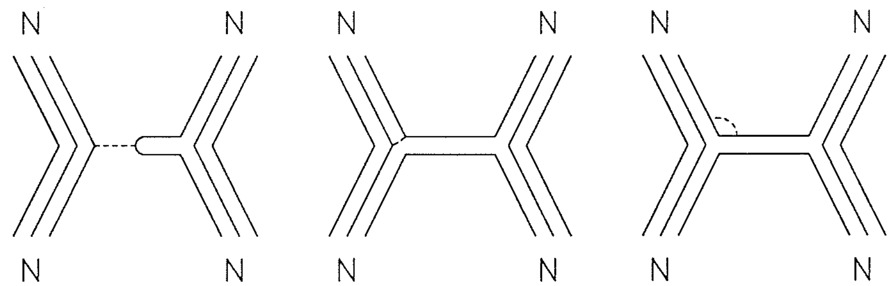

Figure 1: *The three dominant Feynman quark diagrams showing the weak PNC vertex (left) and the strong PC vertex (right) of the nucleon-nucleon interaction.*

Donoghue and Holstein (DDH) [1] based on the standard model and are shown in table 1. Calculations performed by Dubovik and Zenkin (DZ) [2] are also shown and agree reasonably well with those by DDH. By experimental determination of these weak coupling constants, a detailed comparison with the underlying theory can be made.

Simonius has proposed a $\vec{p}-p$ scattering experiment at 230 MeV [3]. At these energies, only the lowest order parity violating partial wave transition amplitudes contribute significantly. The dominant amplitude at low energy is the $({}^1S_0 - {}^3P_0)$ transition amplitude and at 230 MeV, its contribution integrated over all solid angle passes through zero as calculated by Simonius [4] and shown in fig. 2. This contribution can also be made to integrate to zero by choosing the angular acceptance of the detection apparatus and operating the experiment at a beam energy of 230 MeV which translates to 215 MeV at the target center. The fact that this partial wave transition amplitude contribution passes through zero is a result of the behaviour of the strong interaction phase shifts which are known independently [5]. The maximum contribution of the $({}^1S_0 - {}^3P_0)$ transition amplitude allowed by the variation in phase shift parameters at 230 MeV is ~ 5 % of the dominant $({}^3P_2 - {}^1D_2)$

Meson Exchanged	Coupling Constant	Theoretical Range (10^{-7}) (DDH)	Theoretical Best Value (DDH)	Theoretical Value (DZ)
$\pi^{\pm}$	f_π	0 $\leftrightarrow$ 11.4	4.6	1.3
ρ	h_ρ^0	-31 $\leftrightarrow$ 11.4	-11.4	-8.3
	h_ρ^1	-0.38 $\leftrightarrow$ 0	-0.19	0.39
	h_ρ^2	-11.0 $\leftrightarrow$ -7.6	-9.5	-6.7
ω	h_ω^0	-10.3 $\leftrightarrow$ 5.7	-1.9	-3.9
	h_ω^1	-1.9 $\leftrightarrow$ -0.8	-1.1	-2.2

Table 1: *Theoretical predictions for the weak meson-nucleon coupling constants as calculated by Desplanques, Donoghue and Holstein (DDH) and Dubovik and Zenkin (DZ). Superscripts denote the associated isospin change for each coupling constant.*

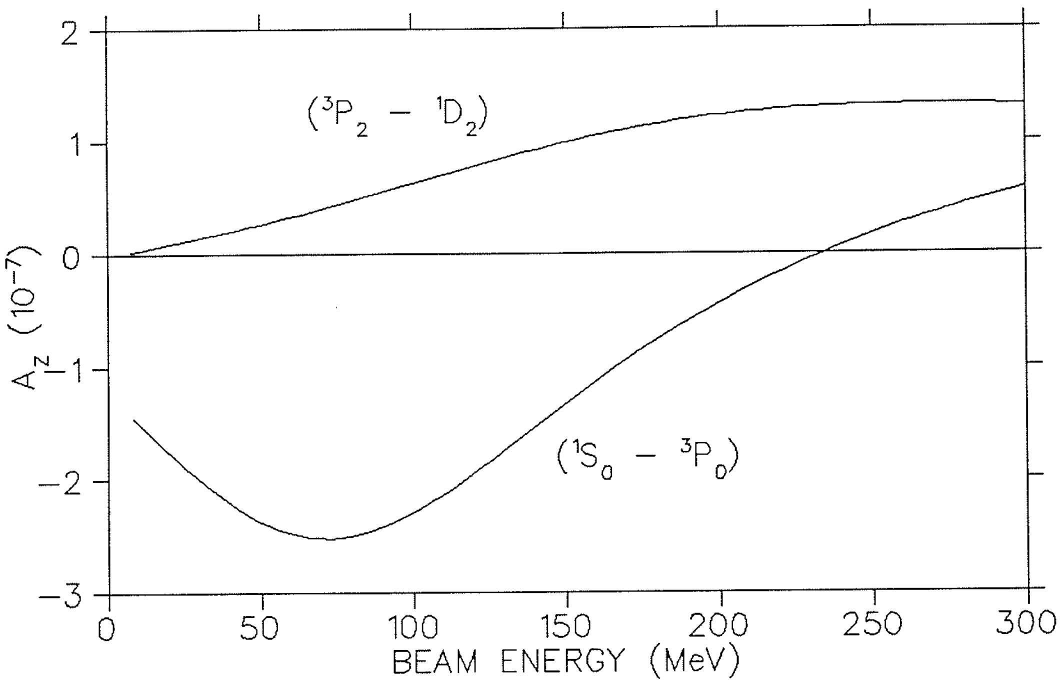

Figure 2: *Contributions to the longitudinal analyzing power from the two partial wave transitions* $({}^1S_0{-}{}^3P_0)$ *and* $({}^3P_2{-}{}^1D_2)$ *as calculated by Simonius.*

amplitude. Also shown in fig. 2 is the contribution from the next order parity violating transition amplitude $({}^3P_2 -{}^1 D_2)$. The $({}^1S_0 -{}^3 P_0)$ transition amplitude dominates at low energies and is determined by $h_\rho + h_\omega$, while the $({}^3P_2 -{}^1 D_2)$ transition amplitude is determined by h_ρ alone. The third parity violating transition amplitude to contribute, $({}^1D_2 -{}^3 F_2)$ has a theoretical contribution of only 5 % at 230 MeV. The longitudinal analyzing power A_Z can thus be related to the $({}^3P_2 -{}^1 D_2)$ transition amplitude which has been shown by Simonius to determine the h_ρ^{pp} coupling constant, where

$$h_\rho^{pp} = h_\rho^0 + h_\rho^1 + \frac{1}{\sqrt{6}} h_\rho^2. \tag{2}$$

The theoretical value at 230 MeV has been calculated as A_Z(230 MeV)= 0.4×10^{-7} [4] and A_Z(230 MeV)= 0.7×10^{-7} [6], assuming h_ρ^{pp} takes on the "best value" predicted by DDH.

1.2 Experimental Setup.

TRIUMF refers to TRI-University Meson Facility which is based on an isochronous 500 MeV H^- cyclotron. Due to come on line at TRIUMF in 1990 is an optically pumped polarized ion source, which is preferred for the parity violation experiment because the spin flip mechanism causes minimal changes to other beam properties. In this ion source, an unpolarized proton beam is accelerated to 5 keV and passes through a sodium vapour cell. The sodium atoms have the outer electron polarized by illumination from a circularly polarized laser tuned to the sodium D_1 transition at 589.6 nm. The outer electron is stripped from the sodium atom by the proton beam and after leaving the vapour cell, the electron spin is transferred to the proton using the diabatic field reversal technique[7]. The neutral, nuclear polarized hydrogen atom is then passed through a second sodium vapour cell and picks up a second electron, allowing the H^- ion to be accelerated through the cyclotron. By adjusting the laser frequency on the first sodium cell and changing the helicity of the laser light, a selection of the resultant spin of the exiting proton can be made. The spin of the extracted protons, which depends on the laser helicity and frequency, takes approximately 2 milliseconds to switch from one state to the other, limiting the spin flip rate to below 500 Hz.

Since H^- ions are accelerated in the cyclotron, a stripper foil can be inserted at a particular radial orbit, removing the electrons from the H^- ions and allowing the remaining protons to be extracted from the machine. Using this technique, several separate beams at different energies and at 100 % duty cycle can be extracted from the machine at once. The TRIUMF cyclotron, using the optically pumped polarized ion source, will provide a 500 nA beam of 230 MeV protons with a polarization of $\sim$ 70 % for the parity violation experiment.

There are two main experimental areas; the meson hall is used for the production of pion and muon beams, and the proton hall is dedicated to nucleon-nucleon and nucleon-nucleus studies. In the proton hall, beamline 4A is equipped with a 20.3 cm liquid deuterium target for polarized neutron production and beamline 4B features a magnetic spectrometer. The liquid deuterium target can be removed to allow the proton beam to continue down beamline 4A into a beam dump. It is beamline 4A which has been used to date for the setup and testing of the experimental apparatus.

As the polarized proton beam is accelerated through the cyclotron, the spin must be aligned in the vertical direction. Any component of the spin in the horizontal direction would be precessed due to the cyclotron magnetic field and would result in a depolarization of the beam. Only the vertical component of the spin would be retained. Once out of the cyclotron, the spin must be rotated into the longitudinal direction for the parity experiment. This can be done using two solenoid magnets and two dipole (bending) magnets[8]. Fig. 3 shows the four stages of spin precession from vertical to longitudinal. The solenoid magnets precess the spin by some angle ϕ in the plane perpendicular to the beam axis while the dipole magnets precess the spin by some angle θ in the plane perpendicular to the vertical axis. By arranging the magnets in the sequence solenoid (ϕ_1), dipole (θ_1), solenoid (ϕ_2) and dipole (θ_2), a longitudinally polarized beam can be produced at a range of beam energies. For this scheme to work at TRIUMF energies, the sum of bending angles for the two bending magnets must lie between 40^o and 100^o.

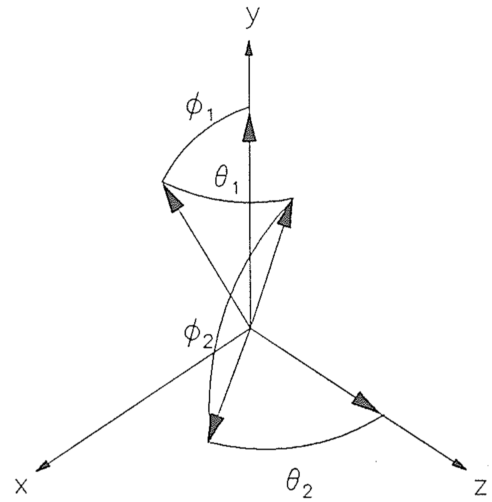

Figure 3: *The four stages of spin precession from vertical (y axis) to longitudinal (z axis) using solenoid (ϕ) and dipole (θ) magnets.*

Fig. 4 shows the proposed beamline setup for the parity experiment on beamline 4A. The first elements of dedicated parity apparatus encountered by the beam are the aircore steering magnets. These steering magnets are used in conjunction with the intensity profile monitors which are also equipped with position sensing split plates operating on secondary electron emission. The displacement signal of the beam from some predefined position is fed to electronic servo amplifiers, then to the aircore steering magnets which correct the beam position. Aircore steering magnets were used for the test runs described in this thesis. However, ferrite core steering magnets are being considered for the final parity setup. Ferrite core steering magnets can provide steering equal to that of the aircore steering magnets, but are more compact and provide a more uniform magnetic field.

One of the functions of the beam intensity profile monitors is to provide the intensity distribution of the beam in the horizontal and vertical

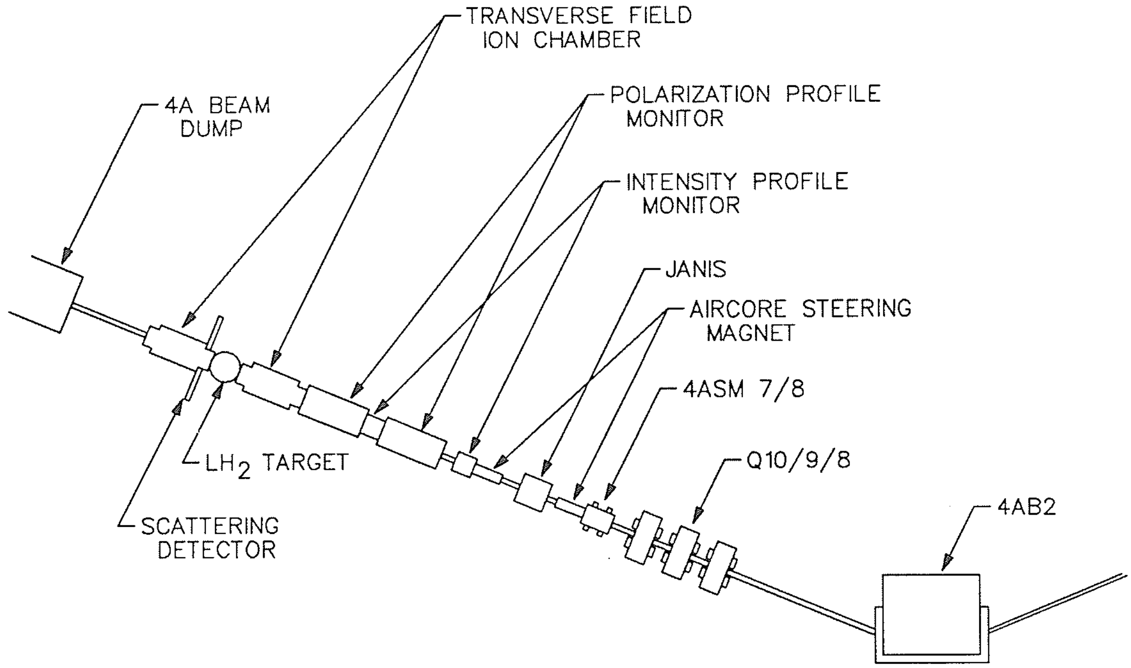

Figure 4: *The Parity violation experimental setup on TRIUMF beamline 4A. Individual items are discussed in the text.*

directions. These profile measurements are generated via secondary electron emission from 0.9 mm wide strips of aluminum foil. The monitor contains twenty-one single channels in the central region, four double channels on either side and an outer channel on each end to determine the intensity in the tails of the beam. The profiles are to be generated during the data taking phase for the parity experiment. A critical design feature of the intensity profile monitor was to minimize the amount of material in the beam to reduce multiple scattering.

There are also two polarization profile monitors which give vertical and horizontal polarization profiles in order to determine $< P_x >$, $< P_y >$, $< yP_x >$ and $< xP_y >$. By determining the polarization profiles at two locations, the effects of the extrapolated transverse polarization profiles at the scattering target can be corrected for. The polarization profile monitor uses a polyethylene blade mounted to a rotating disk. One disk is mounted with its rotation axis in the same horizontal plane as, and parallel to, the beam axis so that the blade is horizontal as it intersects the center of the beam. The other disk is mounted with its rotation axis in the same vertical plane as, and parallel to, the beam axis so that the blade is vertical as it intersects the center of the beam. The disks spin at 15 Hz; one of the eight blades passes through the beam at each spin state and data taking (for A_z) must be briefly disabled while the polarization profiles are acquired. Scintillation detectors are used to detect scattered and recoil particles from the $\vec{p}-p$ events originating from the target blade. The asymmetry of scattered particles determines the polarization, while the recoil particles from the $\vec{p}-p$ event will provide a coincidence, reducing the possibility of counting an event from $\vec{p}-^{12}C$ which would dilute the efficiency of the polarization measurement.

The target to be used for the parity experiment will contain LH_2 in a cell 40 cm in length and will require a continuous flow of LH_2 through the cell in order to keep thermal variations in the target (density fluctuations) to an absolute minimum. While all of the previous parity violation experiments were performed in either an attenuation or scattering detection mode, the TRIUMF experiment will be the first attempt to obtain A_Z for a particular energy from both modes of operation. The first phase of the experiment involves two transverse field ionization chambers which are located immediately upstream and downstream of the scattering target. The second phase of the experiment incorporates an ionization chamber scattering detector with an angular acceptance of $\theta_{lab} = 6.0^o$ to $\theta_{lab} = 41.4^o$. This is the angular range for 215 MeV at the target center that will measure an average lowest order partial wave amplitude $(^1S_0 -^3 P_0)$ contribution of zero. The scattering detector contains a central high voltage plane sandwiched upstream and downstream by sense plates, forming an annular ring for the detection of the scattered particles. Both the scattering chamber and the transmission chambers will operate with ultra-pure H_2 gas.

Up until now, only partial components and prototype monitors have been implemented for test runs. In 1991, the final design and construction of the intensity profile monitors, polarization profile monitors and transverse field ionization chambers should be complete with testing well underway. As soon as a dedicated beamline and target are completed by TRIUMF, data taking runs for the first phase of the parity experiment can begin. The final aim of the parity experiment is to measure $\delta A_z = \pm 2 \times 10^{-8}$ or better in 300 hours. This translates to a determination of h_ρ to $\pm$ 25 %, as compared to the presently accepted theoretical value which is only known to $\pm$ 300 %.

1.3 Previous Experimental Results.

A number of parity violation experiments in $\vec{p} - p$ scattering have been performed in basically four energy regions, at 15 MeV, 45 MeV, 800 MeV and 5 GeV. A general description of each is given below with the final results displayed in table 2.

At 13.6 MeV, a parity violation experiment is being performed at the BONN isochronous cyclotron [9] . A ground state atomic beam type polarized source injects protons into the cyclotron with the beam continuing through steering magnets and a spin procession solenoid to provide the longitudinal polarization. The helicity of the protons is reversed every 20 ms at the ion source, corresponding to a spin flip rate of 50 Hz. Split plate SEM monitors are used for beam position control, and a beam intensity profile

Facility	Energy	Experimental Method	Results $\times 10^{-7}$
BONN	13.6 MeV	Scattering	-1.5 ± 0.5
LANL	15 MeV	Scattering	-1.7 ± 0.8
SIN	45 MeV	Scattering	-1.50 ± 0.22
LBL	46 MeV	Scattering	-1.63 ± 1.03
Texas A & M	47 MeV	Scattering	-4.6 ± 2.6
LANL	800 MeV	Attenuation	2.4 ± 1.1
ZGS	5 GeV	Attenuation	26.6 ± 6.6

Table 2: *Results of the previous Parity Violation experiments in* $\vec{p} - p$ *scattering.*

is determined by scanning a carbon wire through the beam. The secondary electron current from the carbon wire provides a current signal versus wire position, while signals from two adjacent surface barrier detectors allow a determination of the transverse polarization of the proton beam. Ion chambers determine the scattered beam current from the 12 Atm H_2 gas scattering target, and a Faraday cup determines the beam current after the target. A comparison of the ion chamber current signal to the Faraday cup current signal for the different helicity states of the proton beam has led to the present interim experimental result of $A_Z(13.6\text{MeV}) = (-1.5 \pm 0.5) \times 10^{-7}$. The experiment is being continued at BONN with the aim of reaching a precision of $\delta A_z = \pm 0.3 \times 10^{-7}$ [10].

A 15 MeV $\vec{p} - p$ scattering experiment was performed at the Los Alamos National Laboratory tandem van de Graaff accelerator [11,12]. This experiment was also based on the scattering method, as particles scattered from an

H_2 gas target at 3 Atm for the initial phase and 6 Atm for the final phase, were collected in the scattering chamber. A Lamb shift type ion source produced polarized protons which then passed through a Wien filter to precess the spin into the longitudinal direction. By applying small additional transverse magnetic fields in the ion source, the polarization vector for the proton spin was reversed very quickly, providing a fast spin flip rate of 1 kHz for the experiment. After extraction from the accelerator, the beam passed four electrodes which intercepted part of the beam. These electrodes along with a segmented beam stop gave beam position and displacement signals which were then corrected for by steering the beam. Transverse polarization was measured by scattering from a carbon foil into two opposing quadrants of the scattering detector. The scattering detector itself initially consisted of four liquid scintillator cells equipped with three photomultiplier tubes for each cell, while a final phase of this experiment was completed using scintillating plastic. The experimentally determined value of $A_Z(15\text{MeV}) = (1 \pm 4) \times 10^{-7}$ was later improved in the final phase to $A_Z(15\text{MeV}) = (-1.7 \pm 0.8) \times 10^{-7}$.

At SIN, a polarized beam experiment was performed at 45 MeV [13] where the polarized beam was produced by an atomic beam polarized ion source and extracted from the injector cyclotron. A solenoid and dipole deflection magnet precessed the spin vector in the longitudinal direction. RF transitions acting on the neutral atomic beam in the source were used to reverse the proton polarization direction every 30 ms for a spin flip rate of 33 Hz. Two rotating carbon blade scanners provided the intensity and polarization profiles of the beam in a similar fashion to the BONN experiment. The experiment was set up to determine the helicity correlated scattering yield from a 100 Atm H_2 gas target in an ion chamber scattering detector, accepting scattered particles in the range $\theta_{lab} = 23^o$ to 52^o. The energy of 45 MeV was chosen specifically for the maximum estimated theoretical value of A_Z, and an experimental value of $A_Z(45\text{MeV}) = (-1.50 \pm 0.22) \times 10^{-7}$ was reported.

The Lawrence Berkeley Laboratory performed a parity violation experiment at 46 MeV [14] on the 88 inch cyclotron using an atomic beam type polarized ion source operating at a 60 Hz spin flip rate. After exiting the cyclotron and passing through a solenoid and bending magnet to precess the spin vector into the longitudinal direction, the beam passed through a set of secondary electron emission position monitors and polarization profile monitors. Transverse polarization profiles were determined by passing carbon strips through the beam and observing the scattering asymmetry between opposite quadrants of the scattering detector. The scattering detector contained a target filled to 80 Atm of H_2, surrounded by a He filled ion chamber that was divided into four segments. An experimental value of $A_Z(46\text{MeV}) = (-1.63 \pm 1.03) \times 10^{-7}$ was reported.

At Texas A. & M. University, a measurement of A_Z at 47 MeV was carried out on the 224 cm cyclotron at the Cyclotron Institute [15]. The source was an atomic beam type polarized ion source with longitudinal polarization produced from a downstream solenoid and bending magnet. The spin flip rate was set to 50 Hz for this experiment. Polarimeters with rotating carbon blades were implemented to provide both the transverse polarization and the intensity distributions of the beam. The scattering target was a 42 cm long H_2 gas cell at 39 Atm and was surrounded by four plastic scintillator detectors. The scattering apparatus also included a Faraday cup for determining the beam intensity. Using the scattering method, a result of $A_Z(47\text{MeV}) = (-4.6 \pm 2.6) \times 10^{-7}$ was obtained.

A further parity violation experiment was performed at LAMPF at an incident proton energy of 800 MeV [16]. The Lamb shift type polarized ion source was operated at a spin flip rate of 30 Hz and a Wien filter precessed the spin into the longitudinal direction before acceleration. Wire chambers were used to measure beam intensity profiles, and transverse polarization information was obtained from two polarimeters, one using the LH_2 main scattering target, and a second following the LH_2 target using an independent scanning target. Using two transverse field ionization chambers, one upstream of the target and one downstream, the scattered fraction of beam from the LH_2 target was determined. The resulting longitudinal analyzing power from this attenuation experiment was determined to be $A_Z(800\text{MeV}) = (2.4\pm1.1)\times10^{-7}$.

Also based on the attenuation method was a parity violation experiment at the Argonne National Laboratory ZGS synchrotron facility with a polarized beam of 5 GeV protons [17]. Using an atomic beam type polarized ion source, a vertically polarized proton beam was produced and the spin was precessed with a bending magnet used for an upward bend of the beamline. A spin flip rate of 0.3 Hz was achieved while reversing the spin vector for each beam pulse. Only vertical beam displacements were corrected for by an upstream steering magnet, based on a correction signal produced from two scintillator wedges which determined the vertical position asymmetry of the beam. Because the synchrotron produces such a narrow beam spot, the experiment becomes insensitive to $< xP_y >$ and beam profiles are not required. Scintillation detectors were also used to produce transverse polarization measurements. Two transmission measurements were performed. One with two scintillator blocks, each viewed by four photomultiplier tubes, and another with ionization chambers. Each type of transmission detector was located upstream and downstream of a 81 cm H_2O target. A value of $A_Z(5\text{GeV}) = (26.5 \pm 6.6) \times 10^{-7}$ was obtained.

Shown in fig. 5 are the best results for the four energy regions. The solid

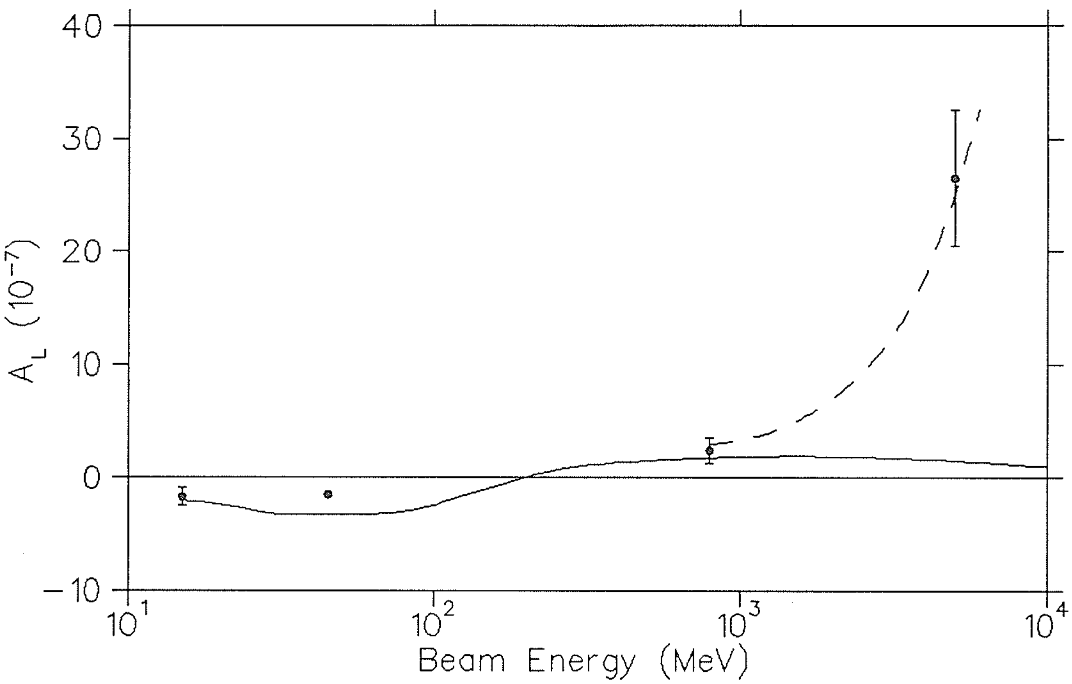

Figure 5: *Previous experimental results for p-p scattering Parity Violation experiments. The solid curve represents the theoretical prediction of the meson-exchange model and the dashed curve represents quark model calculations.*

curve is the theoretical prediction of the meson-exchange model [1] and predicts A_Z reasonably well for energies up to 800 MeV. Above 800 MeV, theory and experiment disagree, at least for the meson-exchange model. Calculations at the quark level [18] agree rather well with experimental results at 800 MeV and 5 GeV as shown by the dashed curve in fig. 5 but extrapolate to unreasonable predictions at lower energies.

2 Monitor Design Specifications.

There are three functions that the beam intensity profile monitor was designed to perform. The first is the ability to provide an asymmetry signal that is proportional to the displacement of the beam from a fixed axis. This signal will be used in a fast feedback servo loop to steer the beam and correct for any displacements from this axis. It is also a requirement that the position axis can be moved with respect to the other parity apparatus. It is then possible to relocate the monitor and investigate the sensitivity of other components of the apparatus to beam excursions away from the fixed axis. For the purpose of these tests and for the actual data taking runs, it is necessary to have the beam centroid stable to within $\pm$ 10 μm [19] for frequencies below 1 Hz. This criterion was set by assuming a worst case transverse polarization for the experiment as $\overline{P_t} = 0.01$. This requirement will determine restrictions on the stability of the beam and the mechanical tolerances of the position control mechanism discussed in the following section.

The second function is to provide an intensity profile in both x and y directions, perpendicular to the beam. From these intensity distributions, it is necessary to be able to determine the beam centroids to within $\pm$ 10 μm [19] after 1 hour of data taking. It is not necessary for the position of the profile apparatus to be repositioned as it was for the beam positioning apparatus. Thus, it was decided that the two components of the monitor be mechanically isolated from one another.

The third function of the SEM monitor is to produce a current signal which is linear with respect to the beam intensity. Section 2.1 discusses the two modes of operation that were considered and examines the linearity of each method of operation. Calculations in following sections were then performed assuming a linear monitor response. It should also be noted that all design specifications are based on a 500 nA proton beam and that all widths are expressed as the full width $\frac{1}{e}$ of the beam distribution. Systematic errors such as non-linear monitor response and changes in secondary electron efficiency of the foil surface will be evaluated in section 6.3 where gain correction factors will determine if there is any position or intensity dependence of the monitor.

2.1 Modes of Operation.

As an ion projectile passes through matter, its energy loss can be expressed in the form of the Bethe-Bloch eq. [20],

$$\frac{dE}{dx} = \frac{DZ_{med}\rho_{med}}{A_{med}} \left(\frac{Z_{inc}}{\beta}\right)^2 \left[\ln\left(\frac{2m_e\gamma^2\beta^2c^2}{I}\right) - \beta^2 - \frac{\delta}{2} - \frac{C}{Z_{med}}\right](1+\nu) \quad (3)$$

where $D = 4\pi N_A r_e^2 m_e c^2 = 0.3071$ MeV cm^2/g. Z_{med} and A_{med} are the charge and mass numbers of the medium and ρ_{med} its mass density. I is characteristic of the electronic binding energy of the medium and can be approximated by $I \cong 16(Z_{med})^{0.9}$ eV and δ, C and ν are higher order corrections. δ represents a density effect and is non-negligible for highly relativistic particles in a dense medium, C represents shell corrections and ν contains corrections due to higher order electrodynamics. The energy is transferred to the medium as a result of excitation and ionization processes. For the beam intensity profile monitor, two modes of particle detection were evaluated. The first mode of operation was a gas ionization monitor which collected ions created as the projectile passed through a gas region, while the second mode of operation would collect the secondary electrons emitted from a metallic surface placed in the beam. The following sections discuss these modes of operation.

2.1.1 Gas Ionization.

Many types of particle detector are based on the production of ion pairs due to the passage of a particle through the detector. As the projectile passes through the gas, energy is lost to the gas, creating ions which are collected on sense wires. To determine the number of ion pairs produced per proton (η_{ip}) in H_2 gas, the Bethe-Bloch estimate of the total energy lost in the gas is needed ($\Delta E = \frac{dE}{dx} = 8\frac{\mathrm{MeV}}{\mathrm{g\ cm^{-2}}}$ for 230 MeV protons) as well as the average energy required to produce one ion pair in hydrogen gas ($w_{H_2} = 37eV$), available in most physical tables. Thus,

$$\eta_{ip} = \frac{\Delta E}{w_i}. \tag{4}$$

As an example, 230 MeV protons will liberate approximately 18.1 ion pairs per proton, per cm of H_2 gas at atmospheric pressure and by adjusting the size of the gas region or the pressure, the gas gain (ion pairs per proton) of the monitor can be controlled.

The detector consists of a harp of wires at equal spacing and is sandwiched between two high voltage foils. If a particle passes within the region of a sense wire, the charge of the ion pairs is collected on that wire and passed to the detector electronics. The polarity of the monitor only affects the sign of charge collected on the sense wires. The difference is that electrons will drift much faster through the sense region gas than will the positive ions.

An analytic expression for the periodic field produced by a series of wires can be solved by standard electrostatic techniques. Erskine [21] has derived an approximate expression for the field as well as calculating field distortions due to wire displacements. The monitor was constructed as shown in fig. 6 with s as the wire spacing and l the wire harp to voltage plane gap. By using the boundary condition that the high voltage planes be at a potential V_o and defining the coordinate system with x in the direction of s and y in the direction of l, the electric potential V is given by:

$$V(x,y) = \frac{CV_o}{4\pi\epsilon_o}\left(\frac{2\pi l}{s} - ln\left[4\left(sin^2\frac{\pi x}{s} + sinh^2\frac{\pi y}{s}\right)\right]\right) \tag{5}$$

and the magnitude of the electric field is given by:

$$E(x,y) = \frac{CV_o}{2\epsilon_o s}\left(1 + tan^2\frac{\pi x}{s}tanh^2\frac{\pi y}{s}\right)^{\frac{1}{2}}\left(tan^2\frac{\pi x}{s} + tanh^2\frac{\pi y}{s}\right)^{-\frac{1}{2}} \tag{6}$$

where C is the capacitance per unit length of wire,

$$C = \frac{2\pi\epsilon_o}{\left(\frac{\pi l}{s}\right) - ln\left(\frac{2\pi a}{s}\right)} \tag{7}$$

and $a \equiv$ wire radius. The resolution of the monitor can be increased by decreasing s, but wire spacings less than 1.0 mm are mechanically difficult to produce. By increasing l, the gas gain of the monitor can be increased, but the applied potential must also be increased to compensate for the decrease in the electric field. The upper limits of l are basically due to the maximum high voltage that can be applied and overall dimensions of the monitor, the latter being of more concern for this particular case.

During operation, the electrons are in an electric field so they are accelerated in the direction of the applied field. Since the electrons are also in gas, they soon collide with neutral gas molecules losing energy through

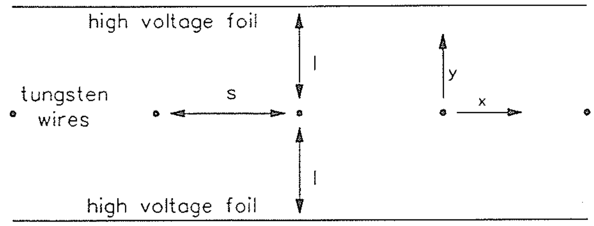

Figure 6: *Schematic setup of the wire harps and high voltage planes.*

rotational and vibrational modes of the molecules. If the electron has been accelerated to a high enough energy since the last collision, it ionizes the neutral gas molecule. Ionization would result in an increase in total charge collected and would be indistinguishable from an increase in the number of incident protons. It is therefore important that the applied potential be kept below the critical value that accelerates the electron over the ionization energy between collisions. This process is known as avalanche multiplication.

To determine the critical potential for hydrogen, Sauli [22] sets the reduced electric field for the onset of ionization by the accelerated electrons at $30 \times P$ volts cm^{-1} mm Hg^{-1}. The tungsten wire radius is 6 μm, the monitor wire spacing is 1 mm, and if the G10 boards are mounted without any spacers, the half gap length is set at the G10 board thickness of 1.5 mm. For this particular setup, the electric field at the wire surface is,

$$E_{max}(x = 0, y = a) = \frac{\pi V_o coth\left(\frac{a\pi}{s}\right)}{s\left(\frac{\pi l}{s} - ln\left(\frac{2\pi a}{s}\right)\right)} \tag{8}$$

$$= 200\ V_o\ \text{cm}^{-1}. \tag{9}$$

We must also keep the maximum electric field

$$E_{max} < 30 \times P\left(\text{volts cm}^{-1}\ \text{mm Hg}^{-1}\right) \tag{10}$$

to avoid avalanche multiplication. To operate at 1.0 Atm (760 mm Hg), we require

$$E_{max} < 22500 \text{ volts cm}^{-1} \quad (11)$$

$$200\ V_o \text{ cm}^{-1} < 22500 \text{ volts cm}^{-1} \quad (12)$$

$$V_o < 110 \text{ volts.} \quad (13)$$

Another problem to consider with gas operation is the possibility of glow discharge. Townsend [23] shows the breakdown voltages for H_2 gas which can be approximated to first order by the straight line fit

$$E_{spark} = 33P(\text{volts cm}^{-1}\text{ mm Hg}^{-1}) + 250(\text{volts cm}^{-1}). \quad (14)$$

If the applied voltage is kept below the critical value for the onset of ionization by accelerated electrons, glow discharge is not a problem.

Sauli also considers the tension T required on the wires. Since the wire is in a position of instability, if one wire is displaced by a small amount towards a high voltage plane, its neighbouring wires will be repelled towards the other high voltage plane. From his results,

$$T \geq T_c = \frac{1}{4\pi\epsilon_0}\left(\frac{CV_oL}{s}\right)^2. \quad (15)$$

where L is the total wire length. For the central wire of length 87 mm and an applied voltage of 110 volts,

$$T_c \simeq 10^{-7}\text{N}. \tag{16}$$

This is not a concern for the length of wire used in this monitor. We now have all the basic criteria to begin construction of the wire harps.

Although the gas ionization mode of operation was tested in the beam intensity profile monitor, it was decided that the linearity of this mode of operation was unsatisfactory for the parity violation experiment. Reports [24] from the Los Alamos group stated that the gas profile monitors used in the 800 MeV LAMPF experiment were operating dangerously close to the limit for linear response with respect to beam current fluctuations. The problem arose due to space charge effects. These effects would be more severe for the TRIUMF experiment since the energy loss for 230 MeV protons in hydrogen gas ($(\frac{dE}{dx})_{H_2} = 8$ MeV g^{-1} cm^{-2}) is greater than that for 800 MeV protons ($(\frac{dE}{dx})_{H_2} = 4.5$ MeV g^{-1} cm^{-2}), and the TRIUMF experiment operates at 500 nA dc beam while the LAMPF experiment used a pulsed beam with a peak intensity of only 80 nA.

A calculation of space charge was performed for the monitor geometry described above. Using a 500 nA beam with a 20 mm full width $\frac{1}{e}$, the total current on the wire at the enter of the beam was determined. The signal current collected can be expressed as

$$I = n_+ e v_+ A_{surface} \tag{17}$$

where n_+ is the number density of positive ions collected on the wires, e is the ion charge, v_+ is the velocity of the positive ions and $A_{surface}$ is the surface area through which the ions flow. Since the velocity of the ions can be expressed as the product of the mobility and the electric field ($v_+ = \mu_+ E(r)$) and the current collected on the wire from the beam is a constant, the number density of ions can be expressed as a function of the electric field,

$$n_+(r) = \frac{I_{wire}}{e\mu_+ E(r) A} \tag{18}$$

$$= \frac{I_{wire}}{2\pi l e \mu_+ E(r) r}. \tag{19}$$

The electric field near the wire can be approximated by $E(r) = \frac{CV_o}{2\pi\epsilon_o}\frac{1}{r}$, and the fraction of charge screened at a distance R can be expressed as

$$Q = \int_a^R \frac{n_+(r)}{n_-} 2\pi r l dr \tag{20}$$

where n_- is the charge density located on the wire due to the applied potential V_o. Evaluation of this integral shows that 1 % of the charge on the wire is screened at 0.14 mm from the wire while 10 % of the charge is screened at a distance of 0.45 mm from the wire. Since the existence of space charge will decrease $E(r)$, the true electric field (of which n_+ is inversely proportional) should increase the problem of space charge, and the numbers determined here can be considered an under estimate of the true space charge problem. Clearly, this demonstrates that a gas ionization monitor would not be able to operate at the beam intensity proposed for the parity experiment.

2.1.2 Secondary Electron Emission.

An alternative to the detection of particles through a gas is the use of secondary electron emission (SEM). The energy lost from the incident proton is transferred to atoms of a metal foil as a result of excitation and ionization processes, producing secondary electrons which continue collisions, losing energy in the process. If secondaries are produced close to the surface of the metal, it is possible for the electrons to escape the medium by what is referred to as secondary electron emission. This mode of operation would require the replacement of the 6 μm radius tungsten wires with aluminum foil strips of width 0.90 mm. These strips increase the surface area for secondary electron emission by a factor of

$$\frac{0.90 \text{ mm}}{\pi \times 6 \ \mu\text{m}} = 50 \tag{21}$$

compared to the surface area of the tungsten wires.

The energy lost by an incident ion is transferred to the electrons of the medium through two elementary electron emission mechanisms as discussed by Sternglass [25] resulting in a continuous spectrum of secondary electrons. The first mechanism is distant inelastic electron collisions and the second is "free" electron elastic collisions. The first case creates low energy electrons peaked around 10 - 25 eV (independent of the incident ion energy) which can be scattered through large angles after one or two collisions in the material and thus can be considered to be emitted isotropically. These secondary electrons are emitted from a typical depth of 10^{-5} to 10^{-6} mm. The second case produces high energy electrons referred to as δ-rays of energies up to 0.54 MeV for a 230 MeV proton beam as derived from the relativistic kinematics equation for elastic scattering [27],

$$T_e(\theta) = \frac{2m_e(E_p^2 - M_p^2)cos^2(\theta)}{(E_p + m_e)^2 - (E_p^2 - M_p^2)cos^2(\theta)} \tag{22}$$

where m_e is the electron mass, M_p is the proton mass, $E_p(= T_p + M_p)$ is the total energy of the proton with T_p its kinetic energy and θ the direction of the recoil electrons with respect to the incident ion trajectory. The maximum energy transferred to the δ-ray is determined by setting $\theta = 0^o$, then eq. 22 simplifies to

$$T_{e_{max}}(0) = \frac{2m_e\beta^2\gamma^2c^2}{1 + 2\gamma\frac{m_e}{M_p} + \left(\frac{m_e}{M_p}\right)^2} \tag{23}$$

where β and γ are the relativistic parameters of the proton.

To determine $\frac{dN}{dx}(\mathrm{cm}^{-1})$, the number of δ-rays produced as the proton passes through a foil, one can integrate [27] the following equation:

$$\frac{d^2N}{dT_e dx} = \frac{1}{2}D\left(\frac{Z_{med}}{A_{med}}\right)\left(\frac{Z_p}{\beta}\right)^2 \rho_{med}\frac{1}{T_e^2}F \tag{24}$$

over the electron energy range dT_e where $D = 0.3071$ MeV cm^2 g^{-1}, Z_{med} and A_{med} are the foil material charge and mass numbers, ρ_{med} the foil material density and $Z_p = 1$ as the proton charge number. The factor F depends on the incident projectile. For protons,

$$F_{proton} = 1 - \beta^2\frac{T_e}{T_{e_{max}}} + \frac{1}{2}\left(\frac{T_e}{T_p + M_p}\right)^2. \tag{25}$$

The energy deposited in each of the two electron emission mechanisms is roughly equal [25], so the number of δ-rays is less than that of secondaries. However, δ-rays can produce more secondary electrons as they continue to pass through the medium. These δ-rays are emitted primarily in the forward direction and when estimating the secondary electron yield from a foil, they must be taken into consideration. Section 5.2.3 also discusses some observations made of these δ-rays. It has also been found that the yield of secondary electrons depends more on characteristics of the projectile ion and the surface quality of the medium than on the atomic properties of the medium.

The main problem with operation of a monitor using secondary electron emission is the fact that the yield for 230 MeV protons passing through aluminum (similar for many metals) is only 0.05 per proton, per surface as compared to 18.1 per proton, per cm for gas as discussed earlier. To operate in this mode requires higher gain electronics with lower noise.

The last concern was the linearity of the SEM device with respect to changes in the beam current. As was seen with the gas ionization monitor in the previous section, non-linear behavior is a result of space charge buildup around the wires. Since the SEM mode of operation is a surface effect, causes of non-linear monitor response would instead be a result of changes in efficiency of the foil surfaces. This would be possible if a change in temperature of the metal foil caused by an increase in beam current in turn caused a systematic change in the foil surface efficiency. However, no experimental results or theoretical models have suggested that the secondary electron efficiency of metals varies significantly with temperature. Secondary electron emission was thus the proposed mode of operation for the intensity profile monitor based primarily on its improved linearity over a gas operated monitor.

2.2 Split Plate Monitor.

For the position control of the beam, split plate foils are used. A foil with a split down the center, providing a left and right signal plate, is sandwiched between two high voltage foils at an applied potential. The split plate monitor provides both horizontal and vertical asymmetry signals to the upstream aircore steering magnets. These splits define a cross-hair on which the steering magnets position the beam. The horizontal asymmetry signal is defined as

$$\epsilon_{L,R} = \frac{L - R}{L + R} \tag{26}$$

with a similar vertical asymmetry calculated from the up and down plates. Positioning the beam centroid at the cross-hair reference point of the monitor is achieved by forcing the vertical and horizontal asymmetries to zero, applying the appropriate steering signals to the upstream aircore steering magnets. Note that the above asymmetry value is independent of the beam current. However if the beam current should drop below a preset level, the loop must automatically be disabled to eliminate response to an undefined asymmetry signal. The final experimental setup calls for two split plate monitors, both providing vertical and horizontal asymmetry signals to the upstream aircore steering magnets. Positioning the two split plate monitors along the beam defines the entire beam axis.

A design consideration for the split plates was the effect of the width of the split between two plates. Even if the servo loop is successful in securing the position such that a beam of fixed shape does not move from the predefined axis, one must consider the effect of a change in the beam shape. The only parameter controlled by this device is the median of the beam x_m where

$$\int_{-\infty}^{x_m-\delta} I(x)dx = \int_{x_m+\delta}^{\infty} I(x)dx. \tag{27}$$

$I(x)$ represents the beam distribution and the split plate separation is 2δ. If the beam profile is symmetric, the beam centroid defined as

$$<\overline{x}>= \frac{\int_{-\infty}^{\infty} xI(x)dx}{\int_{-\infty}^{\infty} I(x)dx} \tag{28}$$

is controlled. If the beam is not symmetric, then this is not the case. Depending on the degree of skewness, there is an error introduced when assuming that the beam centroid and beam median coincide. The next step was to determine the effect of changing the split plate width on the validity of approximating the beam median for the beam centroid for various degrees of skewness.

Three possible cases modelling the beam skewness were used in an attempt to determine the effect of the split plate separation on the error arising from equating the beam median to the centroid. The first case was to introduce a factor $(1 + \beta x)$ to a Gaussian profile, giving

$$I(x) = I_o(1 + \beta x)e^{-\alpha x^2} \tag{29}$$

where $\alpha = 1/x_o^2$, x_o ($\frac{1}{e}$ half width) $\simeq$ 10 mm. The centroid of this distribution is

$$\overline{x} = \frac{\beta}{2\alpha} \tag{30}$$

and the median of the beam distribution, as calculated from eq. 27, is determined from the relation

$$erfc(x_m - \delta) - erfc(x_m + \delta) = \frac{\beta}{\sqrt{\pi\alpha}}\left(e^{-\alpha(x_m-\delta)^2} - e^{-\alpha(x_m-\delta)^2}\right). \qquad (31)$$

The second case considered was the superposition of two Gaussians with relative intensities h and displaced by a distance a,

$$I(x) = I_o(e^{-\alpha x^2} + he^{-\alpha(x-a)^2}) \qquad (32)$$

with a centroid of

$$\overline{x} = ha/(1+h) \qquad (33)$$

and a median x_m that satisfies the equation

$$erfc(x_m - \delta) - erfc(x_m + \delta) = h\left(erfc(x_m + \delta - a) - erfc(x_m - \delta - a)\right). \qquad (34)$$

The third and final case was to assume that the left half and right half of the beam each had a different width,

$$\begin{aligned} I(x) &= I_o e^{-\alpha_1 x^2} \quad x < 0, && (35)\\ &= I_o e^{-\alpha_2 x^2} \quad x > 0, && (36) \end{aligned}$$

where $\alpha_n = 1/x_n^2$ and $x_{1(2)} = x_o + (-)skew$. The centroid for case 3 is

$$\overline{x} = \frac{1}{\sqrt{\pi}}\left(\frac{x_2^2 - x_1^2}{x_1 + x_2}\right) = \frac{1}{\sqrt{\pi}}(x_2 - x_1) \qquad (37)$$

and a median that satisfies

$$\sqrt{\alpha_2}\, erfc(x_m - \delta) = \sqrt{\alpha_1}\, erfc(x_m + \delta). \tag{38}$$

In all of the above cases, the median of the beam x_m was determined from eqn 27. The intent was to determine what value of δ was sufficient such that the error in determining the beam centroid from the median was reduced to a minimum. After varying the parameters through realistic values for the beam profiles, it was concluded that the actual separation that would minimize the error of associating the beam median to the beam centroid depends on the method used to model the profile skewness. For case one, by varying the parameter β from 0 to 0.5, it was observed that a value of $\delta = 10-12$ mm was best. For case two, by varying h and a, the optimum value of $\delta = 6-8$ mm. For case 3, there was no reasonable value of δ that would significantly reduce the error.

Due to the inconclusive results above, the deciding factors for the determination of δ were taken as the signal to noise ratio of the monitor and the linearity of the asymmetry signal with respect to beam excursions away from the center of the monitor. For these calculations, again a Gaussian beam of 20 mm full width $\frac{1}{e}$ was assumed. Also required for the signal to noise ratio calculations was the fact that the experiment will be operating at 500 nA of beam current. A typical rms noise signal for one of the split plate amplifier channels ranges from $\sigma = 10$ pA to 50 pA. Using these values, a determination of the split plate asymmetry signal to noise of $\frac{\epsilon}{\sigma_e}$ for a beam position shift of 0.1 mm gives the results in table 3. These results show that the signal

Noise	Signal to Noise $\frac{\epsilon}{\sigma_e}$			
σ_e	$\delta=0$mm	$\delta=2$mm	$\delta=4$mm	$\delta=6$mm
10 pA	13.5	12.8	11.5	9.5
50 pA	2.5	2.4	2.2	1.9

Table 3: *Signal to noise calculations with split plate separation parameter* δ.

to noise ratio is best and remains relatively unchanged for small values of the split plate separation. For the beam position linearity calculations, if the position asymmetry signal ϵ is calculated from eq. 26 as the beam is moved across the split plates, the plot in fig. 7 is obtained. This plot shows the value of ϵ for a split plate separation of $\delta = 0$ mm and $\delta = 5$ mm. It can be seen in the plot that the linearity of the asymmetry signal for beam excursions near the center of the monitor are improved by making δ as small as possible.

Although there is no limit placed on δ to reduce the error in equating the beam centroid to the beam median, both the linearity and the signal to noise ratio would suggest a value of δ as small as possible. The final separation of the split plates was therefore chosen by practical considerations to be 1.0 mm. This kept the split plates close to the optimum for linearity and signal to noise considerations and allowed the foils to be mounted with little difficulty. A measurement of the actual location and width of the split between the plates was not critical, since all measurements of beam position will be provided via the monitor position readout, but the split plates were mounted with consideration to ensure that the split was parallel. If the splits are misaligned, then beam motion in one orthogonal direction could couple to the split plates in the second orthogonal direction, producing an apparent motion of the beam in the second split plate asymmetry signal.

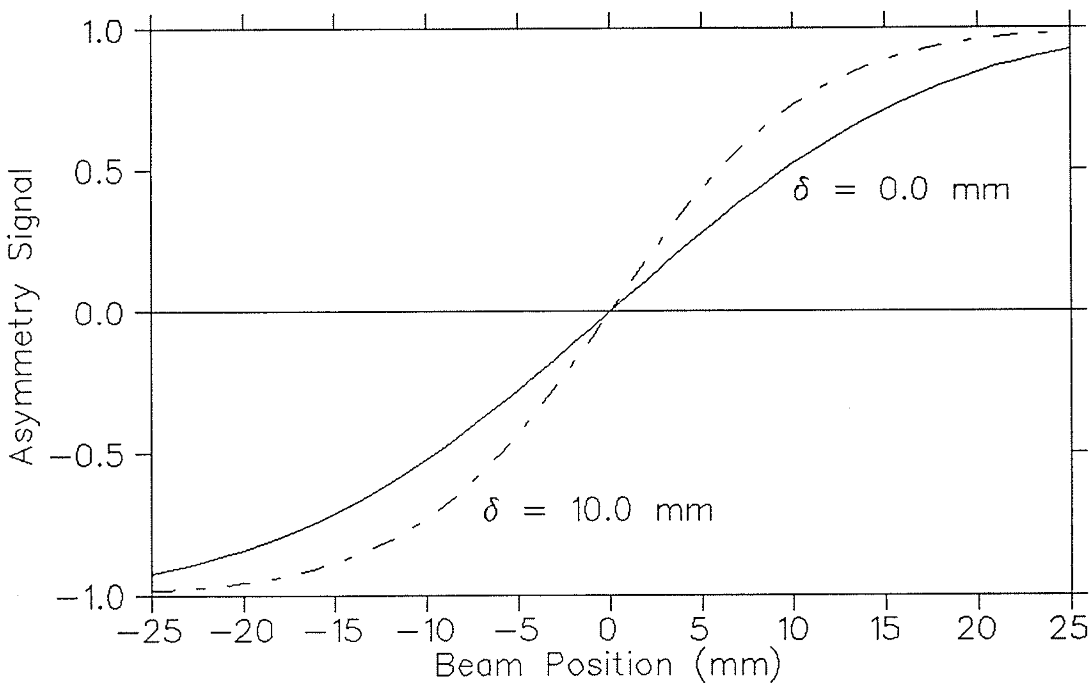

Figure 7: *Position asymmetry signal for a 20 mm full width* $\frac{1}{e}$ *beam for the split plate separation parameter* $\delta = 0$ *mm and 10 mm.*

The method of determining the fixed axis as defined by the split plates would entail moving both split plate monitors in order to vary the axis of the beam through the other parity apparatus. Although the rest of the apparatus is designed cylindrically symmetric, it is necessary to determine the axis through the apparatus that minimizes the sensitivity to beam position fluctuations. The split plates are necessary to lock the beam on axis in order to perform the sensitivity measurements. This "neutral" axis will define the optimum position axis on which to operate the experiment.

2.3 Intensity Profile Monitor.

The only requirement specified at the beginning of this section regarding the intensity profile monitor was that the monitor be able to determine the centroid of the beam to within $\pm$ 10 μm in one hour, assuming 500 nA beam of 20 mm $\frac{1}{e}$ full width. This single requirement imposed limitations on the four parameters: electronic noise, electronic pedestal values, error in determining foil strip locations and the gain calibration factors. The following discussion determines the requirements imposed on these parameters.

In addition to the four sources of random error listed above that contribute to the centroid error, there may be additional problems due to variation in the width and surface efficiency of the foil strips. These effects are included in the determination of the individual channel gain factors. There is also a problem with using the explicit form of the discrete distribution. If the profile of the beam is offset from the central channel, an error is introduced. Falk [26] gives a method to correct for this error by applying a simple algorithm. However, the centroid value still depends upon the upper and lower limits of the calculations (i.e. if the tails of the distribution are removed). In this case, it might be more advantageous to fit the discrete distribution with a function and to determine the beam centroid (and other moments of the beam) from this fit. For the following calculations, the discrete distribution is used to provide restrictions on the physical parameters listed above.

The centroid of the discrete distribution can be determined from the equation

$$< \overline{x} >= \frac{\sum_i x_i g_i I_i}{\sum_i g_i I_i} \tag{39}$$

where x_i is the position of the i^{th} foil strip, g_i is the gain factor of the i^{th} strip and I_i is the total current from the strip before electronic amplification. For this case, the total current reading is the sum of the SEM current produced by the beam I_i', the electronic noise I_{e_i} and the electronic bias current (pedestal) I_{p_i},

$$I_i = I_i' + I_{e_i} + I_{p_i}. \tag{40}$$

The total statistical error for the centroid is estimated by

$$\begin{aligned} \sigma^2_{<\overline{x}>} \quad = \quad & \sum_{all\ channels} \sigma_g^2 \left(\frac{\partial < \overline{x} >}{\partial g} \right)^2 + \sigma_{I_e}^2 \left(\frac{\partial < \overline{x} >}{\partial I_e} \right)^2 + \sigma_{I_p}^2 \left(\frac{\partial < \overline{x} >}{\partial I_p} \right)^2 + \\ & \sigma_x^2 \left(\frac{\partial < \overline{x} >}{\partial x} \right)^2 . \end{aligned} \tag{41}$$

Each partial differential in the equation above is solved as,

$$\frac{\partial < \overline{x} >}{\partial g_i} \quad = \quad \frac{I_i(x_i - < \overline{x} >)}{\sum_i g_i I_i}, \tag{42}$$

$$\frac{\partial < \overline{x} >}{\partial I_{e_i}} = \frac{g_i(x_i - < \overline{x} >)}{\sum_i g_i I_i}, \quad (43)$$

$$\frac{\partial < \overline{x} >}{\partial I_{p_i}} = \frac{g_i(x_i - < \overline{x} >)}{\sum_i g_i I_i}, \quad (44)$$

$$\frac{\partial < \overline{x} >}{\partial x_i} = \frac{g_i I_i}{\sum_i g_i I_i}. \quad (45)$$

The final equation for the centroid error is

$$\sigma^2_{<\overline{x}>} = \frac{\sum_i \sigma^2_{g_i} I_i^2 (x_i - < \overline{x} >)^2}{(\sum_i g_i I_i)^2} + \frac{\sum_i \sigma^2_{I_{e_i}} g_i^2 (x_i - < \overline{x} >)^2}{(\sum_i g_i I_i)^2} + \frac{\sum_i \sigma^2_{I_{p_i}} g_i^2 (x_i - < \overline{x} >)^2}{(\sum_i g_i I_i)^2} + \frac{\sum_i \sigma^2_{x_i} g_i^2 I_i^2}{(\sum_i g_i I_i)^2}. \quad (46)$$

Next, assume that $\sigma_{I_{e_i}}$, $\sigma_{I_{p_i}}$ and σ_{x_i} are the same for all channels and that the value of σ_{g_i} depends upon the gain matching algorithm. In fact, it is possible to match the gains of the central channels much more accurately than the outer channels, but for the purpose of these calculations, the worst case where all channel gains are matched to the accuracy attainable for the outermost channels was assumed. For the purpose of estimating $\sigma_{<\overline{x}>}$, one can set $g_i = 1.0$ and $< \overline{x} > = 0$ mm. Finally, since the SEM coefficient for the aluminum foil is ~ 5 % per proton, per surface, the total SEM current is $500 \times 2 \times 0.05 = 50$ nA from the two foil surfaces. The equation for the centroid error then reduces to

$$\sigma^2_{<\overline{x}>} = \frac{\sigma_g^2 \sum_i x_i^2 I_i^2}{(50\text{nA})^2} + \frac{\sigma^2_{I_e} \sum_i x_i^2}{(50\text{nA})^2} + \frac{\sigma^2_{I_p} \sum_i x_i^2}{(50\text{nA})^2} + \frac{\sigma_x^2 \sum_i I_i^2}{(50\text{nA})^2}. \quad (47)$$

A Gaussian of 20 mm full width $\frac{1}{e}$ was used to solve for x_i and I_i. The sums are over the entire 31 channels of the monitor. Note that the second and third terms in eq. 47 involving $\sum_i x_i^2$ become very large for the contributions from the outer channels. This simply means that any noise or change in pedestal that is present on the outer channels significantly contributes to the centroid error. One then finds $\sum_i I_i^2 = 80.6$ nA^2, $\sum_i x_i^2 = 2480$ mm^2 and $\sum_i x_i^2 I_i^2 = 1960$ mm^2 nA^2 so that eq. 47 becomes

$$\sigma^2_{<\bar{x}>} = 0.8\sigma_g^2 \text{ mm}^2 + 1.0\sigma_{I_e}^2 \text{ mm}^2 \text{ nA}^{-2} + 1.0\sigma_{I_p}^2 \text{ mm}^2 \text{ nA}^{-2} + 0.03\sigma_x^2. \quad (48)$$

Now, the total contribution must be less than (10 μm)^2 for the realistic values used. The specifications that were finally decided upon were $\sigma_g = \pm$ 1.0 %, $\sigma_{I_e} = \pm$ 1.0 pA, $\sigma_{I_p} = \pm$ 1.0 pA and $\sigma_x = \pm$ 5.0 μm. Substituting into eq. 48 gives

$$\begin{aligned} \sigma^2_{<\bar{x}>} &= 8.0 \times 10^{-5} \text{ mm}^2 + 1. \times 10^{-6} \text{ mm}^2 + 1. \times 10^{-6} \text{ mm}^2 + 8. \times 10^{-7} \text{ mm}^2 \\ &= 8.3 \times 10^{-5} \text{ mm}^2. \quad (49) \\ \sigma_{<\bar{x}>} &= 9.1 \times 10^{-3} \text{ mm} \\ &= 9.1\ \mu\text{m} \quad (50) \end{aligned}$$

which is below the required ± 10 μm.

The resulting specifications for the profile monitor are that gains must be calibrated to within ± 1.0 %, the pedestals determined to within ± 1.0 pA, foil strip positions determined to within ± 5.0 μm and the electronic noise (in one hour) reduced to within ± 1.0 pA. This last requirement translates to 1.0 pA $\times\sqrt{3600} = 60$ pA noise in a one second measurement. These requirements complete the set of monitor specifications for the design described in the following section.

3 Monitor Design and Construction.

The prototype Beam Intensity Profile Monitor was designed in such a way that an existing monitor could be modified to help reduce cost and construction time. The first prototype monitor which was tested was a reproduction of the existing TRIUMF monitor design for 4AM4.4 and 4AM4.7, which have been in operation and had the capability of remotely relocating the position of the monitor with respect to the beam. The mechanical accuracy of this monitor proved to be unacceptable for the experiment, and it was decided that a dedicated monitor would have to be designed specifically as the Beam Intensity Profile Monitor.

The latest prototype monitor was designed to fit within the standard TRIUMF monitor box. This monitor box is used by a number of monitors on site and allows ample room for the required motion control mechanisms. The construction was further simplified by acquiring the existing monitor 1AM9 which was no longer in use and could be modified to provide the required motion control. Existing on the monitor box was an in/out controller capable of rotating a monitor cell in and out of the beam. Fig. 8 shows the monitor cell mounted on a hollow, vertical shaft where electrical feedthroughs enter the cell. The cell is a 15 cm $\times$ 15 cm $\times$ 3 cm box cut from a solid piece of aluminum. The monitor cell provided a rigid structure onto which a positioning device was mounted and the aperture of this cell was to coincide with the inner radius of the beam pipe of 87 mm.

Allowances were made such that the monitor could operate in both gas ionization and secondary electron emission modes. Initial tests were performed using gas ionization, but this mode of operation failed to provide a linear signal response with respect to beam current as discussed in sec-

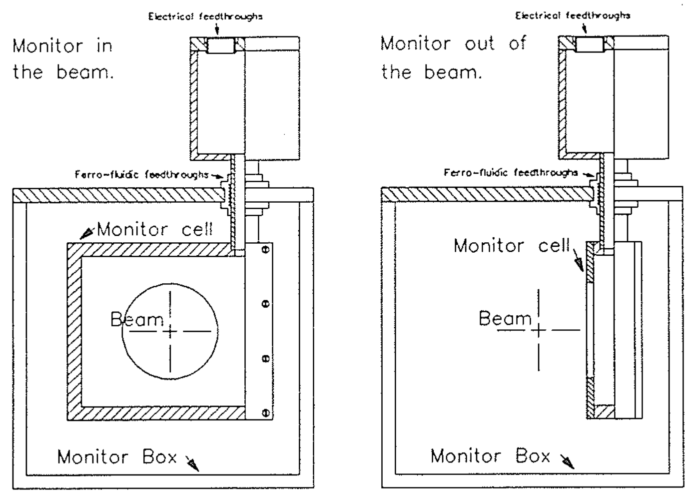

Figure 8: *TRIUMF monitor 1AM9 which was modified to contain the Beam Intensity Profile Monitor control mechanism.*

tion 2.1.1. The secondary electron emission mode proved desirable and was adopted as the final mode of operation. In the following sections, the modifications made to the internal cell for the two modes of operation are addressed.

3.1 Construction of Plate Pack Assemblies.

The first construction task was to create a plate pack that would supply a frame on which the high voltage planes, split plates, sense wires and foil strips could be mounted. The final plate pack assembly with both the split plates and the profile pack is shown in fig. 9. A material frequently used for these support frames is G10, which is a fiberglass board material available in standard thicknesses from $\frac{1}{32}$". Frames for the monitor were originally constructed with $\frac{1}{32}$" thick G10, but it was found that these frames deformed when secured to the monitor. The stronger $\frac{1}{16}$" G10 boards were then used and held securely with little deformation.

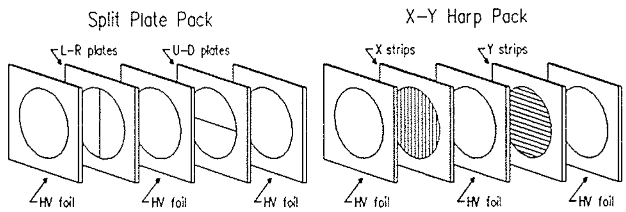

Figure 9: *Assembly of the Split Plate and Foil Strip pack G10 frames.*

The G10 boards are supplied with a layer of copper coating onto which a printed circuit board is drawn. The printed circuit board for foil strip planes is shown in fig. 10 and contains pads 0.7 mm in width and 6 mm in length. The wire harp planes are very similar, but required a pad at both ends of the G10 frame to solder the tungsten wires. Conducting paths of copper were traced from the pads to soldering flashes. Wire leads then transferred the current to the electrical feedthroughs and out of the monitor. Marked on the copper plated boards were centering marks for the 87 mm beam aperture and the four mounting holes, providing reference points for drilling. Other G10 boards for the split plates and high voltage planes were also created using this method.

The printed circuit boards were generated on the Gerber AutoCAD system which was operated by the TRIUMF wire chamber shop. Artwork generated on this system was saved on an 8 inch double sided, double density floppy disk with a limit of one job per disk. After the artwork was completed, the computer file was passed to a Hewlett Packard 8060 pen plotter. The pen used was a 0.7 mm tungsten 63TB plotter pen tip, the dimension of which must be taken into account when generating the circuit board artwork to scale. The plotter was instructed to draw the circuit at double size on a vellum sheet, a semi-transparent paper with a plastic like texture. The vellum sheet was then sent off site to a laboratory which reduced the plot to

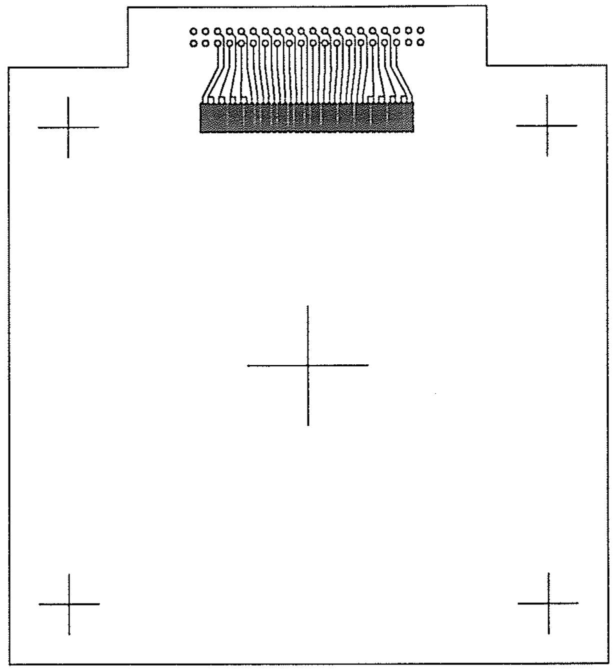

Figure 10: *Circuit board layout for the foil strips.*

scale and produced its negative print on a transparency. The artwork detail of the plotter was improved by enlarging the scale of the plot and then reducing it back to its original scale for the transparency, reducing the plotter imperfections in the final transparency.

The next step is to coat the copper plating with a photo-resist material. Photo-resists were available in positive and negative solutions as well as a negative laminate. The negative solution was tried but could not reproduce the detail of the laminate. The G10 boards were fed through the Kepro BTL-121 dry film laminator which heated the photo-resist film laminate to $300°C$ and applied it to the copper surface. The transparency was then placed over the photo-resist and exposed to a high intensity light such as an arc lamp with an exposure time of 7 minutes. Care was taken to ensure the printed side of the transparency was against the photo-resist material as this helped improve the definition and detail of the artwork. The photo-resist was cured by exposure to high intensity light and was developed in a sodium carbonate solution for two minutes. Areas of the photo-resist that were protected from the high intensity light by the negative transparency print were removed, exposing the copper plating. This dry film laminate was very resilient to damage at this stage and it was found that by using a small paint brush to brush between pads and tracks, better detail was obtained.

The copper plated board, complete with the printed circuit marked on its surface in photo-resist, was then immersed in a solution of ferric chloride (FeCl) which etched the copper from the exposed areas of the G10 board. Any copper which was protected by the photo-resist was left intact. The etching process took approximately fifteen minutes as etching for longer lengths of time allowed the FeCl solution to penetrate under the photo-resist material, causing breaks in the electrical tracks. Once the etching was complete, the G10 board was placed in a potassium hydroxide stripper solution which removed the remaining photo-resist, leaving the copper print underneath. The boards were then cut out and holes drilled for the beam aperture, mounting holes and wire flashes for lead connectors.

The final preparation of the G10 circuit boards was the mounting of foils and wires. The foil used was 8.5 μm thick aluminum which was easily available from local suppliers. With a total of ten foils per monitor, the total material placed in the beam by each monitor was 85 μm Al. Since then, another supplier has been located that was able to provide 5 μm thick foil, but this was acquired too late for the prototype monitor. These thinner foils will be used in the final version of the monitor, reducing the total material per monitor placed in the beam to 50 μm Al.

A multiple scattering calculation can be performed to compare the amount of mass placed in the beam by the SEM monitor as compared with previously existing gas filled monitors. The Split Plate Ionization Chamber (SPIC) used for the 800 MeV LAMPF experiment places 865 μm of aluminum in the beam (we will neglect the gas). The "rms scattering angle" of particles deflected by multiple scattering (in radians) is given by the equation [27]

$$\theta_o = \frac{14.1\frac{\mathrm{MeV}}{\mathrm{c}}}{p\beta} Z_{inc}\sqrt{\frac{L}{L_{Rad}}}\left\{1 + \frac{1}{9}\log_{10}\left(\frac{L}{L_R}\right)\right\} \tag{51}$$

where p, β and Z_{inc} are the momentum, velocity and charge of the incident particle, L is the thickness of material traversed, and L_R is the radiation length of the medium. For 230 MeV protons, p = 696 MeV/c, β = 0.6, Z_{inc} = 1 and the radiation length for aluminum is L_R = 89 mm. For the SEM monitor, θ_o(SEM) = 0.7 mradians while for the SPIC, θ_o(SPIC) = 2.6 mradians. If the monitor is located 2.0 m upstream of the target and a pencil beam is assumed incident on the monitor, then the standard deviation of the beam distribution at the target will increase to 1.4 mm for the SEM monitor and 5.2 mm for the SPIC. This demonstrates the improvement of the SEM monitor over conventional monitors as a low mass beam monitoring device.

The high voltage planes were the easiest to mount, using the vacuum foil stretcher shown in fig. 11. This stretcher consisted of an aluminum frame with a circular vacuum channel. Once the circumference of the foil was taped down to the aluminum frame, pumping on the channel sucked the foil into the channel and stretched the central region of the foil. Using two part epoxy, the foil was then secured to the G10 high voltage planes.

An alternate method mounting each side of the split plate separately was required for the signal foils. Supporting the foil on a clean glass plate, the

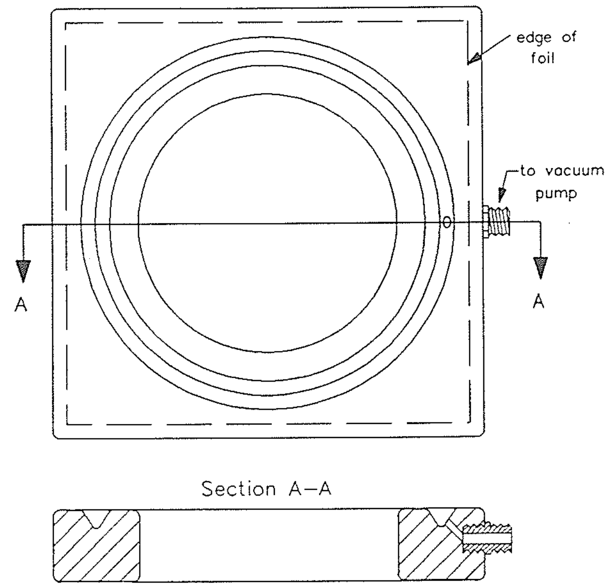

Figure 11: *Aluminum foil stretcher for high voltage planes.*

first split plate was cut with an Exacto blade and a straight edge. By lubricating the top foil surface with isopropyl alcohol and using a Kimwipe to gently stroke the foil outward from the center, wrinkles in the foil as well as any slack areas were stretched out. The surface tension of the fluid around the perimeter of the foil kept the foil tight to the glass while the G10 frame was lowered in place. Again, two part epoxy was used to secure the foil. Repeating this process for the second split plate completed the operation.

The last G10 frames which had to be mounted were the wire harp/foil strip frames. The wires used were 12 μm gold plated tungsten wires and the strips used were 0.90 mm wide, 0.008 mm thick aluminum foil strips. The channel spacing used was to provide signal readout at a separation of 1.00 mm for the central region. For the foil strips used in the low-gain SEM mode, it was decided that twenty one channels covering the central 21 mm of the monitor would provide ample coverage of the proton beam spot. The next

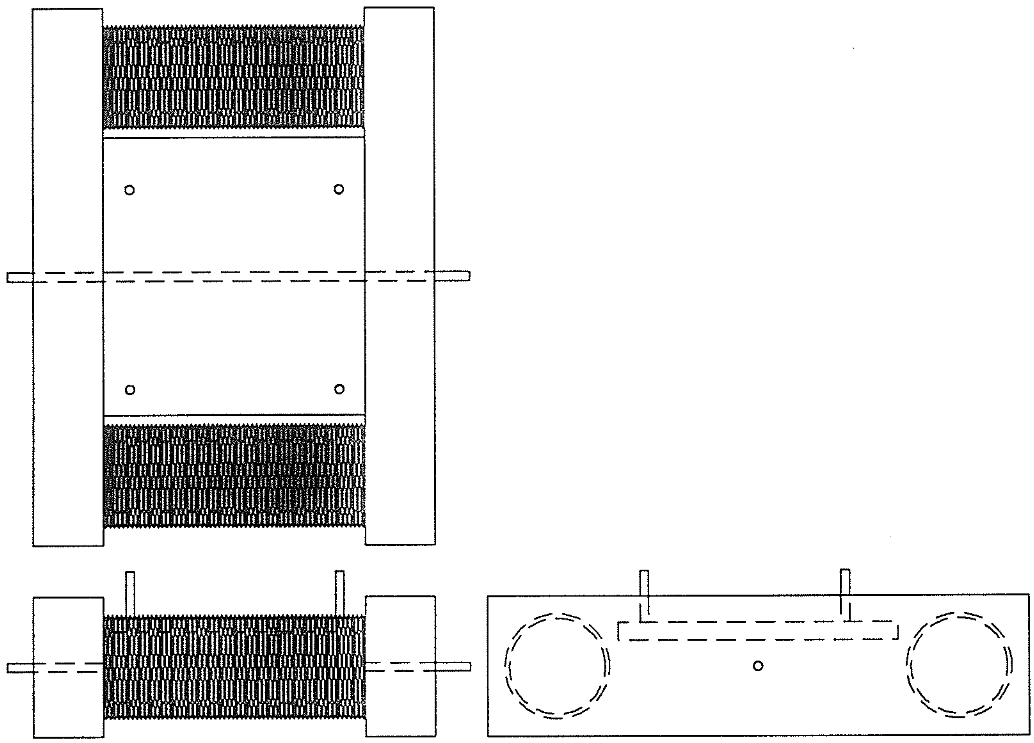

Figure 12: *The wire positioning and tensioning device.*

would be four double channels on either side of the central region. These double channels would include information on the tails of the profile for 8 mm on either side of the central region. Since the tails of the beam are lower in intensity than the central channels, the double channels would also be easier to detect with the electronics. Finally, the outer remaining regions of the monitor are combined in outer channels. These outer channels, numbers 1 and 31, contain the current from 19 mm to 47 mm from the center of the monitor.

For the mounting of the 12 μm tungsten wires, a typical wire mounting frame as shown in fig. 12 was used to secure the G10 frame. The wire was wound at a constant tension of an 80 gram weight around the threaded rods which have threads at 1.0 mm pitch. These threaded rods can be rotated allowing for transverse alignment of the wires with the G10 board soldering pads. Once aligned, the gold plated tungsten wires were soldered in place

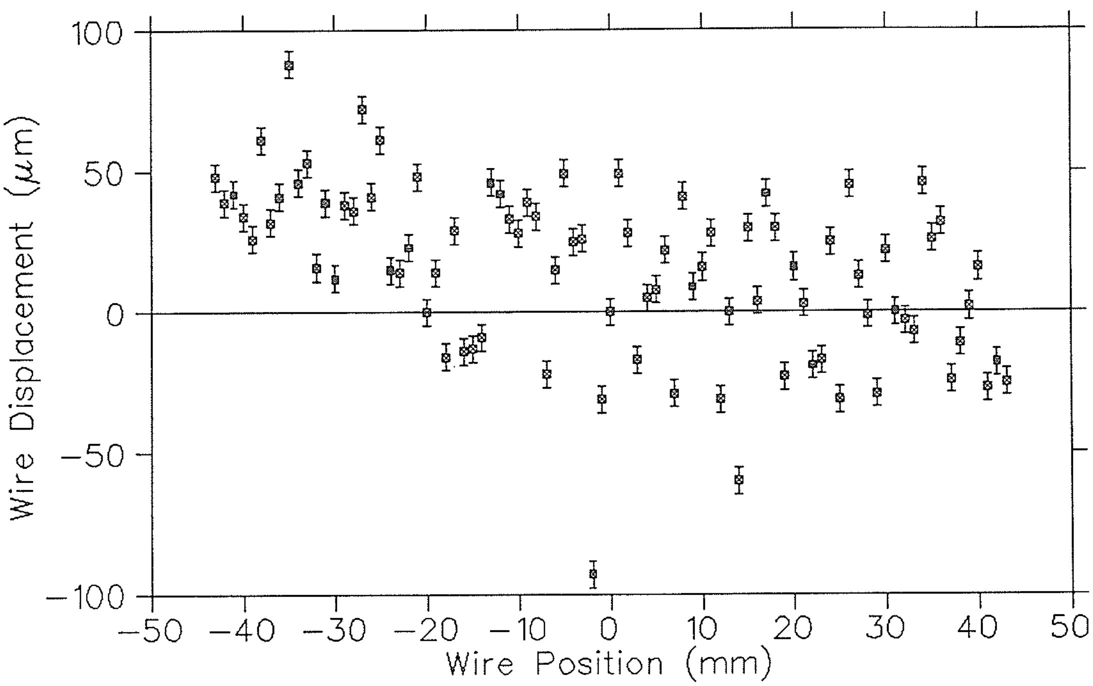

Figure 13: *Tungsten wire displacements after being mounted on the G10 support frame.*

and trimmed. This mounting procedure was capable of positioning the individual tungsten wires to ± 30 μm σ as shown in fig. 13. The plot shows the displacement of the wires from their optimum position. A displacement of 0 defines a perfectly placed wire. The error bars in the plot are the optical resolution of the projection microscope used to view the wires.

The alternate SEM mode of operation required that the gold plated tungsten wires be replaced by aluminum foil strips. The initial problem was to cut the foil into strips. The solution was provided through a collaboration with the Los Alamos National Laboratory. By focussing a Yttrium-Aluminum-Garnet (YAG) laser tuned to the 1.06 μm wavelength with a maximum 400 W output to a 0.1 mm beam spot, gaps were cut to a precision of ± 10 μm. The 15 cm × 15 cm aluminum foil was mounted in a frame while the pattern of single and double strips was programmed into the computer controlled positioning device of the laser. The cuts from the laser were not continued to the edge of the foil so that all strips could be mounted as one unit with the bordering foil trimmed after the strips were mounted. A gas stream was directed onto the cutting region so that as the laser vaporized the material, the gas stream removed the vaporized aluminum.

Once the aluminum strips had been cut, they were ready to be mounted. The major problem with the mounting of the array of strips was that as the laser cut each individual strip, the aluminum became hot and expanded. Due to inconsistent heating of the strips by the laser and the pressure from the gas jet that removes the vaporized aluminum, many strips became stretched and had to be tensioned more than others. After many attempts to mount the array of strips to a G10 board, each with proper tension to keep it from coming in contact with the neighbouring strips, the final technique was to begin by gluing one end of the strips to one side of the frame. The free end was then pulled tight and taped. Each individual strip was cut free of the foil, pulled taut by hand and finally glued into place while being viewed under a microscope. This process was long and tedious but proved to be the only method that was able to tension each strip effectively.

3.2 Split Plate Pack Motion Control Mechanism.

As mentioned in section 2, it was necessary to be able to relocate the position of the split plate pack assembly but not the profile pack assembly. Fig. 14 is the schematic showing the foil strip pack arrangement bolted directly to the rear face of the monitor. By viewing the beam profile on the wire harps or foil strips, the centroid of the beam was to be determined to within

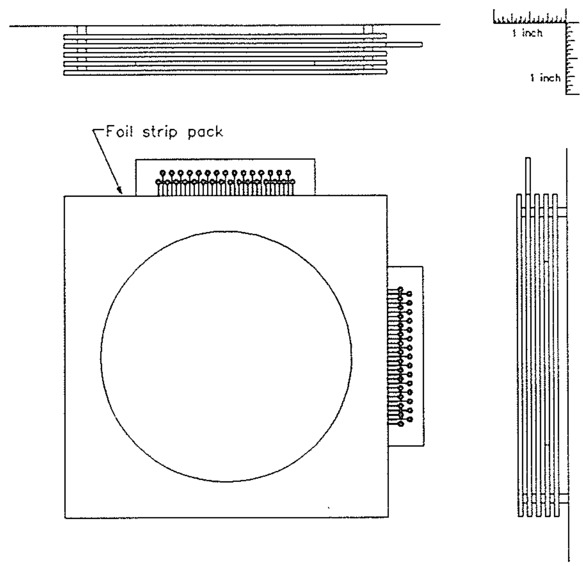

Figure 14: *Schematic of the mounting of the foil strip assembly.*

± 10 μm in one hour. The reproducibility of the motion control mechanism did not have to be to the ± 10 μm level but was to be comparable. Even though the final centroid of the beam was to be determined using the wire harp or foil strip pack, it was determined that a reproducibility of ± 13 μm was mechanically feasible and that many possible position readout devices were available.

Fig. 15 shows a schematic of the split plate motion control mechanism for the prototype SEM monitor. The basic design of the motion control mechanism was to place the split plate pack onto a frame which was supported on two vertical rails. The frames contain brass bushings that allowed smooth vertical motion on the stainless steel rails. The two vertical rails were then mounted on a frame fixed to two horizontal rails. Again, the entire system slides on brass bushings for the horizontal motion. Finally the horizontal rails were mounted in the aluminum cell. The maximum travel for both the vertical and horizontal motion is 10 mm, determined by the travel of the

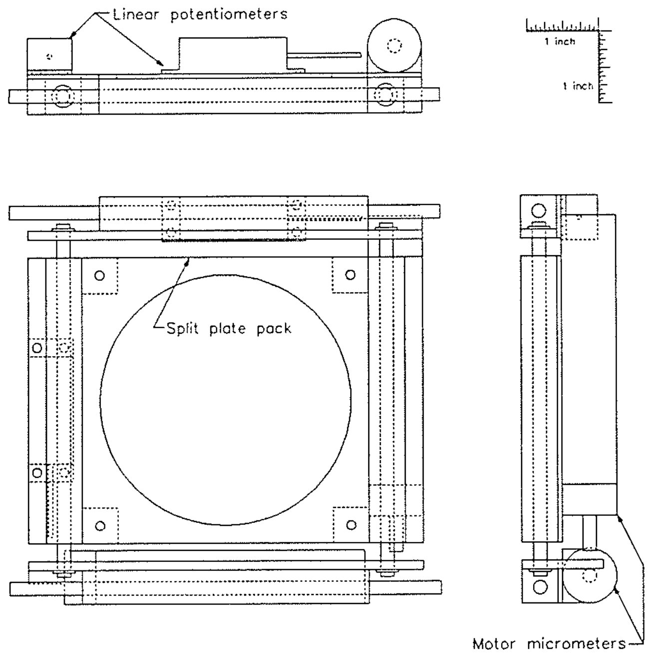

Figure 15: *Schematic of the X-Y motion control of the split plate assembly.*

stepping motors and the available space in the cell. Since the prototype monitor was used only for testing the various modes of operation, the 10 mm of travel was sufficient. The final version of the beam intensity profile monitor will require at least 50 mm of total travel, allowing more extensive testing of other parity beamline apparatus.

The position of the control mechanism is controlled by two motorized micrometers, the Oriel DC Encoder Mike Drives model no. 18212. These motors operate at a maximum speed of 12.5 mm per minute with a total distance of travel of 12.7 mm. Also available on the motor micrometer is an optical encoder which uses a shutter fixed to the motor shaft. Optical diodes mounted beside the motor are viewed with phototransistor detectors. The shutter has ten equally spaced apertures which interrupt the optical signal of the optical diodes ten times each revolution. With the motor micrometer geared such that one motor revolution equals 1.0 μm of travel, the highest resolution attainable from the encoder is 0.1 μm relative position. Unfortunately, this position readout proved unable to withstand the radiation flux experienced in beamline 4A. A separate position readout was therefore devised.

The most reliable position readout available was a linear potentiometer. Other options, including the optical encoders, proved inoperable under the radiation field of the beamline. Even the initial linear potentiometers proved susceptible to radiation. Testing of the resolution after the monitor was removed from the beam revealed that the reproducibility of these potentiometers had deteriorated. In an attempt to improve the monitor readout system, a second model of linear potentiometer was tried. This was the Beckman Instruments Series 400 Linear Actuation Potentiometer model no. 472-200-R5K-L25. This potentiometer had been used on other TRIUMF monitors and had proven its radiation hardness. Although the backlash from this potentiometer was of the order of 0.1 mm, approaching from one direction achieved the position reproducibility of $\pm$ 13 μm.

4 Monitor Electronics.

The two tasks performed by the Beam Intensity Profile Monitor were to supply asymmetry signals for the beam position servo loop and record the profile data used to determine the shape of the beam during the experiment. The fast feedback servo loop was used for real time corrections to the beam position through servo amplifiers and aircore steering magnets. The profile data were recorded on computer tape, then processed to calculate the beam centroid (which may vary from the split plate controlled median) and width. Eventually the profile monitor will be used in conjunction with the polarization profile monitors to determine moments of transverse polarization. Both of these systems are discussed in the following sections.

4.1 Position Control Servo Loop Electronics.

Once the split plate pack had been aligned on the desired beam axis, it was the job of the position control servo loop to prevent low frequency excursions of the beam centroid from this axis. The electronic signal was extracted from the split plates using secondary electron emission. The secondary electron yield from aluminum is ~ 5 % per proton, per surface; thus, for a 500 nA beam experiment, the total plate current for one monitor would be 50 nA. For a 500 nA beam centered on the monitor, the average current on each split plate would be approximately 25 nA. The four split plate signals (L,R,U,D) make up the two asymmetry signals, vertical and horizontal, for each monitor.

The four split plate current signals were passed to an operational amplifier which was mounted in an electronics rack next to the beamline. The

Split Plate Electronics (4 channels)

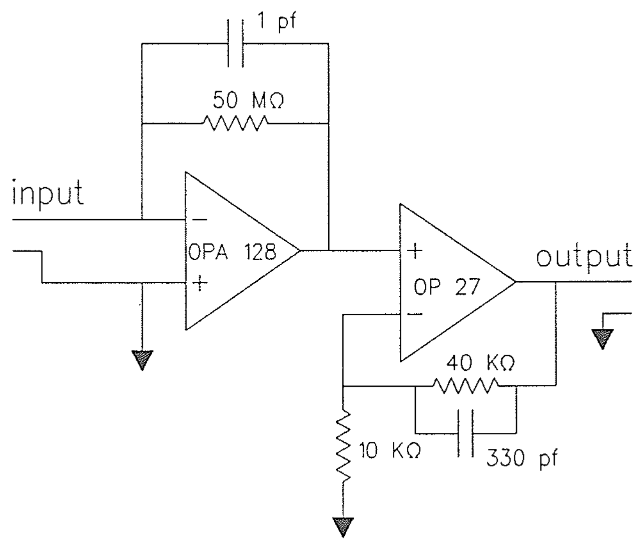

Figure 16: *Electronic circuit for the L,R,U and D split plate signals. The OPA 128 is an inexpensive, low noise, low input bias operational amplifier.*

proximity of the amplifiers was imperative to minimize noise pickup by the unamplified split plate current signals. The total distance before amplification was reduced to 0.5 m of cable. The operational amplifiers operated at a gain of 25 nA input current to 5 volts output voltage at a bandwidth of 5 kHz. The electronic circuit can be seen in fig. 16 with four channels per amplifier unit. Two units, one for each monitor, are required for the final parity violation experimental setup. Using the Burr-Brown Operational Amplifier OPA 128, a two stage gain, differential input, low noise, high amplification circuit was achieved. The advantage of the differential input was that noise from ground loops was greatly reduced. Amplified signal outputs were also made with differential connections, reducing the noise pickup of the cable. The amplified voltage signals travelled through balanced lines from the beamline to a nearby trailer housing the computer CAMAC branch. The total length of these differential cables was 30 m.

The four voltage signals of each intensity monitor entered the trailer and were fed into one of two single width NIM analog divider boxes, one for the vertical loop and one for the horizontal loop. These devices were designed and built at TRIUMF using the Analog Devices model no. AD538 analog divider chip. The divider module then provided the horizontal or vertical asymmetry signal as defined in eq. 26. A second output from the analog dividers was a logic signal (TTL). This output signal was set to 5 volts when the sum of the two split plate currents dropped below a preset threshold and was set to zero under normal operating conditions.

The two voltage output signals from the analog dividers were then passed to the variable gain servo amplifier which had a $\frac{1}{f}$ fall off of voltage gain with frequency (6 db/octave). The high frequency fall off was necessary to keep the open loop gain below unity at the higher frequencies where the phase shift of the loop becomes greater than $\frac{\pi}{2}$ and the feedback loop becomes destructive. This unit, which was typically operated at a gain of 1000, was used to control the power supplies which drive the steering magnets, minimizing the position asymmetry signal produced by the monitor. Since changes in beam shape and size can create a change in the loop response, a variable gain control was necessary. The variable gain servo amplifier also contained an inhibit input which received the TTL level from the analog divider. This disabled the loop until the beam current returned to an acceptable level. The logic signal was used to disable the servo loop under conditions when the beam current was too low to prevent instabilities in the loop performance.

After the asymmetry voltage signal from the analog dividers had been amplified in the servo loop amplifier, it was then sent back to the beamline area where it was connected to the power supplies of the aircore steering magnets. These power supplies received the amplified asymmetry signal and supplied a high current output using the APEX model PA 03 high current operational amplifier, capable of output currents up to 30 amperes. By applying a current of 20 amperes to the steering magnets, a total deflection of 0.8 mradians is achieved for the 230 MeV proton beam. If the asymmetry signal received was for a positive displacement, the correction was applied in the negative direction so as to reduce the resultant asymmetry signal on the plates.

The strength of the correction applied by the steering magnets was controlled by the servo loop amplifier. By observing the asymmetry signal on an oscilloscope while increasing the gain of the servo amplifier, a reduction in the position displacement of the beam was observed. As the gain was increased above its optimum value, the loop became unstable, eventually breaking into oscillation. The optimum gain setting was a compromise between large residual beam motion at low gain and instability at high gain. The optimum gain setting was typically about half of the value that caused oscillations.

The fast feedback servo loop can be implemented in either a coupled or decoupled mode. Fig. 17 shows the schematic for passing asymmetry signals to the respective steering supplies. In plot A), the first split plate (SP1) asymmetry is passed directly to the first aircore steering magnet (ACSM1) and the second split plate (SP2) asymmetry is passed directly to the second aircore steering magnet (ACSM2). Note that to properly define the beam axis from SP1 and SP2, no external steering to the beam can be applied after passing SP1. Since the second aircore steering magnet was located close to SP1, any steering done at ACSM2 would have a negligible effect on SP1, and the steering corrections performed at ACSM2 would not be imposed on the upstream loop. Unfortunately, the same is not true on SP2 for corrections performed at ACSM1. If a correction is applied at ACSM1, the beam deflec-

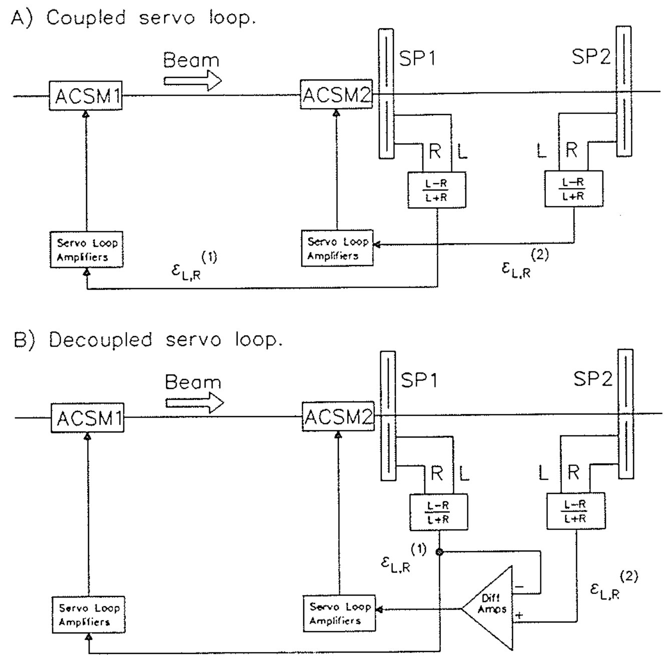

Figure 17: *Schematic for the horizontal component of the A) coupled feedback servo loop, B) the decoupled feedback servo loop.*

tion at SP2 will be approximately double the deflection at SP1, and ACSM2 must then compensate for the correction of ACSM1. Experience from previous experiments shows that this mode of operation will work effectively if both aircore steering magnets are operating within their optimum range of power.

In an attempt to reduce the effect of one steering magnet trying to correct for the other, a decoupled mode can be implemented. As shown in plot B) of fig. 17, use is made of a difference amplifier. The first loop remains as it was in the previous mode, feeding the SP1 asymmetry signal directly to ACSM1. For the second loop, both the SP1 and SP2 asymmetry signals are passed to a difference amplifier. A gain adjustment on one of the input channels allows the relative strengths of the two asymmetry signals to be controlled. The result is that the correction made by ACSM2 is reduced depending on the correction made by ACSM1. This may seem destructive at first, but it is important to note that the "lever arm" effect of ACSM1 on SP2 is twice as large as that of ACSM2 on SP2. In this mode, the work done by ACSM1 will influence ACSM2 less, providing two relatively independently operating servo loops. Regardless of the mode adopted, the frequency response of the two servo loops should also be kept different since this suppresses the possibility of the two loops being forced into oscillation while trying to correct for one another. A detailed test of the two operation modes will be performed once both dedicated monitors are constructed and implemented.

4.2 Profile Monitor Electronics.

The profile information was extracted from wire harps and foil strips. Each harp contained 31 channels, and the final experimental setup requires four such harps. Two options were considered for the 31 channel electronics. The first was to feed all of the harp currents to a single operational amplifier by using a Complementary Metal Oxide Semi-conductor (CMOS) switch, a high impedance switch capable of low current operation. The benefit of using this type of electronic setup was that the electronic gain for all channels would be the same. Gain calibration would still have to be performed to take into account the variations in surface area from one strip to the other (estimated to be less than 5 %) as well as any differences in the foils' secondary electron efficiency. Another advantage with this setup was that the cost was extremely low. However, experience with these CMOS switches had revealed that charge injection during switching would exceed the current expected from the secondary electron yield of the proton beam. For this reason and because the cost of the operational amplifier was reasonable, each channel was provided with its own electronics.

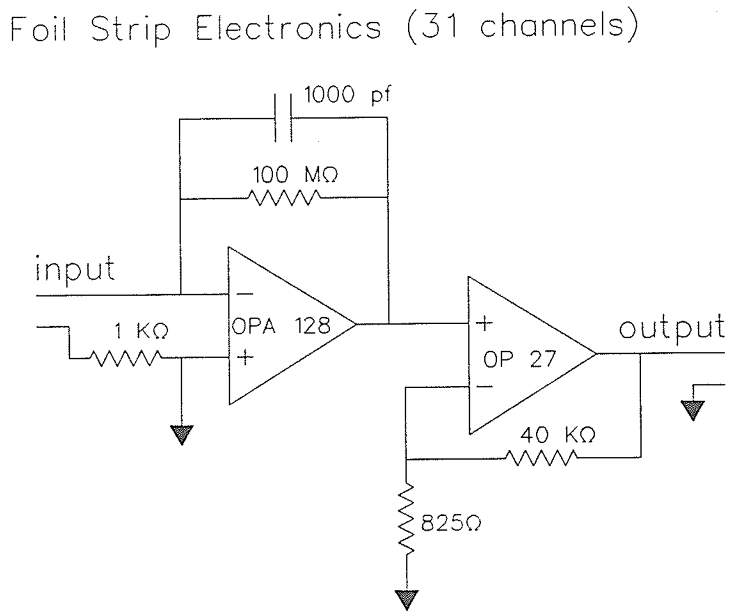

Figure 18: *Electronic circuit for the 31 channel wire harp or foil strip preamplifier case.*

The 31 channel preamplifier case contained the entire electronics for a single wire harp or foil strip plane. As with the split plate unamplified signals, it was important to place the preamplifier as close to the monitor as possible. The distance travelled by the unamplified current signals was reduced to approximately 0.5 m. The signal circuit used for the prototype monitor foil strips is shown in fig. 18, providing a gain of 1 nA input current to 5 volts output voltage and operating at a bandwidth of 2.5 Hz. Note that this bandwidth translates into an integration time of 0.5 seconds. Although the requirements were specified for an integration time of 1 second, integration through the use of electronics does not provide a definite start and end of the integration. For the prototype monitor tests, the 31 channel preamplifier differential output signals were passed to a CAMAC ADC, the LeCROY module 2232A. This module was capable of sampling 32 differential input channels sequentially, taking 18 msec for an entire scan. Since the monitor was located 30 meters from the CAMAC crate, differential cables were used for the voltage lines from the preamplifier to the CAMAC module.

The computer used for the prototype monitor tests was a microVAX which is currently used in conjunction with the TRIUMF Medium Resolution Spectrometer. By extending the computer branch parallel highway to the trailer containing the parity electronics, computer control of the data acquisition modules was available. The final monitor setup will incorporate a 32 channel voltage to frequency converter using the Analog Devices model ADVFC 32 which is capable of operating up to 500 kHz. The LeCROY ADC module will be replaced by a LeCROY 4434 32 channel, 24 bit Emitter Coupled Logic (ECL) scaler capable of counting at 20 MHz. This setup will allow user control of the integration time of the channel currents. This is an important feature since the experiment requires an accurate start and end to the integration time, not possible with the conventional integrating ADC for the long (up to one second) integration time required for that device.

5 Monitor Performance.

A number of test runs were scheduled to test the beam intensity profile monitor. Since other elements of the parity apparatus were also under construction, a mock setup of the beamline was used. For the prototype monitor tests, the beamline 4A setup was assembled with an aircore steering magnet, a SEM halo monitor, a transverse field ion chamber borrowed from Los Alamos and finally the beam intensity profile monitor. The total distance from the steering magnet to the profile monitor split plates was 3.45 meters.

5.1 Wire Harp Operation.

One of the basic operational modes of a beam intensity profile monitor is to collect the ion pairs created as the beam particles pass through the detection gas. The first test for the wire harps was performed in a February 1989 test run where the current plateau of the monitor was investigated. The monitor setup used for these runs is shown in fig. 6. A wire spacing of 1.0 mm was used and the gap from the wire harp to high voltage foil was set to 3.0 mm by placing spacers between the G10 boards.

With 130 nA beam current, the wire harp signal current for channel 12 was determined for various applied potentials to the high voltage foils. Fig. 19 shows the plateau of the monitor for the negative and positive polarities of the high voltage foil. The upper plot, which is labelled negative, is the result of collecting electrons on the wires. Likewise, the positive polarity plot refers to the case where positive ions are attracted to the wires. The gas was H_2 and the pressure of the gas was 80 torr ($\sim 1/10$ atm).

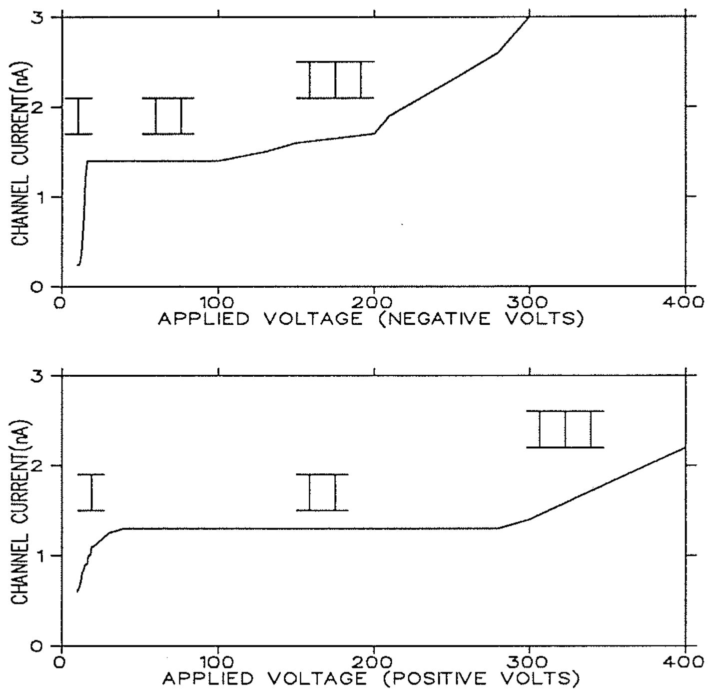

Figure 19: *The effect of reversing the applied high voltage polarity on the signal current of channel 12. Region I designates recombination, region II is the current plateau used for monitor operation and region III refers to avalanche multiplication (upper plot) or cold electron emission (lower plot). Beam current: 130 nA,* H_2 *pressure: 80 torr.*

Each plot can be divided into three regions with both polarities providing a definite operating plateau of a few hundred volts. As the beam particles pass through the detection gas creating ion pairs, either the electrons or positive ions are attracted to the tungsten wires. Region I refers to the range of high voltage where the ion pairs could recombine before they were completely collected. Notice that the plateau for the negative applied voltage was reached much sooner than for the positive applied voltage. This has to do with the fact that the electrons have a higher mobility in the hydrogen gas than do the positive ions. When collecting electrons on the wires, they create a relatively small region of high density ions. Because of their lower mobility, the collection of positive ions will create a much larger region of high density ions. This in turn shields the potential of the wire and enhances the effect. The result is that as protons from the beam continue to generate ion pairs in this region, there is a greater probability of recombination while collecting the positive ions on the wires. Thus, recombination is reduced more quickly for the case of negative applied high voltage.

Region II refers to the plateau where the current signal from the monitor is independent of the applied voltage. The width of this plateau is approximately 100 volts for negative applied high voltage and approximately 200 volts for positive high voltage. The extended length of the positive high voltage plateau is a result of region III. One observes the onset of avalanche multiplication for the negative applied high voltage and cold electron emission for the positive applied high voltage. The critical reduced field for the onset of avalanche multiplication as discussed in section 2.1.1 was 30 $\times P$ V cm^{-1} mm Hg^{-1}. Once the reduced field surrounding the wire is larger than this critical value, electrons accelerated in this field have enough energy to ionize the H_2 gas molecules. Even if this critical field is only one electron path length deep, the result is that the detected electron current would be doubled.

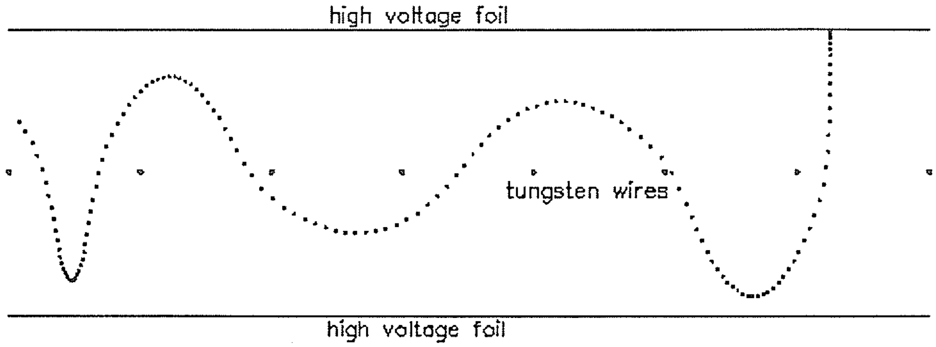

Figure 20: *The trajectory of an electron, in a vacuum, emitted from a high voltage foil.*

For the positive applied high voltage case, electrons are collected on the high voltage foils. Only a very small number of these electrons encounter the high field region surrounding the wires. Because of the positive ions' larger mass, their critical reduced field value for avalanche multiplication is many times larger. In fact, long before this value is reached, the high field on the surface of the wire is strong enough to strip electrons from the surface atoms of the wire and hence, cold emission occurs.

As one can see, there are a number of non linear effects which limit an ionization type intensity profile monitor. In an attempt to make use of the linearity of secondary electron emission, the wire harp setup was operated in a secondary electron mode with a high vacuum. First consider the case where electrons from the high voltage foils are collected on the tungsten wires. The electric field around the wire can be approximated from eq. 6 such that

$$E(x,y) \cong \frac{CV_o}{2\pi\epsilon_o}\frac{1}{(x^2+y^2)^{\frac{1}{2}}} \tag{52}$$

where the parameters have the same values as in eq. 6. Notice that this is a $\frac{1}{r}$ field which results in an elliptical orbit for the electron. In a gas ionization device, this is not a problem since electrons that are accelerated towards the wires can also collide with the other gas molecules in the sense region. The electrons lose energy in these collisions and eventually fall onto the collection wire. In a vacuum, the electrons cannot lose angular momentum and as a result, they orbit the wires. A simple program that used the analytic expression for the electric field generated the trajectory of an electron in a vacuum, leaving the aluminum foil with only a few electron volts, as shown in fig. 20. Points on the trajectory are spaced by 10 ps. The electron is seen to travel a number of wires before it is eventually collected, far from its point of origin. The result would be a smearing of the profile over the entire monitor. To verify these results, the monitor was placed under a turbo pump vacuum of 10^{-6} torr and a profile was taken during a June 1989 test run at a beam current of 270 nA. This spectrum was taken with only 16 channel preamplifiers available, thus only the central 16 channels are shown in fig. 21.

Another test for the wire harp was an attempt to eliminate the smearing effect of the electrons. The proposed method was to weave 8 μm thick kapton foil between the wires. The assumption was that the insulator would accumulate charge and repel the electrons. The electrons would charge the insulator until repulsion was great enough to deflect the electrons into the wires. Fig. 22 shows the positioning of the kapton foil in the wire harp and the observed distribution. The monitor was operating under a turbo pump vacuum of 10^{-6} torr and secondary electrons were collected on the wires. Unfortunately, the run was not recorded on computer tape and the vertical current scale is not known. The profile distribution alternates in intensity from odd and even channel numbers. Although this effect has not been studied in great detail, the effect was assumed to result from the fact that the kapton divides the wires such that every other wire was facing either the upstream or downstream face of a high voltage foil. It is well known [28] that

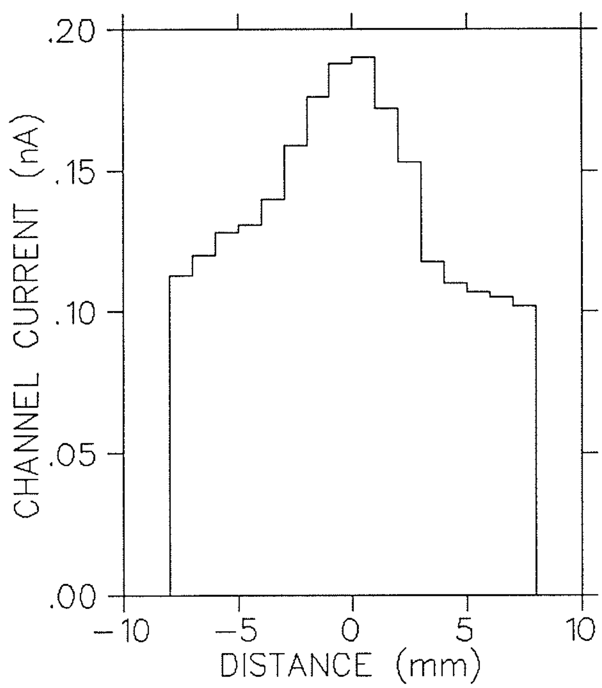

Figure 21: *The observed spectrum of emitting electrons from the high voltage foils and collected in a vacuum on the tungsten wires. Beam current is 270 nA. Horizontal scale is centered on the central wire.*

the upstream and downstream faces of a foil will have different secondary electron yields. The difficulty in extracting the true profile from this method of operation had rendered this option useless.

The final test for the tungsten wire setup was to reverse the polarity of the monitor while under a hard vacuum and observe the emission of secondary electrons from the tungsten wires. Again, the previous monitor parameters were used and the results can be seen in fig. 23. This test was also performed with only 16 preamplifier channels; therefore, only the central 16 channels are shown. Note that the maximum channel signal was only about 60 pA, a very small detector signal that would drastically reduce the signal to noise ratio. This method also proved unacceptable.

5.2 Split Plate and Foil Strip Operation.

When operating the monitor in secondary electron emission mode, the value of the applied voltage becomes less critical. The only criterion for the maximum high voltage would be breakdown or the onset of detectable leakage currents. An applied high voltage of 300 volts was used for the prototype monitor in this mode. It was necessary that operation of the monitor in the secondary electron emission mode be conducted in a vacuum. A calculation of the current contribution of ion pairs in the detection gas has been made in section 2.1.1. Results were that the 230 MeV protons will produce 18.1 ion pairs per proton, per centimeter of H_2 gas at atmospheric pressure. At 1 torr, this reduces to 0.02 which is comparable to the secondary electron yield of 0.045 per proton, per surface of aluminum foil. The gas pressure should be kept well below the mtorr region to ensure the charge collected is only secondary electron current. The pressure in the monitor box volume

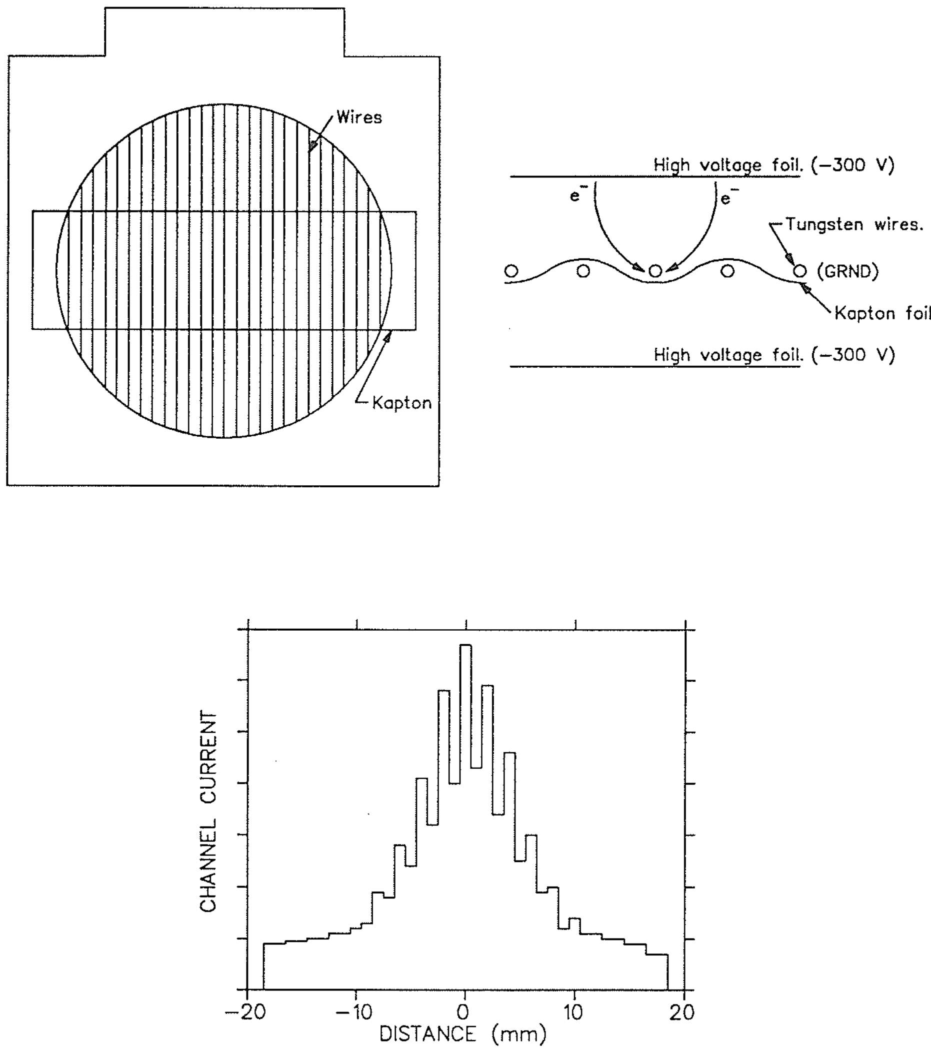

Figure 22: *The schematic showing the placement of 8 μm kapton foil in the wire harp plane with the corresponding current distribution. Current scale is not known.*

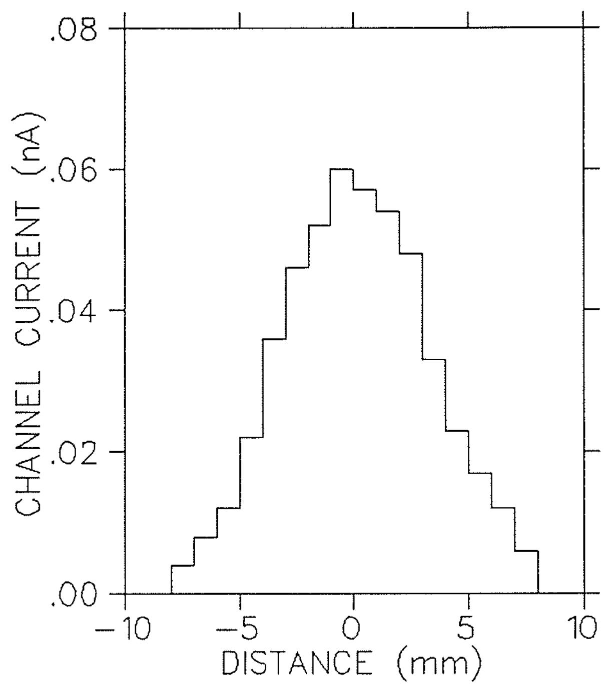

Figure 23: *The observed spectrum of emitting electrons from the tungsten wires and collected on the high voltage foils. Beam current is 270 nA.*

was monitored with a remote vacuum gauge to ensure that the gas pressure remained below the critical value. What happens if the pressure rises above the critical value? The first reaction might be to return the pressure to the optimum value and continue the monitor operation, but a temporary increase in the pressure has proved disastrous to future monitor performance.

Operation of the monitor in a number of separate test runs has led to a detectable change in the surface efficiency of the aluminum foil. Possible causes of this effect can be classified into two basic categories. The first is a change in the structure of the aluminum surface and the second is the deposit of ion contaminants on the foil. Since the SEM process is a surface effect, increasing the surface area of the aluminum foil increases the yield of secondary electrons. If so desired, this can be achieved by sputtering or even etching of the aluminum to create an irregular foil surface.

The effect of depositing dielectric material on the surface of aluminum foil was studied by Chehab et al [29]. By depositing CsI onto an aluminum foil, secondary electron yields for a 25 MeV electron have been observed close to 4.0 which is an increase by a factor of 10 over aluminum oxide. It is also well known that polyatomic organic gas in the detection region results in a buildup of liquid or solid polymers on foil surfaces [22]. The process is known as polymerization and is observable for beam fluxes above 10^7 to 10^8 particles sec^{-1} cm^{-2}. The beam particles generate radicals which can recombine to form smaller molecules (dissociation) or larger molecules (polymerization). This is the basis of "quenching", a process used in proportional counters to modify the high gain operation stability of the detector gas by adding small amounts of polyatomic molecules. The radicals may polymerize into larger molecules which are then deposited on the anode or cathode surfaces of the monitor, depending on their affinity. The result is a thin film of polymers on the aluminum foil which alters the secondary electron yield.

The largest change in SEM efficiency was detected for areas of the monitor operating in the most intense beam. The outer protons of the sense region were less affected. This non-uniform increase in SEM yield was observed with the vacuum operation of the prototype monitor. The first observation of the change in SEM efficiency was made during a gain calibration run. The run is discussed in greater detail in section 6, but the essential feature is that the beam was positioned in three different locations along the horizontal with a shift applied to the beam centroid of approximately 1.0 mm. By averaging a number of events, the three profiles taken should be expected to average out any changes in the intensity of the beam. However, the profile located at the center of the monitor showed a systematic increase of total beam current of about 1 %. This position dependence was also observed for the halo monitor, the second SEM device in the prototype beamline setup. The beam position at this monitor was moved by approximately 10 mm, and the total change in efficiency was observed to be about 10 %.

A second observation was more direct in determining the change of efficiency of the contaminated foil. For diagnostic purposes, a solid Al foil was inserted after the array of foil strips. This normalization foil was to detect the entire beam current incident on the prototype beam intensity profile monitor. Since this foil was immediately downstream of the array of aluminum foil strips, the current of the two should be comparable. Note that since the strips contain gaps of about 10 % of their width, the integrated beam current over the strips should be $\sim$ 90 % of the normalization foil. The current on the foil strips (which had been in the beam for a number of test runs) was compared to that of a newly installed normalization foil (of identical stock material) for a test run performed in June 1990, and found to be equal to within 1 %. After the normalization foil had been left in the beam for two days, a second comparison revealed the 10 % difference expected. The two days of beam exposure had led to an increase in the foil efficiency as experienced with the halo monitor as mentioned above. Longer exposure of the normalization foil failed to produce any further changes in the efficiency. Many of the test runs have resulted in extended operation under non-ideal vacuum conditions, the result of numerous turbo pump failures in which the pressure in the monitor rose to the roughing pump backing pressure. This level was found to be 10-50 mtorr, high enough to permit polymer contamination of the foils. The final beam intensity monitor must be kept clean for the duration of the parity violation experiment. This will require an operating pressure of at most 10^{-6} torr in the monitor and separation of the monitor vacuum from the beamline vacuum.

5.2.1 Split Plate Performance.

The final parity violation experimental setup requires two split plate monitors separated by at least 2 meters. As noted previously, the steering magnets are based on the aircore design and the option is available to replace these aircore steering magnets with ferrite core magnets. The use of two split plates defines the beam position at two locations, and the x-y motion control of the split plates allows the positioning of the beam axis as defined by the monitors. This feature provides a means of testing the position sensitivity of other experimental apparatus as well as being able to locate the optimum axis for the experiment. The positioning accuracy of the split plate control mechanism was determined by placing the monitor in a support frame. A reference mark was placed on the split plate pack. At three meters from the support frame was an optical telescope which was focused on the reference

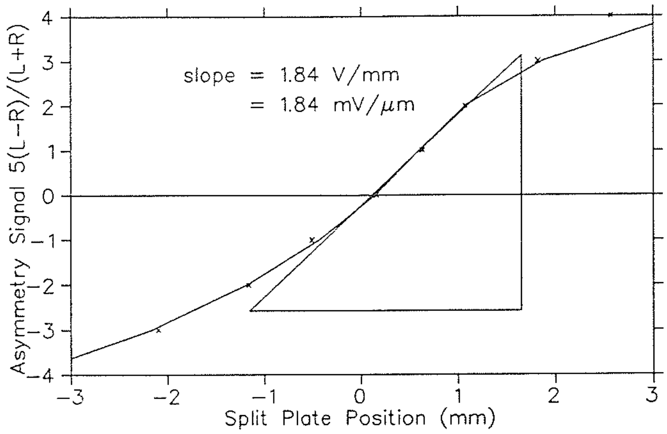

Figure 24: *Asymmetry signal as a function of split plate position.*

point. By moving the split plates a predetermined distance and referring to the readout system, the calibration of the motion control mechanism was determined. The motion control mechanism was moved off to one side, then returned to the original position and the potentiometer readout was recorded. The variation in the linear potentiometer readout for a number of trials was of the order of $\pm$ 13 μm. This value was of the order of the resolution of the optical bench setup, so the true accuracy of the split plate control mechanism should be better than the observed $\pm$ 13 μm.

The final test for the split plate operation was of the servo loop performance by passing the split plate asymmetry signal to a Fast Fourier Transform analyzer. Since the split plate asymmetry signal was to be used as a measure of beam displacement, it was necessary to determine its calibration. Note that this calibration depends on the beam spot size and must be determined for each beam profile. By moving the split plates across the beam and determining the position and asymmetry signal, a plot of split plate asymmetry versus position was created and is shown in fig. 24. The slope of this plot at the beam center gave a calibration of 1 mV to 1.84 μm.

With the above calibration, the asymmetry signal transmitted to the FFT analyzer was interpreted as a position displacement. Fig. 25 shows the asymmetry signal converted to beam position displacement for the servo loop on and off. The Fourier transform is shown in the lower plot in fig. 25. The reduction of beam displacement when the loop is on was a factor of approximately 100. The bandwidth of the analyzer was set to 10 Hz for these plots. From the figure, it is seen that the beam fluctuates by up to 100 μm but by employing the loop, the beam displacement is reduced to less than 5 μm.

To observe the servo loop performance on a shorter time scale, the bandwidth of the FFT was set to 200 Hz. A second time sweep is shown in the upper plot of fig. 26. The increased bandwidth shows a much less controlled beam position. The lower plot of the figure again displays the Fourier transform of the beam displacement. In this figure, the higher frequency fall off of the servo loop electronics is evident. As the beam position fluctuates at higher frequencies, the servo loop becomes less effective. As the frequency of the fluctuations reaches that of the limiting response for the servo loop, the loop becomes destructive, thus the reason for the high frequency falloff of the servo loop electronics.

As a final note, it was observed that the split plate signal was very susceptible to vibrations of the monitor. This is expected, since the split plate monitor is also a parallel plate capacitor. During bench tests of the monitor, vibrations were shown to cause a capacitive coupling between the high voltage foils and the split plates. This problem was also observed on the foil strips which are discussed in the following section. In order to reduce the vibrational coupling, the split plate pack as well as the foil strip pack were mounted on their supports with rubber grommets. This mounting scheme holds the plate packs in place while eliminating the hard mechanical con-

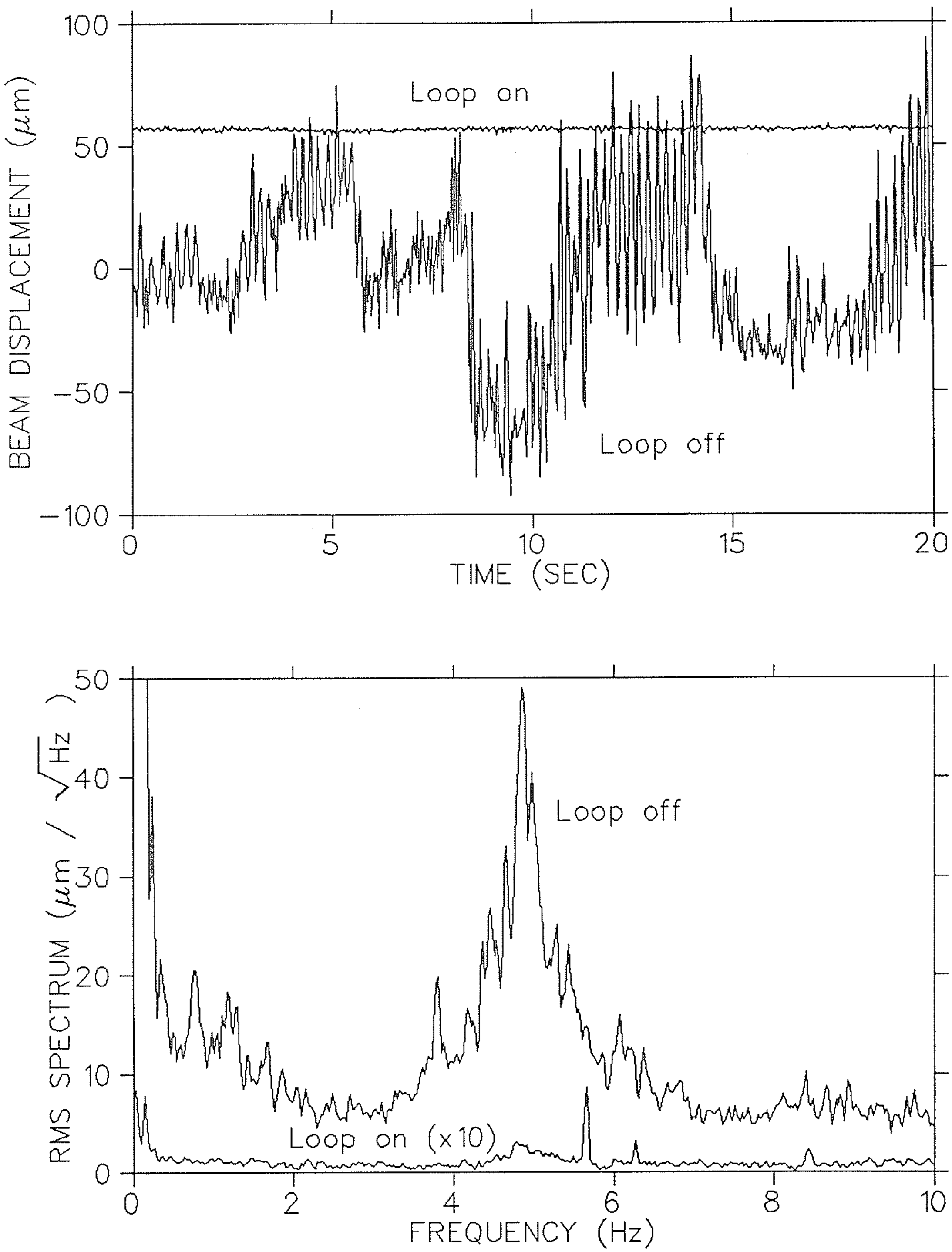

Figure 25: *Upper plot: Beam position control for servo loop on and off in the time domain. Lower plot: Beam position control for servo loop on and off in the frequency domain. FFT bandwidth is set to 10 Hz.*

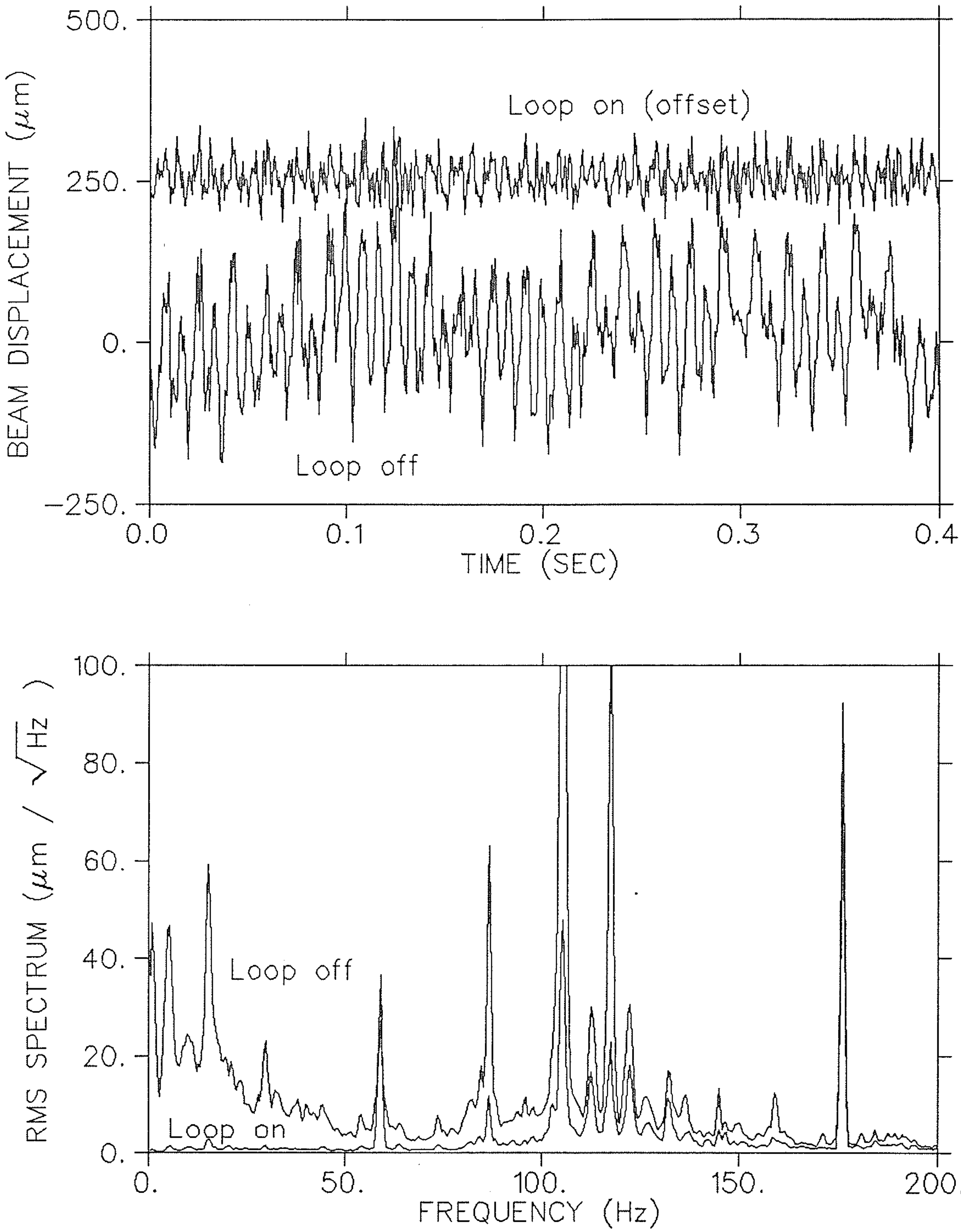

Figure 26: *Upper plot: Beam position control for servo loop on and off in the time domain. Lower plot: Beam position control for servo loop on and off in the frequency domain. FFT bandwidth is set to 200 Hz.*

nection to the monitor box. A second step towards reducing this effect was taken when it was observed that most of the vibration was coming from the turbo pump vacuum station. By connecting the vacuum flanges via a flexible hose, the vibrations passed to the monitor were substantially reduced. Unfortunately, this flexible vacuum hose caused vacuum leaks and could not be used for pressures less than 10^{-6} torr. Once any vacuum leaks were located and the outgassing complete, the vacuum system would pump down to a reasonable level for operation. One possible solution is the use of an ion pump which does not vibrate and can still achieve a vacuum below 10^{-6} torr.

5.2.2 Foil Strip Performance.

The initial tests of electronic noise present on the foil strip array were determined without any beam. With the 32 channel preamplifier box located in the electronics trailer, the 32 unamplified signals travelled 100 feet along coaxial cables to the preamplifiers. Once the signals were amplified, they were passed to the 32 channel ADC and read out by computer. Fig. 27 plot A shows a histogram of foil strip channel 6 current with no beam. The electronic noise of this channel was 3 pA (σ). The 32 channel preamplifiers were then placed in the beam tunnel as close to the monitor feedthroughs as possible. The unamplified cable runs were thus shortened to 0.5 m. The amplified channel currents were then passed to the trailer. Fig. 27 also shows plot B, a histogram of foil strip channel 6 current under the same conditions but with the 32 channel preamplifiers located in the 4A beam tunnel. The reduction in noise is dramatic, being reduced to two ADC channels. In these plots using the 12 bit resolution ADC readout, one ADC step corresponds to 1/2048 nA or 0.488 pA.

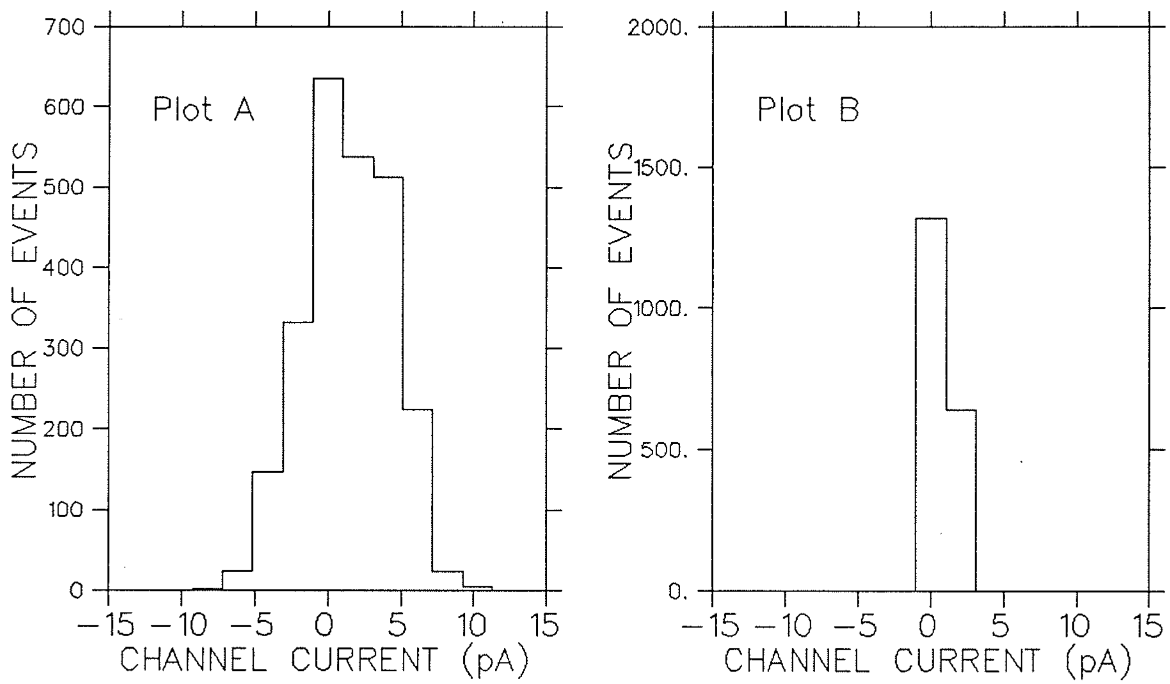

Figure 27: *Measurement of electronic noise. Plot A: Signal current histogram of channel 6 with preamplifiers located in the trailer. Plot B: Signal current histogram of channel 6 with preamplifiers located in the 4A tunnel. Plots generated with beam off.*

The above value for the noise of the preamplifier channels was consistent for all channels with the exception of the outer channels. The active region corresponding to these outer channels ranges from the end of the double strips at 19 mm to 43 mm from the center of the monitor. Because these outer strips have such a relatively large sense region, any residual vibrations in the monitor have greater capacitative coupling to these than to the narrow strips.

Once the noise of the 31 preamplifier channels had been reduced to a suitable level, the pedestal values of the preamplifiers were determined. Fig. 28 shows the 31 preamplifier channel pedestals taken during the December 1989 test run. The bandwidth of the electronics was set to 2.5 Hz, which operates as a 0.5 second time integration. A total of 1800 events, taken over 30 minutes, were recorded. Recall that the design specifications require that the pedestal values be known to $\pm$ 1 pA. Determination of the pedestal values can be made to $\pm$ 0.1 pA by performing a beam off data taking run for the appropriate length of time. Bench tests of the Detronics 41 pin electronic feedthrough used in the prototype beam intensity monitor also showed that the pedestals were greatly influenced by contaminants on this connector. Cleaning the insulator that separates the pins decreased the pedestals below $\pm$ 1.5 pA.

To determine the time evolution of these pedestal values, a single beam off run was taken for 2.5 hours. The events were then divided into 5 separate, sequential runs of 30 minutes. In fig. 29, the evolution of the pedestal values of the 31 preamplifier channels is displayed. Each channel number on the plot contains the pedestal value from each of the 5 sequential runs. The first pedestal value is plotted at the channel number, but subsequent pedestal values are offset. For example, channel number 10 reads about 0.5 pA pedestal for the first run, plotted at channel number 10.0. The pedestal

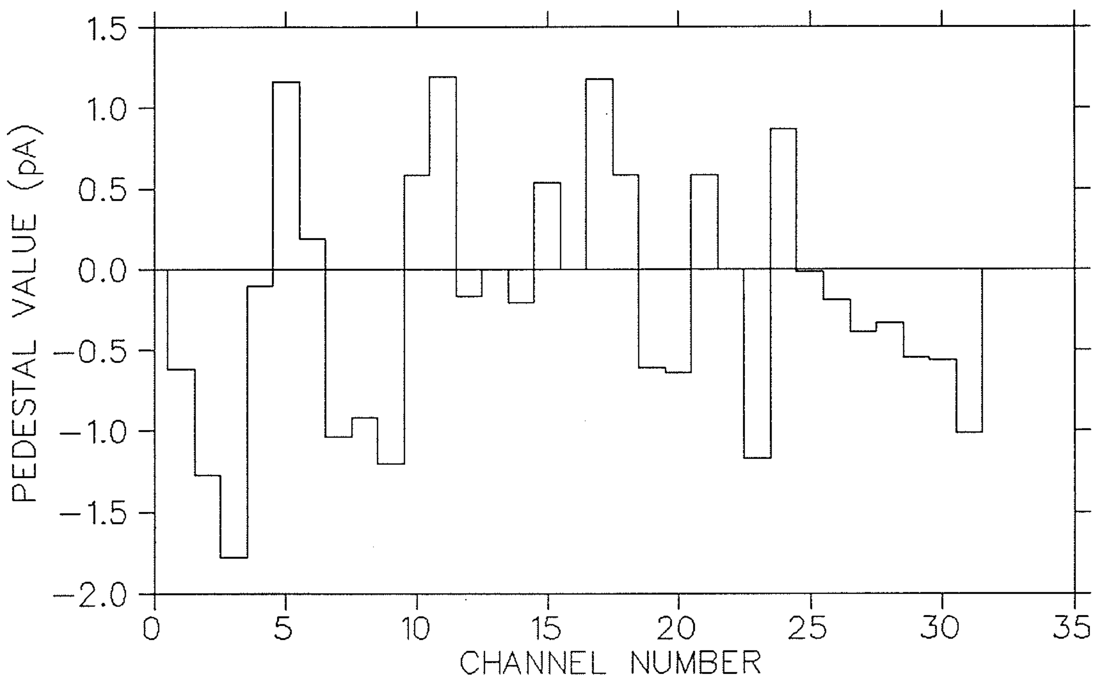

Figure 28: *Pedestal values for the 31 preamplifiers taken over a 30 minute test run with no beam.*

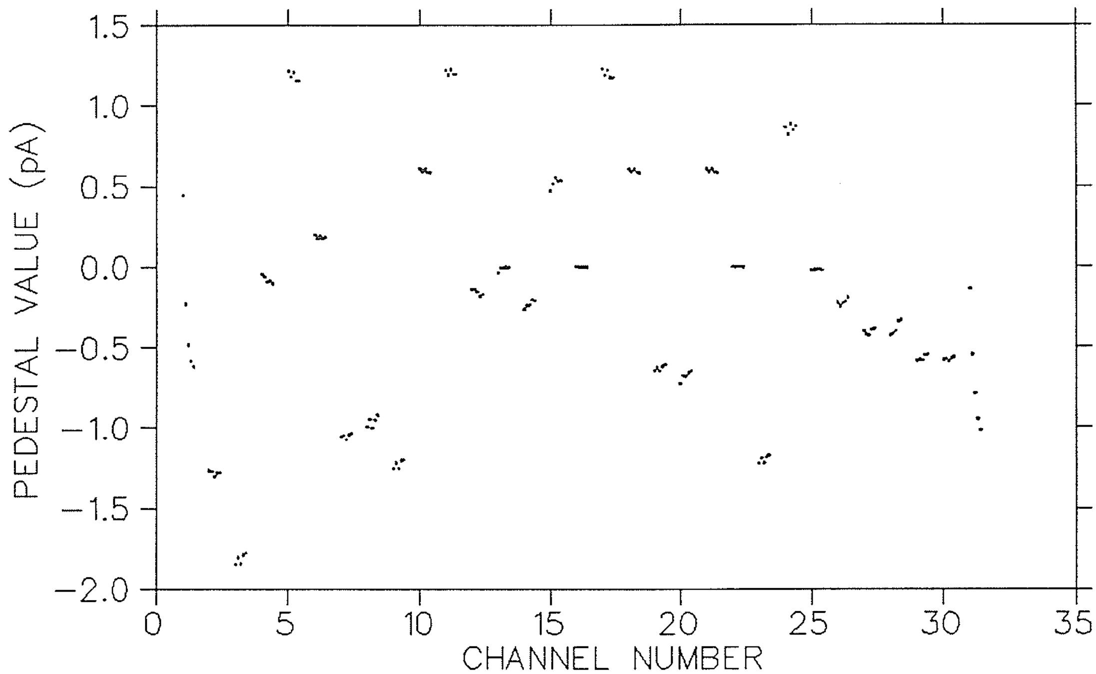

Figure 29: *Pedestal evolution over 2.5 hours for the 31 channel preamplifiers. Shown for each channel number are 5 sequential 30 minute runs.*

value for the second 30 minute run is plotted at 10.1, the third at 10.2 and so on. The unchanging values for channel 10 reveal a relatively constant pedestal value for the 2.5 hour time duration. Channel 1 shows an initial pedestal value of +0.4 pA. By the final 30 minute run, the pedestal has decreased to -0.6 pA. It appears that the outer channels underwent some sort of electrical discharge, but these "guard" channels are not used for any of the beam moment calculations. The pedestal values are not fluctuating by any significant amount and can therefore be neglected. The experiment will still require pedestal runs to ensure that pedestal values remain negligible.

The beamline setup for the prototype beam intensity profile monitor tests included an aircore steering magnet, a halo monitor, a transverse field ionization chamber and finally the profile monitor itself. Beam currents used

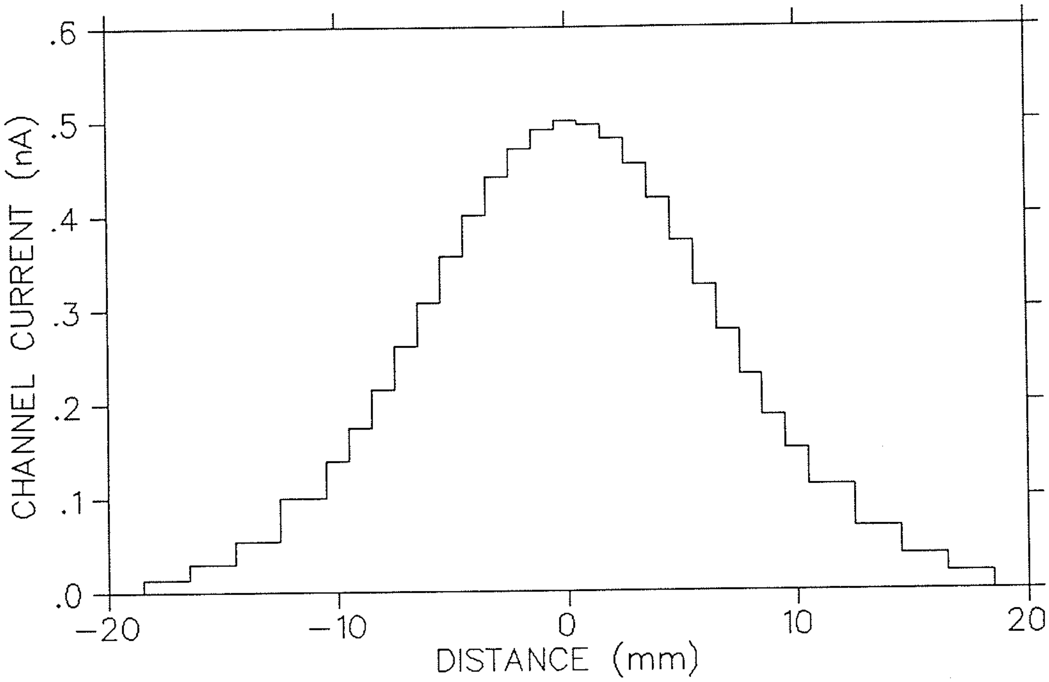

Figure 30: *Beam profile from Run # 108, February 1989 with foil strips. Beam current is 120 nA and channel gains have been matched in software.*

for the test runs were anywhere from 100 to 500 nA, and the beam spot was tuned from 5 to 15 mm in diameter. Fig. 30 shows a typical beam profile taken with foil strips in a February 1989 run with 120 nA beam current. Note that the central 21 channels are single width strips while the channels 2,3,4,5 and 27,28,29,30 are all double width strips. For the display of a beam profile, the double width channels have been extended over two strip widths and the horizontal scale has been converted to millimeters, centered on the central strip.

By histogramming the events for a single channel, an estimate of beam current fluctuations can be made. The left plot in fig. 31 displays the current detected from channel number 16. The beam noise for this plot is 20 pA (σ). This is a result of beam shape changes, position fluctuations and beam

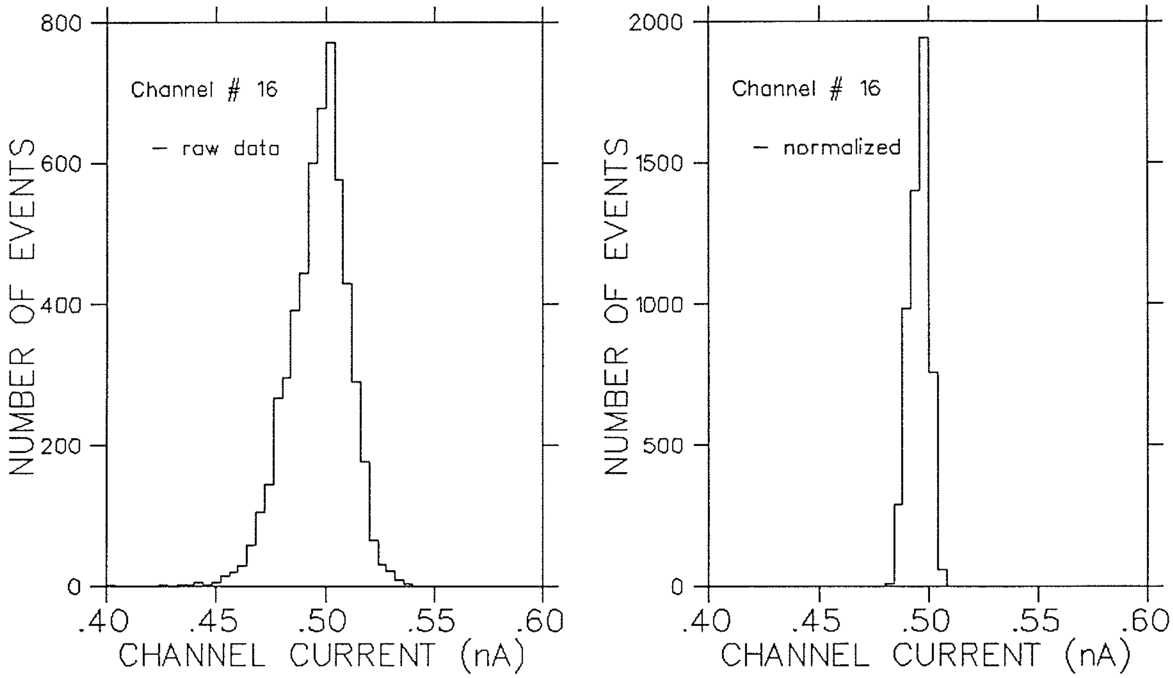

Figure 31: *Left plot: Channel 16 histogram of raw events for a 120 nA beam. Right plot: Channel 16 histogram of normalized events for a 120 nA beam.*

intensity variations. This number can be reduced if the beam intensity variations are compensated for. After normalizing each profile event, the right plot in fig. 31 reveals the beam noise corrected for intensity fluctuations as 7 pA (σ). This result will be used later in section 6.

In an attempt to demonstrate the ability of the monitor to detect beam centroid shifts of the order of 10 μm after one hour of data taking, a run was performed in which the aircore steering magnets stepped the beam between two locations. By scaling the steering magnet current from that required to produce a 1 mm displacement, a shift of 10 μm was applied to the beam. The calibration for the horizontal split plates performed identically to the vertical split plates, was determined to be 2.55 mV/μm. Using a square wave generator, a false asymmetry signal of 25.5 mV peak to peak was fed to the position servo loop. The two resultant profiles would then be expected to have a centroid shift of 10 μm. Three runs were performed to determine if the 10 μm shift was observable. These tests were performed with the channel gains not corrected. The test runs were 30 minutes in duration. The resulting average shift that was observed was 9.7 μm. The consistency in measurements of $\pm$ 2 μm was better than the accuracy that was measured ($\pm$ 3 μm) by recording profiles when no steering signal is applied. Note that pausing one second between centroid shifts will average out any beam position fluctuations greater or smaller than one second, but will enhance any fluctuations of the order of one second. Thus the inconsistency of the two results.

5.2.3 Observed Effects of δ-rays.

One unusual effect that has been observed for the outer channels is the appearance of negative currents as shown in fig. 32. Although the two outermost strips are not used for the determination of the beam distribution centroid and width, this effect could influence the signal of the other strips, providing a distorted beam distribution.

The source of this effect was traced to the collection of electrons. In the secondary electron mode, emitted electrons from the strips produces the beam profile and any negative signal on the signal strips would either suggest a collection of negative charges or an emission of positive charges. The large negative signals detected for the outer strips (of the order of pA's) cannot be explained by the emission of positive charges from the foil. The only alternative would be the collection of the negative charged electrons. Recall eq. 22 that describes the high energy electrons which are emitted from the

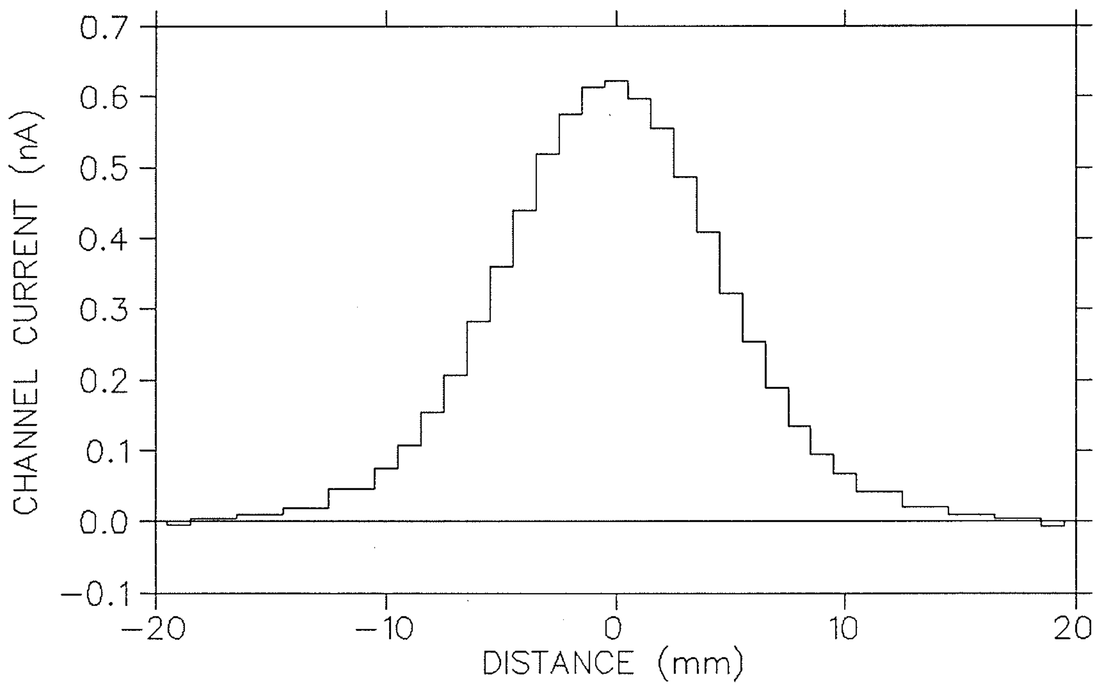

Figure 32: *Negative channel currents shown for channels 1 and 31. Run # 84 of October 1989, 90 nA beam current.*

aluminum foil as a result of elastic collisions with the incident protons. To determine the range of these δ-rays in aluminum [27],

$$\overline{R} = 0.412\, T_e^n \text{ g cm}^{-2} \tag{53}$$

where $n = 1.265 - 0.0954\, ln(T_e)$ for $0.01 < T_e < 3$ MeV. By inserting the appropriate values and using an aluminum density of $\rho_{med} = 2.70$ g cm^{-3}, the range for the maximum energy δ-ray is found to be 0.67 mm! This is the equivalent of 80 foils. A significant number of these δ-rays produced from the upstream foils could greatly influence the readout of the monitor.

A computer code was generated to simulate the emission of the high energy electrons (δ-rays) from upstream foils. An electron was followed from its point of origin to see if it could escape from the foil in which it was produced. Escaping electrons were tracked to the foil strips. Once an electron reaches a foil strip, two results are possible. If it has enough energy to pass through the foil strip, it will emit other secondary electrons from both surfaces of the strip [30]. If it does not have enough energy to escape the foil strip, it will stop. The criterion that must be met for this second case to provide a positive current on that particular foil strip is that the yield of secondary electrons from the surface of the foil must be less than one. This means that, on average, for each electron collected by the strip, less than one secondary electron is emitted from that foil strip.

A Gaussian beam profile of width 14 mm full width $\frac{1}{e}$ was assumed incident on the upstream high voltage foil. The predicted contribution of the high energy electrons to the final beam profile is shown in the upper plot of fig. 33. Notice that at the central strips, there is an increase in signal current

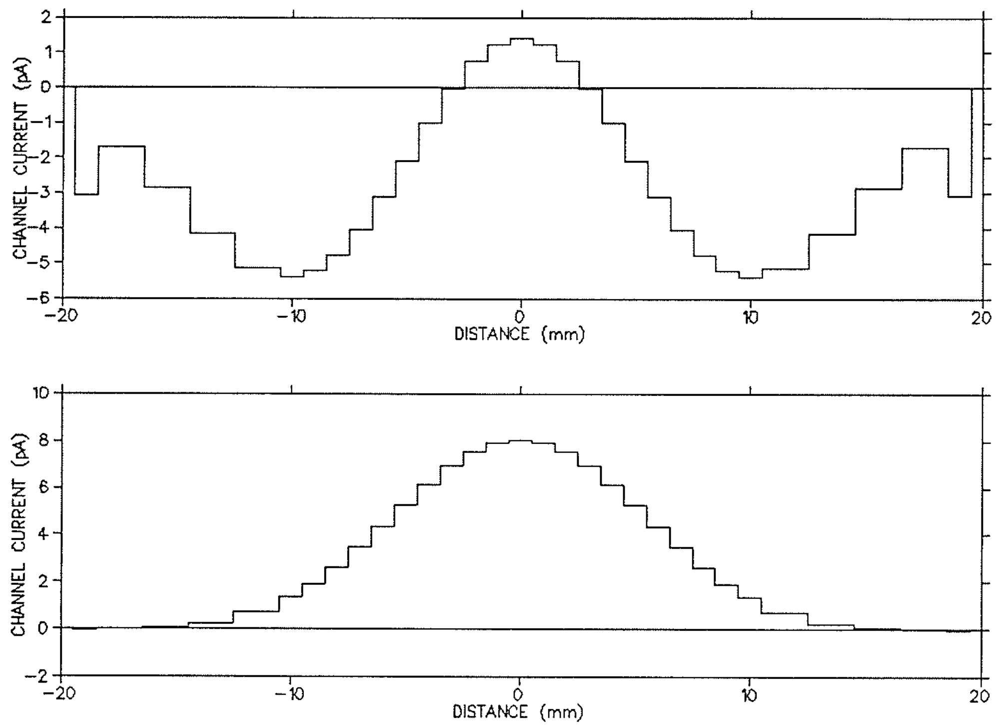

Figure 33: *Upper plot: Computed contribution to the beam profile from δ-rays produced in the upstream high voltage foil. Lower plot: Computed contribution to the beam profile from δ-rays produced in a foil located upstream of the high voltage foil.*

while the outer strips do indeed display a negative signal. It was seen in eq. 22 that at larger angles, the electrons produced in the elastic collisions have much less energy. The electrons of higher energy, able to penetrate the foil and generate more secondary electrons would be expected to travel along the beam axis, thereby increasing the signal current on the central strips. The lower energy electrons are emitted at larger angles, thereby striking the outer foil strips. These electrons are most likely to be collected in the foil strips. It should be noted that one major assumption made by this model is that as the electron loses energy in the aluminum, its trajectory remains a straight line. This assumption may be valid for electrons above several keV but is not valid at low energy. If we limit ourselves to δ-rays above 10 keV, the energy required to traverse 1.0 μm of aluminum, this assumption should be reasonable for a first order approximation.

Calculations performed for a foil located upstream of the high voltage foil, shown in the lower plot of fig. 33, revealed that the effect was less dramatic than for the foil immediately upstream of the foil strips. By summing together the beam profile expected by the incident profile as well as the contribution due to the δ-rays, a final profile was generated as shown in fig. 34. The predicted negative signal currents are only about half the observed effect, but the agreement is reasonable given the approximations of the model.

5.2.4 Identical Profiles.

The gain calibration algorithm discussed in the following section is based on the principle that if the actual beam profile is measured at two locations on the monitor, the two measured profiles should be identical. The problem is that during the data taking, the actual beam shape and position are not

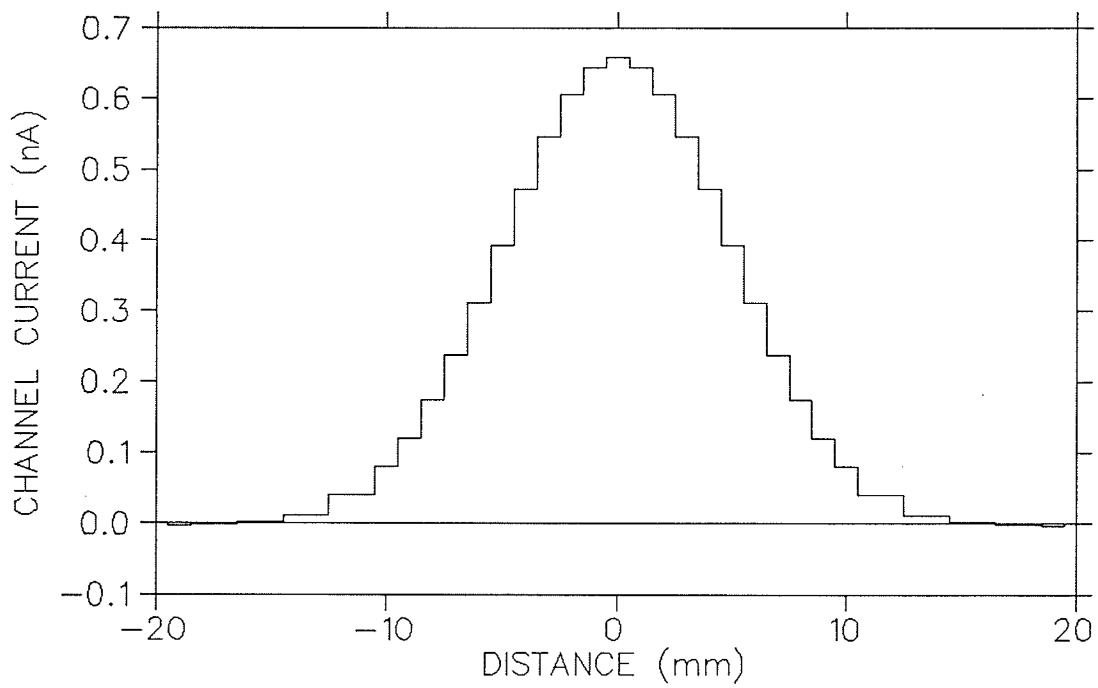

Figure 34: *Computed beam profile which includes the negative channel contribution from δ-rays.*

constant and cannot be independently controlled. This technique can still be used if the variations in beam shape and position are of a much longer time scale than the data runs. Short integration times for the electronics helps to cancel slow drifts in the actual beam parameters. Regardless of the length of the integration time, the data taking will still couple to the frequency of beam position fluctuations that correspond to the beam shift frequency (ie. the rate at which the beam is stepped from one position to the next). For example, consider the case where the beam is left in a fixed location for one second, then shifted to a new location for another second. If this process is repeated sequentially, then any beam position fluctuations that occur at the 1 Hz rate will correspond to differences in the two final measured beam profiles. Any beam fluctuation that occur at other frequencies will be averaged out. If the process is repeated randomly, such that the beam has a 50 % chance of being found in either of the two locations, then even the beam fluctuations at the 1 Hz level will average out. With the electronic setup as previously described for the profile monitor, the shortest possible event would correspond to one second integration time.

To determine any differences in producing two identical profiles, a data run was recorded with the beam in a fixed position. The length of this run was one hour (i.e. 3600 events). The first step was to produce two profiles by averaging the first half hour, i.e. event numbers 0 to 1800, as profile A and the second half hour, i.e. event numbers 1801 to 3600, as profile B. The beam profile is shown in the top plot of fig. 35 while the differences in the two resulting profiles is shown in the middle plot of fig. 35. This corresponds to a change in beam centroid of 24 μm and a change in full width $\frac{1}{e}$ of 58 μm. The second step was to create the two profiles by alternating the events for each profile such that all even numbered events are averaged into profile A and all odd numbered events are averaged into profile B. The resulting difference in

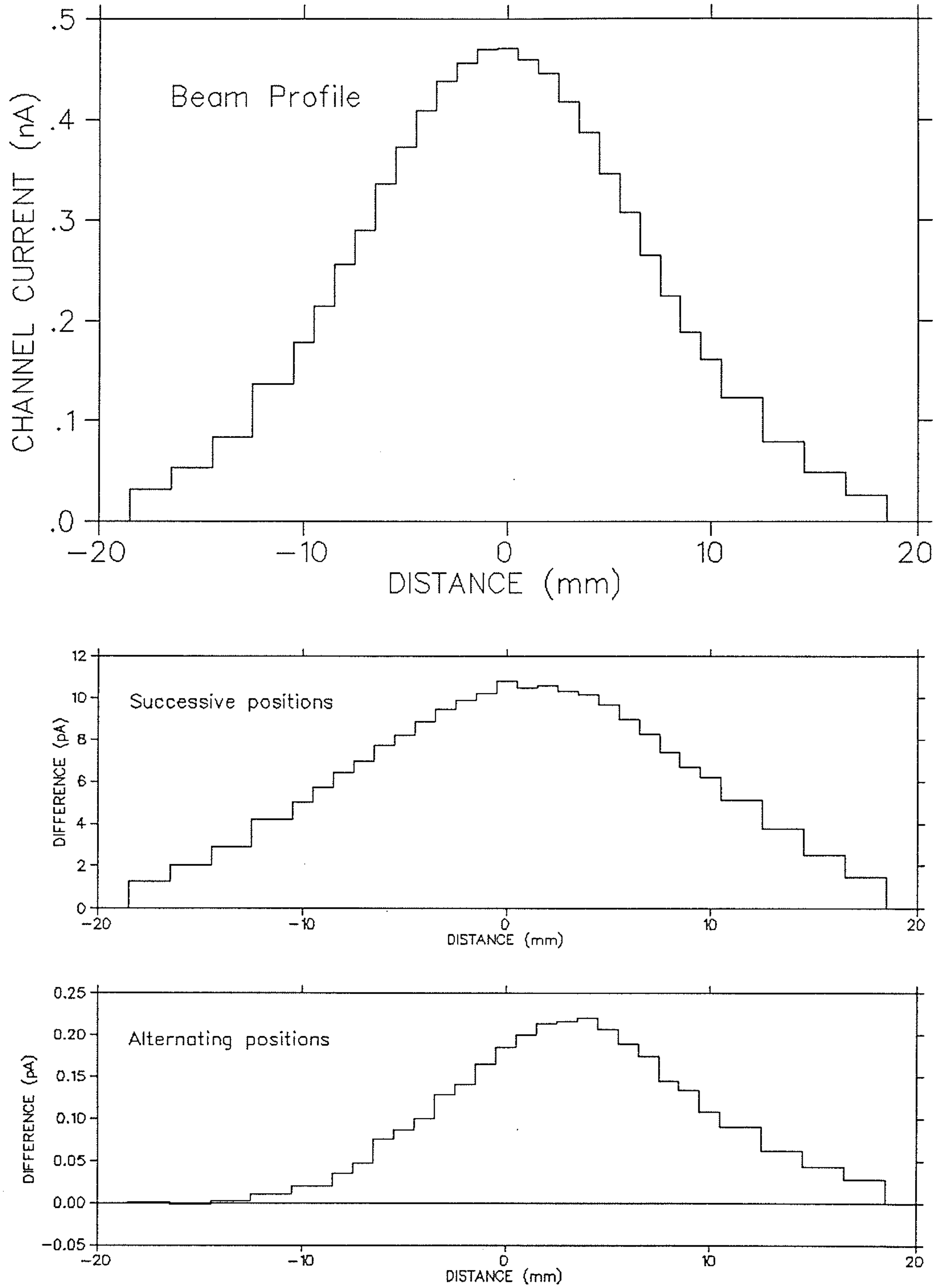

Figure 35: *Upper plot: Beam profile of run # 74 October 1989 with servo loop on and 100 nA beam current. Middle plot: Difference between two profiles generated by locating beam in successive positions. Lower plot: Difference between two profiles generated while alternating beam positions.*

the two profiles is a $2\mu m$ change in beam centroid and no detectable change in the full width $\frac{1}{e}$. Three other runs were processed in a similar manner verifying these results. It was clear from these results that identical profiles should be generated for the gain calibration routine through the alternating technique, i.e. locating the beam in position A for only one event, then relocating the beam position to location B for one event and repeating the cycle until the required statistical accuracy has been reached. Note that there is also a possibility of randomizing the profile location to reduce the error even further.

6 Gain Calibration.

Before taking data in the parity violation experiment, there remains the task of matching each set of preamplifier channel gains for the profile data acquisition. This gain calibration, as stated in section 2, must be performed to within ± 1.0 % per channel. The gain factor would take into account the electronic gain of each operational amplifier circuit and any variations in surface efficiency, surface area or position of the aluminum foil strips. The algorithm only has to match the relative gains of the channels for each harp. It does not have to be concerned with the absolute normalization between all four of the foil strip planes. The latter can be accomplished by normalizing the current over the entire strip array with the beam current signal of the transverse field ionization chambers.

6.1 Two Profile Algorithm

The simplest method for gain calibration is to make use of identical beam intensity profiles by positioning the beam at two accurately determined locations. The beam can be locked on the split foils to keep the beam stable during data taking and the position readouts of the split foil pack for the two locations will give the shift of the beam profile. The gain factors can then be determined in software by requiring the two profiles to be identical with the exception of the known centroid shift. Analytically, the current signals for the i^{th} channel of the 2 distinct profiles are given by:

$$I_i^a = g_i I_o e^{-(x_i+\frac{\delta_o}{2})^2/x_o^2} \tag{54}$$

$$I_i^b = g_i I_o e^{-(x_i-\frac{\delta_o}{2})^2/x_o^2} \tag{55}$$

where $g_i(\sim 1.0)$ is the unknown gain of the i^{th} channel, x_o is the $\frac{1}{e}$ half width of the beam profile, I_o is the normalization factor and δ_o is the total centroid shift from one profile to the other. The gain calibration algorithm introduces a shift of δ $(= -\delta_o)$ to the second profile. Any differences in the two profiles will be a result of gain errors and can be corrected by applying the gain correction factors G_i such that

$$G_i I_i^a = G_{i+\delta} I_{i+\delta}^b. \tag{56}$$

When the gain correction factors G_i $(= \frac{1}{g_i})$ are applied to the observed foil strip current readings, the corrected current distribution is exactly equal to the true beam intensity distribution and is independent of the position of the beam at the monitor. The accuracy to which the gain correction factors G_i must be determined from the algorithm is obtained as follows. For mathematical simplicity the shift δ is chosen to be an integer number of channels. The gain of channel $i + \delta$ is:

$$G_{i+\delta} = \frac{g_i G_i}{g_{i+\delta}} \frac{e^{-(x_i+\delta_o/2)^2/x_o^2}}{e^{-(x_i+\delta-\delta_o/2)^2/x_o^2}}. \tag{57}$$

The propagation of errors gives

$$\sigma_{G_{i+\delta}}^2 = \sigma_{G_i}^2 \left(\frac{\partial G_{i+\delta}}{\partial G_i}\right)^2 + \sigma_\delta^2 \left(\frac{\partial G_{i+\delta}}{\partial \delta}\right)^2. \tag{58}$$

Now,

$$\frac{\partial G_{i+\delta}}{\partial G_i} = \frac{g_i}{g_{i+\delta}} e^{-(x_i+\frac{\delta_o}{2})^2/x_o^2} e^{(x_i+\delta-\frac{\delta_o}{2})^2/x_o^2} \tag{59}$$

$$\frac{\partial G_{i+\delta}}{\partial \delta} = \frac{g_i G_i}{g_{i+\delta}} \frac{2(x_i+\delta-\frac{\delta_o}{2})}{x_o^2} e^{-(x_i+\frac{\delta_o}{2})^2/x_o^2} e^{(x_i+\delta-\frac{\delta_o}{2})^2/x_o^2} \tag{60}$$

so

$$\frac{\sigma^2_{G_{i+\delta}}}{G^2_{i+\delta}} = \frac{\sigma^2_{G_i}}{G^2_i} + 4\sigma^2_\delta \frac{(x_i + \delta - \delta_o/2)^2}{x^4_o}. \tag{61}$$

Hence;

$$\frac{\sigma^2_{G_{i+\delta}}}{G^2_{i+\delta}} = \frac{\sigma^2_{G_i}}{G^2_i} + 4\sigma^2_\delta \frac{(x_i + \delta_o/2)^2}{x^4_o} \tag{62}$$

where $\delta = -\delta_o$. Starting from the central channel $i = 0$ where the gain is most accurately determined, the error on neighbouring channels increases parabolically with distance from the center of the monitor as seen in eq. 62. This can be rearranged to give the total fractional error on the i^{th} strip as

$$\frac{\sigma^2_{G_i}}{G^2_i} = \frac{2\sigma^2_\delta n}{x^4_o} \left[\frac{(n-1)(2n-1)}{3} + (n-1)\delta + \frac{\delta^2}{2} \right] \tag{63}$$

where $n \equiv \frac{i}{\delta}$. The readout system for the split plates is designed for a reproducibility of ± 13 μm which leads to an error in the beam shift of ± 18 μm. From eq. 63, for the outer single width strips ($i = 10$), an uncertainty of $\sigma_\delta = 15$ μm for a $\delta = 1$ mm beam shift (n =10 mm^{-1}) of an $x_o = 10$ mm half width $\frac{1}{e}$ beam spot would translate into a gain error of 0.8 %. The same calculation for a $\delta = 10$ mm beam shift ($n = 1$ mm^{-1}) gives a fractional gain error of only 0.3 %. A shift that will determine the gains to below ± 0.5 % for this two step algorithm is a shift of the order of 10 mm. The reason to keep the gain error below 0.5 % rather than the ± 1.0 % mentioned earlier is that there are other systematic errors that need to be considered.

6.2 Three Profile Method.

As stated above, the two profile method does require a profile shift of the order of 10 mm, which was far too large for the aircore steering magnets in the beamline configuration used. It was thus necessary to use the last bending magnet in the beamline and generate the profiles consecutively. However, the assumption must be made that the profiles do not change shape between the two measurements. This condition could not be met in the test data, so the two profile method was abandoned.

An alternate method relies on three identical beam intensity profiles shifted by smaller amplitudes than required for the two step procedure. The aircore steering magnets of the fast feedback system can be controlled to steer the beam $\pm$ 1 mm from a central position to produce three profiles. The essential feature of this calibration procedure is that the position shift between neighbouring profiles is identical. The two step gain calibration is performed on the two sets of neighbouring profiles independently. By demanding consistency of the two independent calibrations, the gains of the preamplifier channels can be determined to sufficient accuracy without knowing the absolute value of the beam profile shift.

The three step algorithm was to provide a gain calibration technique which would require as little manipulation of beamline components as possible. The advantage of this method is that a 1 mm beam shift can easily be accommodated by the aircore steering magnets. By connecting the voltage output of a computer controlled digital to analog converter (DAC) to the aircore steering magnet power supplies, the beam centroid can be continuously scanned through the three profile locations. Now recall that when the servo loop is on, it will try to position the beam median on the split plate reference point. In this case, the DAC output signal was added to the asymmetry signal. For the gain calibration, the loop no longer positioned the beam at the center of the monitor to zero the asymmetry signal, but instead tried to position the beam at a point where the asymmetry signal canceled the corresponding DAC output. The beam was then positioned at the three locations on the monitor while the servo loop was still operational. The quick response of the DAC allowed for compensation of beam fluctuations, since if there was any sort of change in the beam shape, then continuously scanning through the various beam positions should average out these differences as shown in section 5.2.4. Using the two step algorithm with a profile shift of 10 mm required the control of a beamline bending magnet which may not be stepped rapidly. If the beam should change its shape during the profile data taking, the resulting difference in the two beam profiles would be incorrectly assumed to be a result of gain variations from channel to channel. As shown in the monitor performance section, the reduction of beam shape variations for the quick response DAC setup can be two orders of magnitude.

6.2.1 Gain Calibration Program.

The gain calibration program used to match the central twenty one single strip channels is shown in the appendix. The program input required the channel number, the three profile current values and the corresponding current variance extracted from the histogram of current events on each channel. The first step of the program was to select profiles A and B and then calculate the centroid shift between the two.

To say "calculate the centroid shift" may be misleading since the true centroid must be determined by the use of the entire profile including the tails of the beam. Since the tails of the beam profile extend outside of the twenty one single channels, the shift of the centroid was calculated indirectly. Use is made of the spline routine FLATC.FOR [31], fitting a continuous function for the two profiles. The advantage of FLATC.FOR is that it has the ability to smooth the fitting function. Note that a spline function does not assume any type of distribution and is a model independent interpolation. Starting from the center channel and interpolating out six channel widths from the center, the centroid value $\sum x_i I_i'$ is determined where x_i is the location of I_i', the interpolated current. The centroid is then recalculated, but instead of beginning at the center channel, the calculation begins at the currently calculated centroid value. Again interpolating out six channel widths from the centroid value, $\sum x_i I_i'$ is recalculated. This process is repeated until the centroid value for profile A, 'EPSA', and for profile B, 'EPSB', changes less than the centroid tolerance CENTOLL. Notice that the final results for EPSA and EPSB are not necessarily the true centroids for profiles A and B, but assuming that profiles A and B are identical, the difference between EPSA and EPSB will still be the centroid shift, which is the important variable.

Once the centroid shift has been estimated by the gain calibration algorithm, the gains of all channels are determined from eq. 56. This algorithm assumes that the applied profile shift δ, is approximately one channel width. Since the actual shift may not be exactly one channel width, it is necessary to recalculate the shift and continue the gain corrections until changes in the corrections are below the gain tolerance GTOLL. Since eq. 56 simply gives a relation of the channel gain in question to its neighbour, there is the additional requirement that at least one of the channel gains be known. This constraint can be satisfied by simply defining the central channel gain, for example, to be exactly 1.0. Subsequently, the other channel gains can be matched to the central channel.

Once the gain corrections have been completed for the first and second profiles, then the entire procedure was repeated for the second and third profiles. From the first pair of profiles, the calculated centroids are XA1 and XB1 and from the second pair of profiles, the calculated centroids are XA2 and XB2. Now XB1 and XA2 are the second profile centroids and they *must* agree, so too *must* the corresponding shifts XB1-XA1 and XB2-XA2. The value of the shift is then modified by the program until the centroid values for profile two and the two shifts agree to within $\pm$ 1.0 μm.

6.3 Performance of the Gain Calibration Algorithm.

This algorithm was initially tested with simulated data by generating random gains varying by $\pm$ 10 %. Using a Gaussian profile shifted by 0.8 mm and multiplying the channel currents by the randomly chosen gain, three equally spaced profiles were generated. The gain calibration was determined to be accurate to within $\pm$ 0.001 % for up to 31 channels as shown in fig. 36. Investigation of the relatively large errors for the outer most channels revealed that this error is due primarily to errors in determining the second derivatives at the end points for the spline function used by the gain calibration algorithm.

To properly test the results of this gain calibration algorithm, it is necessary to generate simulated data with realistic noise values such as beam and electronic noise, shift error, normalization error and the strip position and width error. All errors are added to the generated Gaussian profiles used for the basic beam profiles. Each profile has been generated after assuming

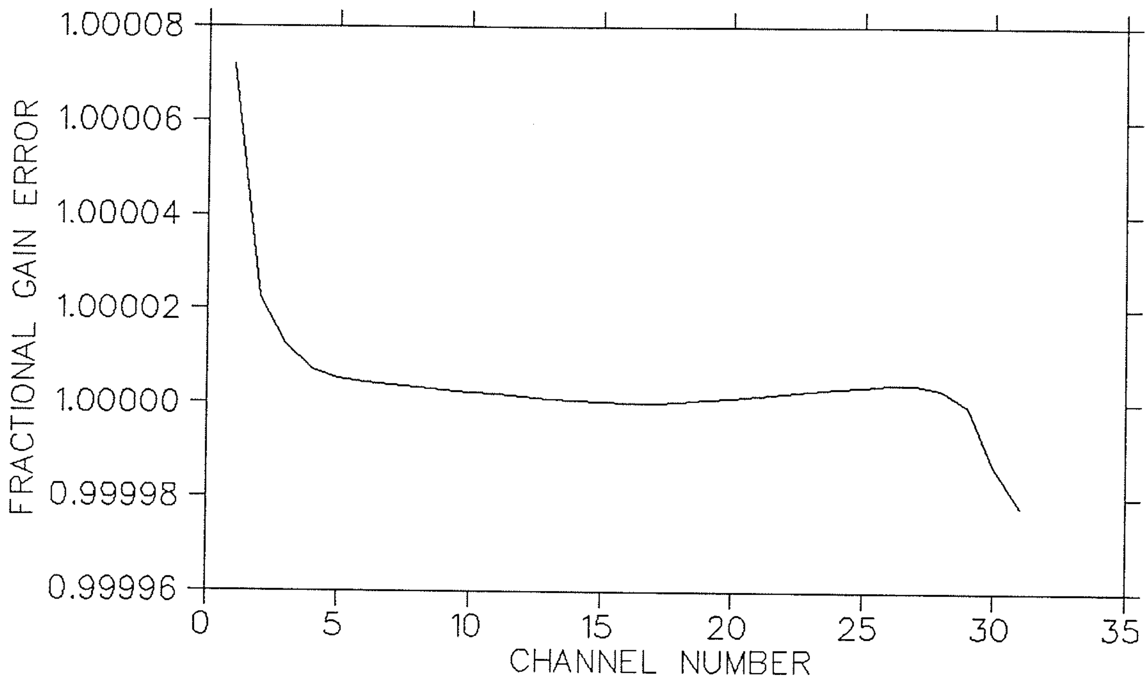

Figure 36: *Computer simulation gain calibration attempt with the profile shifted by 0.8 mm and generated with ± 10 % gain variations and no noise.*

twenty minutes of data acquisition time and 500 nA beam current.

6.3.1 Beam and Electronic Noise.

The beam and electronic noise parameters can be treated as one noise source and each can be reduced by increasing the run time of profile acquisition. As demonstrated in the previous section, the tested electronic preamplifier channels which operated with a 0.5 second integration time constant produced a beam off histogram with an electronic noise of $\sigma_{el} = 0.5$ pA. Also from the previous section, the beam noise which is associated with fluctuations in the beam shape was determined from a test run with the fast feedback servo loop on as a maximum of $\sigma_{beam} = 7.0$ pA for all channels. This is after the beam profiles have been corrected for any changes in intensity.

For a realistic test value, the total beam and electronic noise was generated randomly for each channel from a normal distribution with $\sigma_{total} = 7.0$ pA.

6.3.2 Normalization Error of Beam Profile.

The beam profile can also change its intensity during the gain calibration profile run. This will appear as beam noise as discussed above unless a reading of the beam current from some normalization monitor can be obtained, correcting for the observed change in intensity. For the final experimental setup, the beam intensity will be read directly from the transverse field ionization chambers. The smallest detectable change in beam current for these ion chambers based on their design specifications is one part in 10^9 after 300 hours running time. For each profile event read in by the monitor in one second, the smallest detectable change in current from the transverse field ionization chambers is one part in 10^6, or $\sigma_{norm} = 0.0001$ %, and this is negligible for the gain calibration algorithm.

6.3.3 Beam Shift Error.

Unlike the two step algorithm, the three step gain calibration does not require the input of the profile centroid shift. The only effect that would result in a gain correction error is if the shift is an asymmetric shift for the three profiles, that is, if the shift from profile one to profile two is not equal to the shift from profile two to profile three. Based on previous experience with these steering magnets, a worst case error of $\sigma_{shift} = 1$ % was assumed. This does not mean that the shift is known to $\pm$ 1 %, but rather that the two profile shifts are equal to within $\pm$ 1 %.

6.3.4 Strip Position and Width Error.

As discussed in section 3.1, viewing the laser cut foil strip array under a travelling microscope revealed that the strip positions varied below the 10 μm level, thus $\sigma_{width} = 0.01$ mm. Since the spacing of the strips was 0.1 mm and the array must be tensioned such that no two strips are in contact, the worst case error for the strip position was half a foil strip spacing, or $\sigma_{pos} = 0.05$ mm.

Before any data were taken, both calibration procedures were tested with simulated data. Computer generated profiles with foil strip current and noise distributions as expected for a 1 hour calibration run during actual parity data taking with a 500 nA proton beam were analyzed to test the extraction of gain correction factors G_i from a preset random gain distribution g_i. Results of the two procedures are shown in fig. 37 where the product $G_i g_i$ is plotted for each foil strip channel. Note that for correctly deduced G_i, the product $G_i g_i = 1.00$. The error bars are the statistical fluctuations expected for a 1 hour calibration run. The upper part of fig. 37 shows the results of the two step algorithm and the lower part shows the results of the three step (2×2) algorithm. The computer simulations were made for 31 single width foil strips. Truncation of a symmetric intensity profile distribution does not introduce any error on the centroid determination. For non-symmetric intensity profiles, truncation may be introduced as long as the shape of the profile is known and the truncated parts are estimated through fitting the measured profile using the known shape as a template.

The final test for the gain calibration algorithm was to perform the gain calibration on real data events. Fig. 38 shows two attempts performed during a December 1989 test run. Shown are gain calibration results for run # 60

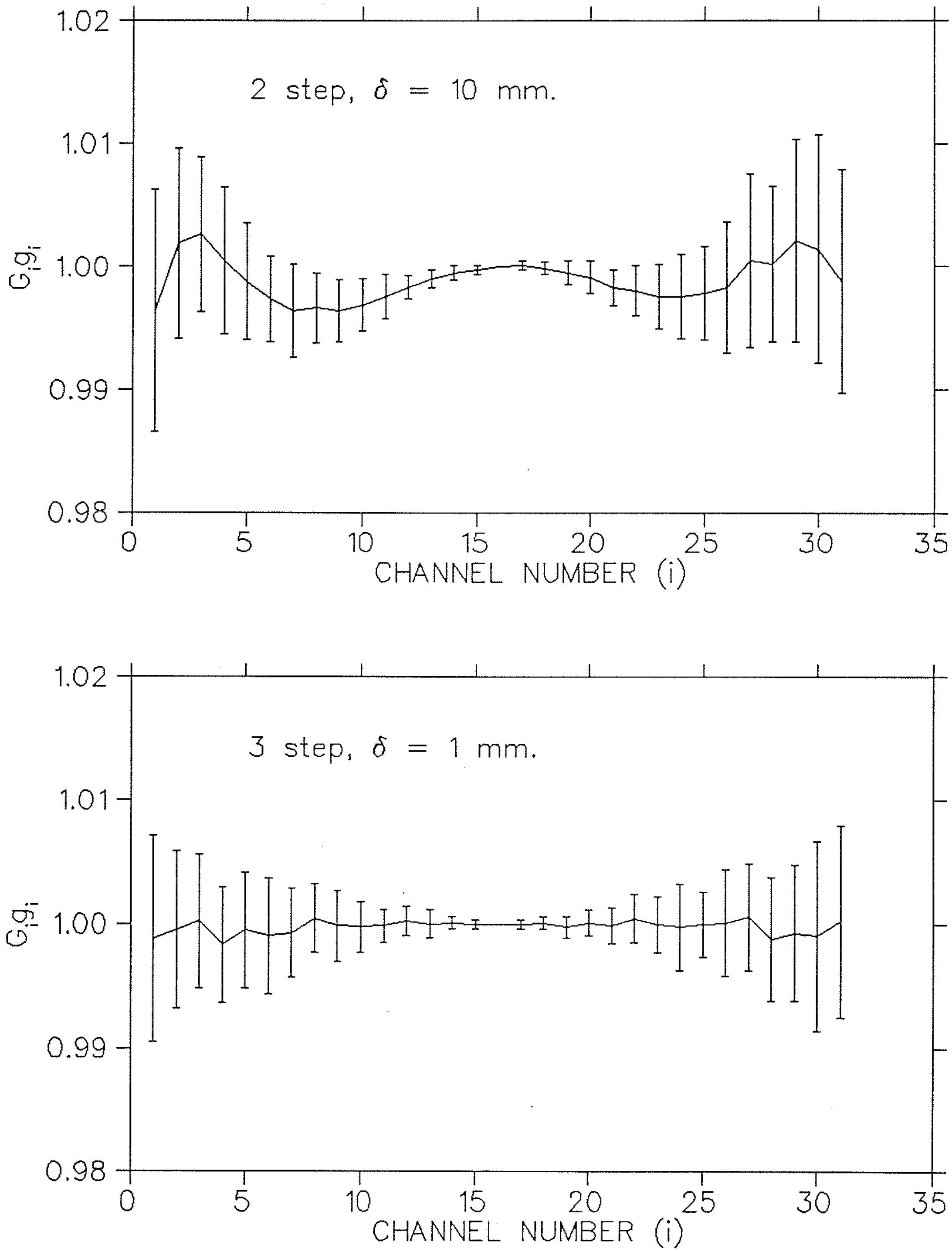

Figure 37: *Comparison of the computer simulations for the two (upper) and three (lower) step gain calibration algorithms. Plotted on the abscissa is the product G_ig_i which should be exactly equal to 1.0, versus channel number i. The statistical error is that expected for a one hour calibration run at 500 nA.*

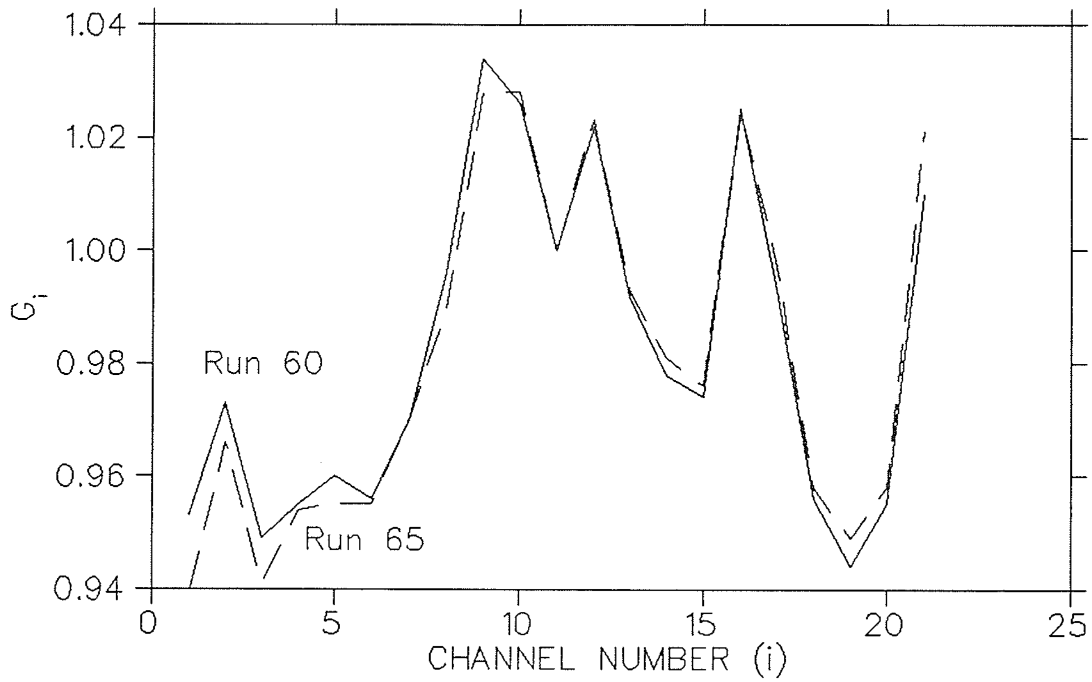

Figure 38: *Three step gain calibration results for two runs separated by two hours. Beam was displaced by 3 mm for the second gain calibration run.*

and # 65 on the central 21 single channel foil strips. The two runs were taken two hours apart. After the first run, the 20 mm full width $\frac{1}{e}$ beam was moved 3 mm (3 channel widths) to the right using the beamline bending magnet. The normalization of event profiles was performed using a normalization foil placed directly behind the foil strip array. Due to electronic noise, this method of normalization is less accurate than with the planned use of the transverse field ion chambers. Also note that the beam current for these test runs was only 100 nA. This decreases the statistics of the profile events below the level that will be available during the data taking of the parity violation experiment. As discussed in section 2, systematic errors such as the non-linear response of the monitor with respect to beam intensity fluctuations would show up as a systematic gain correction on the monitor. As seen in fig. 38, all systematic and statistical errors of the gain calibration

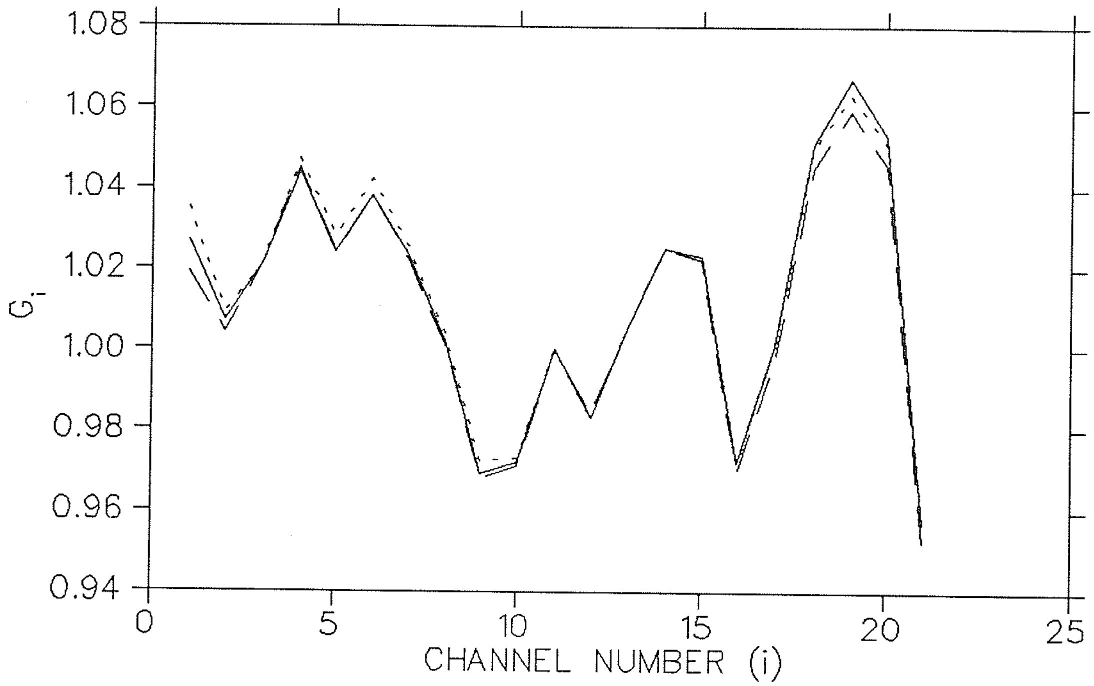

Figure 39: *Comparison of an independent gain calibration algorithm and the proposed three step algorithm for real data profiles. Plots are the independent gain calibration algorithm with 8 fitting parameters (solid), with 7 parameters (dashed) and the three step calibration algorithm (dotted).*

algorithm are below their required level, demonstrating the absence of any detectable non-linear effects.

Fig. 39 shows the three step algorithm results for data from a February 1990 test run # 108. Included in the figure are results from an existing gain calibration program with 7 and 8 fitting parameters compared with the three step algorithm. The agreement of the various methods would support the assumption that the three step algorithm is performing as expected. After observing the satisfactory performance of the three step gain calibration algorithm, the reasons for its implementation would be its fast calibration time, its insensitivity to beam shape and that it has demonstrated ability to obtain high precision for simulated profiles generated with a limited centroid shift distance.

7 Conclusions.

It has been the intent of this thesis to describe in detail the construction, evolution and implementation of a dual-function beam intensity profile monitor used in secondary electron emission mode of operation for a parity violation experiment in $\vec{p} - p$ scattering at 230 MeV. It has been demonstrated that an SEM device provides a linear response far better than that of a similar gas gain monitor. The fundamental problem of low gain for the SEM device was compensated for by high quality, low noise electronics.

Using the split plate SEM monitor to drive a fast analog position feedback system, it has been demonstrated that beam median stability better than $\pm$ 5 μm can be achieved. Also demonstrated was beam centroid determination, by the use of aluminum foil strips, to better than $\pm$ 3 μm for 30 minutes of data taking. Both of the above requirements were accomplished for a 20 mm full width $\frac{1}{e}$ Gaussian beam spot of approximately 100 nA.

Finally, a gain calibration algorithm that is computer controlled and does not require a beam shift of more than 2 mm total shift has provided gain correction factors to better than $\pm$ 1.0 %. In addition to the above performance characteristics, the SEM monitor substantially reduces mass placed in the beam (with respect to conventional gas filled devices), minimizing the effects of multiple scattering.

Parameter	Design Specifications	Performance
median stability	$\pm$ 10 μm (fluctuations < 1 Hz)	$\pm$ 5 μm (fluctuations < 1 kHz)
centroid determination	$\pm$ 10 μm (one hour)	$\pm$ 3 μm (one hour)
signal pedestal (bias current)	$\pm$ 1.0 pA (all channels)	$\pm$ 0.1 pA (short term drifts)
electronic noise	$\pm$ 60 pA (one second integration time)	$\pm$ 7 pA (one second integration time)
gain calibration	$\pm$ 1.0 % (all channels)	$\pm$ 1.0 % (better for inner channels)
split plate position accuracy	$\pm$ 13 μm (relative position)	$\pm$ 13 μm (relative position)
strip position determination	$\pm$ 5 μm	$\pm$ 4.5 μm

Table 4: *Comparison of monitor design criteria and the performance observed for the SEM monitor.*

A Appendix: Gain Calibration Program.

```
C*************************************************************************
C
C      GAIN MATCHING OF THREE PROFILE DATA FILES.
C
C      PROGRAMMER A.M. SEKULOVICH 1990
C
C*************************************************************************

       PROGRAM GAINMATCH
       INTEGER*4 FLAG,IISET,MODE,FLAG2,COUNT
       REAL*8 VAR0,VAR1,I1,I2,EPS2,FLEXB
       REAL*8 IA,IB,IAA,IBB,X,YA,YB,Y2A,Y2B,DXA,DXB,NUMA,NUMB,GAIN
       REAL*8 EPS,AA,BA,CA,DA,AB,BB,CB,DB,DENOMA,DENOMB,FLEXA
       REAL*8 EPSA,EPSB,I11,I12,I21,I22,TEMPA,IC,ICC,CENTOLL
       REAL*8 SHIFT,S11,S12,XA1,XB1,XA2,XB2,IASIG,IBSIG,ICSIG,GTOLL
       DIMENSION IA(21),IB(21),IAA(21),IBB(21),IASIG(21),IBSIG(21),ICSIG(21)
       DIMENSION Y2A(21),X(21),AA(21),BA(21),CA(21),DA(21),IC(21),HOLD(21)
       DIMENSION Y2B(21),AB(21),BB(21),CB(21),DB(21),FLEX(21),ULIMN(21)
       DIMENSION DXA(21),YB(21),DXB(21),GAIN(21),TEMP(21),FLEXB(21)
       DIMENSION YA(21),FLEXA(21)
       DATA CENTOLL,GTOLL/1.0E-05,1.0E-04/
       DATA VAR0,VAR1/0.0,1.0/
       OPEN (UNIT=8,FILE='INPUT.DAT',STATUS='OLD',READONLY)
       OPEN (UNIT=9,FILE='OUTPUT.DAT',STATUS='NEW')

C      DO LOOP TO READ IN THE THREE PROFILE DATA
C      COMPLETE WITH THE VARIANCE OF EACH CHANNEL.

       DO I=1,21
         READ(8,100)COUNT,IA(I),IASIG(I),IB(I),IBSIG(I),IC(I),ICSIG(I)
         X(I)=FLOAT(COUNT)
         GAIN(I)=VAR1
       END DO
       MODE=0

C      IISET IS ZERO IF WE ARE USING THE FIRST TWO PROFILES.
C      IISET IS ONE IF WE ARE USING THE SECOND TWO PROFILES.

       IISET=0

C      PLACE THE FIRST TWO PROFILES IN IAA AND IBB AND
C      PERFORM THE GAIN CALIBRATION.

998    DO I=1,21
         IAA(I)=IA(I)*GAIN(I)
         IBB(I)=IB(I)*GAIN(I)
         IF(IISET.EQ.0)FLEXA(I)=100.0*IASIG(I)/IASIG(11)
         IF(IISET.EQ.0)FLEXB(I)=100.0*IBSIG(I)/IBSIG(11)
       END DO

C      THE SPLINE ROUTINE REQUIRES THE SECOND DERIVATIVE
C      (Y2 A & B) AT THE END POINTS OF THE DISTRIBUTION.

       Y2A(1)=-IAA(4)+4*IAA(3)-5*IAA(2)+2*IAA(1)
       Y2A(21)=-IAA(18)+4*IAA(19)-5*IAA(20)+2*IAA(21)
       Y2B(1)=-IBB(4)+4*IBB(3)-5*IBB(2)+2*IBB(1)
       Y2B(21)=-IBB(18)+4*IBB(19)-5*IBB(20)+2*IBB(21)

C      CALL THE SPLINING ROUTINE.

       CALL FLATC(21,X,IAA,FLEXA,YA,Y2A,DXA,AA,BA,CA,DA)
       CALL FLATC(21,X,IBB,FLEXB,YB,Y2B,DXB,AB,BB,CB,DB)
```

```
C      SET THE CENTROIDS AT 11.000, (IE THE CENTER
C      OF THE MONITOR) 'JA.EPSA' AND 'JB.EPSB'

       JA=11
       JB=11
       EPSA=0.0
       EPSB=0.0

C      CALCULATE THE CENTROID OF THE DISTRIBUTIONS
C      OUT TO PLUS AND MINUS 8 CHANNEL WIDTHS.

997    J=JA
       I1=AA(J)*EPSA**3.0+BA(J)*EPSA**2.0+CA(J)*EPSA+DA(J)
       NUMA=I1*(J+EPSA)
       J=JB
       I2=AB(J)*EPSB**3.0+BB(J)*EPSB**2.0+CB(J)*EPSB+DB(J)
       NUMB=I2*(J+EPSB)
       DENOMA=I1
       DENOMB=I2
       DO I=1,8
         J=JA+I
         I12=AA(J)*EPSA**3.0+BA(J)*EPSA**2.0+CA(J)*EPSA+DA(J)
         NUMA=NUMA+I12*(J+EPSA)
         J=JA-I
         I11=AA(J)*EPSA**3.0+BA(J)*EPSA**2.0+CA(J)*EPSA+DA(J)
         NUMA=NUMA+I11*(J+EPSA)
         J=JB+I
         I22=AB(J)*EPSB**3.0+BB(J)*EPSB**2.0+CB(J)*EPSB+DB(J)
         NUMB=NUMB+I22*(J+EPSB)
         J=JB-I
         I21=AB(J)*EPSB**3.0+BB(J)*EPSB**2.0+CB(J)*EPSB+DB(J)
         NUMB=NUMB+I21*(J+EPSB)
         DENOMA=DENOMA+I12+I11
         DENOMB=DENOMB+I22+I21
       END DO
       TEMPA=EPSA
       JA=INT(NUMA/DENOMA)
       JB=INT(NUMB/DENOMB)
       EPSA=NUMA/DENOMA-DFLOAT(JA)
       EPSB=NUMB/DENOMB-DFLOAT(JB)

C      IF THE NEW CENTROID CORRECTION IS NOT LESS
C      THAN 'CENTOLL', TRY AGAIN.

       IF(DABS(TEMPA-EPSA).GT.CENTOLL)GOTO 997
       FLAG=0

C      IF THE CORRECTION IS SMALLER THAN CENTOLL,
C      DETERMINE THE SHIFT 'EPS'.

       EPS=(JB+EPSB)-(JA+EPSA)
       IF(MODE.GE.1)EPS=SHIFT

C      APPLY THE SHIFT TO THE SPLINED DISTRIBUTIONS AND
C      CALCULATE THE GAIN CORRECTION FACTORS 'GAIN(I)'.

       DO I=1,11
         INC=10+I+IISET
         IF(EPS.GT.VAR1)EPS=0.99
         IF(INC.GT.20)GOTO 881
         I1=DA(INC)
         I2=AB(INC2)*EPS**3.0+BB(INC2)*EPS**2.0+CB(INC2)*EPS+DB(INC2)
         GAIN(INC+1)=GAIN(INC+1)*(I1/I2)

C      IF THE GAIN CORRECTION IS LESS THAT 'GTOLL',
```

```
C       INCREMENT 'FLAG'.

          IF(DABS(1.0-(I1/I2)).LT.GTOLL)FLAG=FLAG+1
881       EPS2=VAR1-EPS
          INC=11-I+IISET
          INC2=INC
          IF(EPS2.LT.VAR0)THEN
            EPS2=VAR1-EPS2
            INC2=INC-1
          END IF
          IF(INC.LT.1)GOTO 882
          I1=AA(INC2)*EPS2**3.0+BA(INC2)*EPS2**2.0+CA(INC2)*EPS2+DA(INC2)
          I2=DB(INC+1)
          GAIN(INC)=GAIN(INC)*(I2/I1)

C       IF THE GAIN CORRECTION IS LESS THAT 'GTOLL',
C       INCREMENT 'FLAG'.

          IF(DABS(1.0-(I2/I1)).LT.GTOLL)FLAG=FLAG+1
882     END DO

C       IF LESS THAN 20 CHANNELS ARE BELOW 'GTOLL',
C       TRY AGAIN.

        IF(FLAG.LT.20)GOTO 998

C       CHECK 'IISET' TO SEE IF GAIN CORRECTIONS HAVE
C       BEEN DONE FOR BOTH PAIRS OF PROFILES.

        IF(IISET.EQ.0)THEN

C       IF NOT, REPLACE 'IAA' AND 'IBB' WITH THE
C       SECOND PAIR OF PROFILES.

          DO I=1,21
            TEMP(I)=IA(I)
            IA(I)=IB(I)
            IB(I)=IC(I)
            FLEXA(I)=FLEXB(I)
            FLEXB(I)=100.0*ICSIG(I)/ICSIG(11)
          END DO
          IISET=1
          DO I=1,21
            HOLD(I)=GAIN(I)
            GAIN(I)=VAR1
          END DO
          XA1=JA+EPSA
          XB1=JB+EPSB
          IF(MODE.GE.2)SHIFT=S12

C       PERFORM THE GAIN CORRECTIONS FOR THE SECOND
C       PAIR OF PROFILES.

          GOTO 998
        END IF

C       ONCE BOTH PAIRS OF GAIN CORRECTIONS HAVE BEEN
C       CALCULATED, DETERMINE IF THE TWO SHIFT VALUES
C       AND TWO CENTRAL PROFILE CENTROIDS AGREE.

        DO I=1,21
          IB(I)=IA(I)
          IA(I)=TEMP(I)
        END DO
        IISET=0
        XA2=JA+EPSA
```

```
      XB2=JB+EPSB
      SHIFT=(XA2+XB2)/2-(XA1+XB1)/2
C     'MODE' IS ZERO FOR THE FIRST ITERATION.
      IF(MODE.EQ.0)GOTO 883
C     IF THE PROGRAM HAS GAIN CORRECTIONS FOR THE TWO
C     SETS OF PROFILES, CHECK TO SEE IF IT HAS IMPROVED
C     SINCE THE LAST ITERATION. IF NOT, MODIFY THE 'SHIFT' VALUES.
      IF(MODE.EQ.1)THEN
        S11=SHIFT
        S12=SHIFT
      ELSE
        S11=SHIFT+(SHIFT-(XB1-XA1))
        S12=SHIFT+(SHIFT-(XB2-XA2))
      END IF
C     IF THE SHIFT AGREE OR THE CENTRAL CENTROIDS
C     AGREE, INC 'FLAG2'.
      IF(DABS(SHIFT-(XB1-XA1)).LT.0.001)FLAG2=1
      IF(DABS(SHIFT-(XB2-XA2)).LT.0.001)FLAG2=FLAG2+1
      IF(FLAG2.EQ.2)GOTO 999
      FLAG2=0
      SHIFT=S11
C     RESET GAINS TO 1.000.
883   DO I=1,21
        GAIN(I)=VAR1
      END DO
      MODE=MODE+1
      GOTO 998
C     IF CENTROIDS AND SHIFTS AGREE, WE ARE DONE.
C     PRINT OUT AND STOP.
999   FLAG2=0
      DO I=1,21
        WRITE(9,300)I,GAIN(I)/GAIN(11),HOLD(I)/HOLD(11)
      END DO
100   FORMAT(1X,I2,6(F10.6))
200   FORMAT(1X,5(E13.6,' '))
300   FORMAT(1X,I4,2(F10.5))
      CLOSE(8)
      CLOSE(9)
      STOP
      END
C*************************************************************************
C         SUBROUTINE FLATC
C           H. SPATH'S SMOOTHING CUBIC SPLINE ROUTINE
C           SOURCE: Spline Algorithms for Curves and Surfaces
C           Translated by W. D. Hoskins and H.W. Sager
C           Utilitas Mathematica Publishing Inc. Winnipeg.
C
C     Computes coefficients Ak,Bk,Ck and Dk of a smoothing cubic spline
C     function.
C           f(x)=Ak*(x-xk)**3+Bk*(x-xk)**2+Ck*(x-xk)+Dk
C           where xk¡=x¡=x(k+1)
C     Input: N,(X(I),U(I),P(I),i=1,N),Y2(1)=y1",Y2(N)=yn"
C           N=number of nodes
C           X=array of x values
C           U=array of y values
```

```
C
C**************************************************************************
      SUBROUTINE FLATC(N,X,U,P,Y,Y2,DX,A,B,C,D)
      IMPLICIT REAL*8 (A-H,O-Z)
      DIMENSION X(N),U(N),P(N),Y(N),Y2(N),DX(N),A(N),B(N),C(N),D(N)
      DATA VAR0,VAR1/0.0,1.0/
      WW=VAR1
      WW1=VAR0
      N1=N-1
      N2=N-2
      C(1)=VAR0
      D(1)=VAR0
      RR1=Y2(1)
      RR2=Y2(N)
      B(1)=VAR0
      B(N)=VAR0
      DX(N)=VAR1
      H1=X(2)-X(1)
      DX(1)=H1
      DO 1 K=2,N1
        H2=X(K+1)-X(K)
        DX(K)=H2
        D(K)=1./(2.*(H1+H2)-H1*H1*D(K-1))
        H1=H2
1     CONTINUE
2     DO 3 K=1,N
        Y2(K)=0.
        Y(K)=U(K)
3     CONTINUE
4     W=WW
      W1=VAR1-W
      DO 6 K=1,N1
        H2=DX(K)
        R2=(Y(K+1)-Y(K))/H2
        IF(K.EQ.1)GOTO 5
        H=6.*(R2-R1)
        IF(K.EQ.2)H=H-H1*B(1)
        IF(K.EQ.N1)H=H-H2*B(N)
        C(K)=D(K)*(H-H1*C(K-1))
5       H1=H2
        R1=R2
6     CONTINUE
      B(N1)=C(N1)
      IF(N1.LE.2)GOTO 8
      DO 7 J=2,N2
        K=N-J
        B(K)=C(K)-D(K)*DX(K)*B(K+1)
7     CONTINUE
8     DO 9 K=2,N1
        B(K)=W*B(K)+W1*Y2(K)
9     CONTINUE
      J1=1
      H5=VAR0
      DO 10 K=1,N
        J2=K+1
        IF(K.EQ.N) J2=N
        H=((B(J2)-B(K))/DX(K)-(B(K)-B(J1))/DX(J1))/P(K)
        IF(W.EQ.VAR1)A(K)=-H
        IF(W.NE.VAR1)A(K)=W*(U(K)-H)+W1*Y(K)
        H5=H5+DABS(A(K))
        J1=K
10    CONTINUE
      H5=VAR1/H5
```

```
      IF(W.NE.VAR1)GOTO 13
      H1=VAR0
      H2=VAR0
      DO 11 K=1,N
        H=Y(K)
        H1=H1+A(K)*H
        H2=H2+H*H
11    CONTINUE
      WW2=H1/H2
      IF(DABS(WW2-WW1).LT.5.E-4*DABS(WW2)) GOTO 12
      WW1=WW2
      GOTO 15
12    WW=2./(1.+DSQRT(1.-WW2))
      B(1)=RR1
      B(N)=RR2
      GOTO 2
13    H2=VAR0
      H3=VAR0
      H4=VAR0
      DO 14 K=1,N
        H2=H2+DABS(A(K)-Y(K))
        H3=H3+DABS(B(K))
        H4=H4+DABS(B(K)-Y2(K))
14    CONTINUE
      IF(H2*H5+H4/H3.LT.5E-4)GOTO 17
      H5=VAR1
15    DO 16 K=1,N
        Y2(K)=B(K)
        Y(K)=A(K)*H5
16    CONTINUE
      GOTO 4
17    DO 18 K=1,N1
        J2=K+1
        D(K)=A(K)
        A(K)=(B(J2)-B(K))/(6.*DX(K))
        C(K)=(A(J2)-D(K))/DX(K)-DX(K)*(B(J2)+2.*B(K))/6.
        B(K)=.5*B(K)
18    CONTINUE
      D(N)=A(N)
      B(N)=.5*B(N)
      RETURN
      END
```

References

[1] B. Desplanques, J.F. Donoghue, B.R. Holstein, Ann. Phys. (NY) 124, 449 (1980).

[2] V.M. Dubovik, S.V. Zenkin, Ann. Phys. (N.Y.) 172, 100 (1986).

[3] M. Simonius, Proceedings Symposium/Workshop on Parity Violation in Hadronic Systems, TRIUMF Report TRI-87-3, 189 (1987).

[4] M. Simonius, Proceedings of Interactions Between Particles and Nuclear Physics - 1986, ed. D. Geesaman, AIP Conference Proceedings No 150, 185 (1986); Can J. Phys. 66, 245 (1988).

[5] R.A. Arndt, L.D. Roper, R.A. Bryan, R.B. Clark, B.J. verWest, P. Signall; Phys. Rev. D28, 97 (1983).

[6] D.E. Driscoll and G.A. Miller, Phys. Rev. C 39, 1951 (1989).

[7] P.W. Schmor et al, European Particle Accelerator Conference-1988, ed. S. Tazzari, World Scientific Publishing Co., 1375 (1989).

[8] M.K. Craddock, TRIUMF Design Note TRI-DN-84-8 (1984).

[9] P.D. Eversheim et al, 7^{th} International Conference on Polarization Phenomena in Nuclear Physics: Paris 90, contributed abstract, 3D (1990).

[10] P.D. Eversheim, private communication (1990).

[11] J.M. Potter et al, Phys. Rev. Lett. 33, 1307 (1974).

[12] J.M. Potter et al, International Symposium on High Energy Physics with Polarized Beams and Targets-1978, ed G.H. Thomas, AIP Conference Proceedings No. 51, 224 (AIP New York, 1979).

[13] S. Kistryn et al, Phys. Rev. Lett. 58, 1616 (1987) and references therein.

[14] P von Rossen et al, Polarization Phenomena in Nuclear Physics-1980, ed. G.G. Ohlsen et al., AIP Conference Proceedings No. 69, 1442 (AIP, New York, 1981).

[15] D.M. Tanner et al, Proc. Int. Conf. on Nucl. Phys., Florence F1 697 (1983).

[16] V. Yuan et al, Phys. Rev. Lett., 57, 1680 (1986).

[17] N. Lockyer et al, Phys. Rev. D30, 860 (1984).

[18] T. Goldman and D.Preston, Phys. Lett. 168B, 415 (1986).

[19] S.A. Page, Proceedings Symposium/Workshop on Spin and Symmetries, TRIUMF Report TRI-89-5, 2 (1989).

[20] H.A. Bethe, Ann. Physik 5, 325 (1930).

[21] G.A. Erskine, Nucl. Inst. Meth., 105, 565 (1972).

[22] F. Sauli, Principles of Operation of Multiwire Proportional and Drift Chambers, CERN 77-09, (1977).

[23] J.S. Townsend, Electricity in Gases, 324 (1915).

[24] D. Mischke, private communication, (1987).

[25] E.J. Sternglass, Phys. Rev., 108 ,1 (1957).

[26] W.R. Falk, Nucl. Inst. Meth., 220, 473 (1984).

[27] H.L. Anderson, Second edition Vade Mecum, (AIP, New York, 1989).

[28] J. Schou, Transport Theory for Kinetic Emission of Secondary Electrons from Solids, Phys. Rev. B, 22, 5 (1980).

[29] R. Chehab et al, IEEE Pacific Conference Proceedings: High Energy Accelerators, Fermilab, 606 (1983).

[30] M. Von Ardenne, Tabellen Zur Angewandten Physik, 99 (1962).

[31] H. Spath, Spline Algorithms for Curves and Surfaces, Translated by W. D. Hoskins and H.W. Sager, Utilitas Mathematica Publishing Inc. Winnipeg.